

August 2019

Scattering in Infrared Microspectroscopy

Alex James Schofield
University of Wisconsin-Milwaukee

Follow this and additional works at: <https://dc.uwm.edu/etd>



Part of the [Physics Commons](#)

Recommended Citation

Schofield, Alex James, "Scattering in Infrared Microspectroscopy" (2019). *Theses and Dissertations*. 2247.
<https://dc.uwm.edu/etd/2247>

This Dissertation is brought to you for free and open access by UWM Digital Commons. It has been accepted for inclusion in Theses and Dissertations by an authorized administrator of UWM Digital Commons. For more information, please contact open-access@uwm.edu.

SCATTERING IN INFRARED MICROSPECTROSCOPY

by

Alex J. Schofield

A Dissertation Submitted in
Partial Fulfillment of the
Requirements for the Degree of

Doctor of Philosophy
in Physics

at

The University of Wisconsin-Milwaukee

August 2019

ABSTRACT

SCATTERING IN INFRARED MICROSPECTROSCOPY

by

Alex J. Schofield

The University of Wisconsin-Milwaukee, 2019
Under the Supervision of Professor Carol J. Hirschmugl

Mid-infrared absorbance spectra obtained from spatially inhomogeneous and finite samples often contain scattering effects that undermine the Beer-Lambert law assumption. Such spectra contain generally non-linear contributions from the scattering material's complex refractive index, which may result in derivative-like bands with shifted peak positions. It is first shown using Mie theory for spherical scatterers, that these band distortions may be interpreted and accurately modeled by Fano theory when the imaginary part of its complex dielectric function is small and Lorentzian in nature—as is the case for many biological media. By fitting Fano line shapes to isolated absorbance bands, recovery of the peak position and pure absorption strength can be obtained with high accuracy. Additionally, for small and optically soft spherical scatterers, recovery of one or the other of constant refractive index or radius (given approximate knowledge of the other), is possible.

Next, these methods from Fano modeling are generalized to multiple, overlapping absorbance bands (as they naturally occur in practice). To account for stronger absorbance strengths encountered in materials such as polystyrene, a second-order model is proposed, with an iterative fitting algorithm provided. The algorithm can model, up to a scaling factor, the imaginary refractive index of a weakly-scattering sphere when it is composed of Lorentzian oscillators. The methods are demonstrated on a polystyrene (PS) sphere embedded in a potassium-bromide (KBr) pellet. Given knowledge of the sphere's size (known

from the manufacturer, and its brightfield measurement), recovery of the constant refractive index difference between PS and KBr, along with a region of the imaginary refractive index and its scaling factor are demonstrated.

Finally, a technique for measuring the phase and amplitude of spatially- and spectrally-resolved samples in the mid-infrared is presented. The design builds on the Mach Zehnder interferometer, with the addition of a high-precision variable-path scanner. The principles of traditional Fourier-Transform Spectroscopy are adapted for use in a Mach Zehnder interferometer, where a sample is placed inside one of the paths as opposed to outside of the interferometer. In this modified setup, an interferogram is measured by varying the path length, as it is in classic Fourier Transform Spectroscopy; however, the resulting spectrum after Fourier transformation of the interferogram is complex, with its phase and amplitude related to that of the scattered field. The additional phase information may help improve scatter correction and three-dimensional hyperspectroscopy, as well as providing quantitative phase imaging techniques.

© Copyright by Alex J. Schofield, 2019
All Rights Reserved

TABLE OF CONTENTS

LIST OF FIGURES	xii
LIST OF TABLES	xiii
ACKNOWLEDGMENTS	xiv
1 Introduction	1
1.1 Infrared Spectroscopy Background	1
1.2 Spectral Analysis and Scattering	3
1.2.1 Spherical Scattering	4
1.2.2 Fano Line-shapes	5
1.3 Hyperspectral Infrared Spectroscopy	8
1.3.1 Electromagnetic Phase	10
1.3.2 Holography	12
1.3.3 FTIR Holography: Future Work	15
1.4 Thesis Overview	18
2 Spherical Scattering Part I: Isolated Peaks and the Fano Effect	20
2.1 Introduction	20
2.1.1 Fano Resonances	21
2.1.2 Fano Line Shapes in FTIR Spectroscopy	23
2.2 Methods	24
2.2.1 Scattering on Spheres	26
2.2.2 Connection to Fano Theory	28
2.3 Results	31
2.4 Discussion	34
2.4.1 Simulations	36
2.4.2 Bulk-absorption Limit	36
2.4.3 Connecting Fano Parameters With Radius and Refractive Index	37
2.5 Conclusions	38
2.6 Appendix	41
3 Spherical Scattering Part II: Multiple Peaks and the Generalized Fano Effect	49
3.1 Introduction	49
3.2 Methods	50

3.2.1	Multi-peak Modeling	53
3.3	Results	62
3.3.1	Simulated Mie Spectra	62
3.3.2	PS in KBr	64
3.4	Discussion	70
3.4.1	Simulations	73
3.4.2	PS in KBr	73
3.5	Conclusions	74
3.6	Future Work Applied to Hyperspectral Imaging	75
4	Fourier-Transform Holographic Spectroscopy	86
4.1	Introduction	87
4.2	Methods	87
4.2.1	Fourier-Transform Spectroscopy	87
4.2.2	Fourier-Transform Holographic Spectroscopy	92
4.2.3	General Path Amplitudes	96
4.2.4	Relation to Phase Shifting Holography	98
4.3	Results	99
4.4	Emission Measurement	100
4.5	Micro-Loop Measurement	103
4.6	Discussion	106
4.7	Conclusions	109
5	Lessons Learned for Extending IR Microscopic Techniques	111
5.1	Infrared Diffraction Tomography	111
5.1.1	Introduction	111
5.1.2	Methods	113
5.1.3	Conclusions	120
5.2	Digital Confocal IR Spectroscopy	121
5.2.1	Introduction	122
5.2.2	Methods	124
5.2.3	Results	130
5.2.4	Discussion	134
5.2.5	Conclusions	135
	References	141
	Appendix: Overview of In-line Holography	162
A.1	In-line Holography	163
A.1.1	Common Path Interference	163
A.1.2	Double Path Interference	166
A.1.3	Example: Imaging a Point Source	168
	CURRICULUM VITAE	172

LIST OF FIGURES

2.1	Fano line shapes for various values of the Fano parameter q . The line shapes are plotted in terms of the reduced coordinate $\epsilon = (E - E_r)/\frac{1}{2}\Gamma_E$, where $\epsilon = 0$ corresponds to the exact resonance position $E = E_r$. For finite $ q > 0$, the peak shifts away from the resonance at $\epsilon = 0$, such that the peak position alone is insufficient for identifying the resonance energy. For $q > 0$, the peaks shift toward positive ϵ , and toward negative ϵ for $q < 0$	22
2.2	Extinction curve Q_{ext} and the Mie background Q_{BG} for a particle of radius 2 μm and constant refractive index $n_0 = 1.5$. Removal of Q_{BG} from the extinction curve Q_{ext} leaves a curve that approaches zero away from the resonance.	27
2.3	Comparing select simulated Mie spectra for a single absorbance band in the vicinity of 1600 cm^{-1} with its local expansion. The associated constant refractive index, radius, size parameters and errors are given in Table 2.1. Left: Simulated spectra Q' and their local expansion Q'_{exp} (Eq. 2.17, to first order in f_0 exact in Δ). Right: Simulated spectra Q' and its local expansion Q'_{Δ} (Eq. 2.19, to first order in f_0 , and second order in Δ).	33
2.4	Select simulated Mie spectra for a single absorbance band in the vicinity of 1600 cm^{-1} . The associated constant refractive index, radius, size parameters and Fano fit parameters q are given in Table 2.1. Left: Simulated spectra with the background removed and the associated Fano fits. Right: The ideal Lorentzian line shapes that would be measured in the absence of scatter effects, and the recovered Lorentzian line shape using the Fano fit parameters.	34
2.5	Recovered resonant position $\tilde{\nu}_r$ for select refractive indices n_0 as a function of size parameter $2\pi a\tilde{\nu}_r$. Shown are the error in position estimates that would be predicted from the simulated transmission spectrum (with scatter), and the recovered positions. As the constant refractive index n_0 increases, the peak position can be shifted by as much as 1.6%, but we are able to recover the true positions $\tilde{\nu}_r$ to within 0.2% or better.	46
2.6	How refractive indices calculated from Fano fitting compare to exact values. Legend: Actual constant refractive indices n_0 for various sphere sizes. Dark markers indicate calculations that fall within 1% of the exact value. Vertical axis: Calculated n_0 with knowledge of the particle's size, using Eq. 2.26. Left: Calculated n_0 vs Fano fit parameter q . Dashed line at $q = -1$ are anti-Lorentzian line shapes, while large q approach pure Lorentzians. Right: Calculated n_0 vs size parameter $2\pi a\tilde{\nu}_r$ for radius a and resonating band $\tilde{\nu}_r$	47

2.7	Error in absorbance strengths as a function of size parameter $2\pi a\tilde{\nu}_r$ for various constant refractive indices n_0 (see legend). Solid markers are recovered absorbance strength errors (using Eq. 2.25), while hollow markers are the error if one were to simply remove the anti-Lorentzian contribution (using Eq. 2.29 from Fano fit parameters). All calculations fall under 10% for each of the particles in our simulations.	48
2.8	Recovered full width at half maxima $\Gamma_{\tilde{\nu}}$ from fitted Fano line shapes have an error that appear to depend mostly on the fit parameter q . When $ q > 6$ the line shape is mostly Lorentzian and the error in determining peak width is nearly under 2%. However, when $ q < 6$ the line shape loses symmetry and the error climbs to nearly 6%.	48
3.1	A simulated refractive index is composed of Lorentzian bands (visible in the imaginary component) and its Kramer's-Kronig (visible in the real component). The Kramer's-Kronig component sits atop a constant refractive index $n_0 = 1.57$	63
3.2	Various extinction models are compared against an exact Mie simulation, using the refractive index in Fig. 3.8. Each assume a radius $a = 5 \mu\text{m}$ and a background refractive index $n_m = 1.53$. The first-order model Q_1 shows significant overshoot around the stronger absorbance bands in the 1600 cm^{-1} region. The upper (and lower) bands are examined more closely in Figs. 3.3 and 3.4, respectively.	64
3.3	Comparing various extinction models in the higher-wavenumber region of Fig. 3.2, where the bands are significantly weaker. Here, while both the first and second order models overshoot slightly from the exact van de Hulst and Mie, there is very little difference between the expansion models Q_1 and Q_2	65
3.4	The stronger bands from Fig. 3.2 show that accurate modeling requires the second-order model Q_2 when the bands are stronger, as the linear-order expansion model Q_1 shows significant overshoot from the other models.	65
3.5	Fitting the second order model Z_2 to the stronger bands of the exact Mie simulation in the 1600 cm^{-1} region (Fig. 3.4). The estimated peak positions (and their refined values) are displayed in Fig. 3.7.	66
3.6	The extracted (scaled) imaginary refractive index (from the second-order fitting in Fig. 3.5) compared with the exact refractive index shown in Fig. 3.1. The extracted refractive index is inherently scaled by $1/\Delta$. Although the fitting is nearly perfect in Fig. 3.5, the extracted refractive index shows some discrepancy, due to the model's approximation errors (see Fig. 3.4, Q_2).	66
3.7	Detected peak positions that were used as input for the modeling process in Fig. 3.5. Also displayed are the updated positions that have been refined by the gradient descent step in Alg. 1.	67
3.8	The fluctuating component of the real refractive index around 3200 cm^{-1} shows a slight deviation from n_0 , due to residual influences of the strong bands in the 1600 cm^{-1} region.	67

3.9	Peak detection is performed using the second derivative of the input spectrum $A(\tilde{\nu})$. Shown is the (negative) second derivative of the input spectrum $A(\tilde{\nu})$; each of its local maxima greater than zero (dashed line) identify a peak position.	68
3.10	Measured extinction image at $\tilde{\nu} = 3024 \text{ cm}^{-1}$. The green circle is the approximate region used to obtain the average spectrum in Fig. 3.11.	69
3.11	Extinction spectrum averaged over the region shown in Fig. 3.10. The CO ₂ region (2400 cm^{-1} to 2250 cm^{-1}) has been removed. The high-frequency bands (around 3000 cm^{-1}) are modeled with the second-order model Z_2 (see Fig. 3.12).	69
3.12	Modeling results after 160 iterations. Using the manufacturer's specification of $a = 5 \text{ }\mu\text{m}$, the estimated refractive index difference is $\Delta \approx 0.041$.	70
3.13	Extracted refractive index \tilde{n} for PS using the modeling in Fig. 3.12.	71
3.14	Pixelated expansion of using the model in Eq. 3.41. Each of the six images contains four samples; the upper two are weak scatterers (see spectra in Fig. 3.15, upper), while the lower two have stronger scatter signatures (see spectra in Fig. 3.15, lower).	78
3.15	Average spectra for each of the four images in Fig. 3.14. The CO ₂ region (around 2300 cm^{-1}) has been removed from all spectra.	79
3.16	The spectral dependence of the background images. The four images ((a) through (d)) are taken at the positions indicated within the spectral range shown in Fig. 3.17. The high wavenumber image (a) shows more diffraction-like features for the bottom two high-scattering spheres. Furthermore, the innermost prominent rings for the bottom two spheres appear to be partitioned down the middle (a slight figure-eight appearance), whereas the rings are completely hollow in the low wavenumber image (d). The structure of the upper (low-scattering) spheres appear very similar accross each of the wavenumber positions in (a) through (d).	80
3.17	The positions corresponding to the background images shown in Fig. 3.16. The displayed curve is the background averaged over all pixels from each of the coefficients B_2 , B_1 , and B_0 .	81
3.18	Pixelated expansion of PS beads in a PU matrix, using the model in Eq. 3.41. While the analysis is complicated by the overlapping bands between the medium and sample, some interesting features appear. Namely, a very subtle shifting occurs between the apparent bead locations—most notably between F , G , and the linear and constant terms B_1 and B_0 . The extinction image (upper left) has been baseline corrected about the 3024 cm^{-1} band.	82
3.19	A theorized explanation for the observed shift between images in the pixelated expansion shown in Fig. 3.18. Since the incident beam enters at an angle, the scattered rays – while symmetric about the forward ray <i>inside</i> the medium – do not exit the medium symmetrically. Therefore, the scattered rays appear to originate from a slightly offset position (“scattered virtual image”), compared to the non-scattered rays (“forward virtual image”).	84

4.1	Fourier-transform spectroscopy using a Michaelson interferometer. A broadband source is split into two paths by a beamsplitter (BS). Along the first path, the field U_1 is reflected by a translating mirror before transmitting through BS and recombining with the second path. Along the second path, the field U_2 is reflected by a fixed mirror before being reflected by BS and recombining with the first path. The combined fields U' interact with the sample before arriving at the camera.	89
4.2	Schematic of our modified Mach Zehnder interferometer for performing Fourier-transform holographic spectroscopy. A broadband (temporally incoherent) laser source is split into two paths by the first beamsplitter BS ₁ . Along the first path: the field U_1 reflects off BS ₂ , reflects from a translating mirror, transmits through BS ₂ , interacts with the sample, and finally transmits through BS ₄ where it is recombined with the second path at the camera. Along the second path: the field U_2 reflects off BS ₃ , reflects from a fixed mirror, transmits through BS ₃ , and finally reflects off BS ₄ where it is recombined with the first path at the camera.	93
4.3	Areal photograph of our modified Mach Zehnder interferometer, whose orientation corresponds to the schematic in Fig. 4.2. A near-IR flash light (peak wavelength ≈ 940 nm) is placed against a 25 μm pinhole, and collimated by a 2.54 cm diameter lens whose focal length is 5 cm. (Note: the camera was not properly aligned in this photograph. The detector should be perpendicular to the optical axis—not at the slight angle shown.)	100
4.4	Intensity at the approximate ZPD location (see the peak position in Fig. 4.5) shows high contrast fringes due to the constructive (and destructive) interference from the broadband source when the two path-lengths of the MZI are nearly equal.	101
4.5	The variance over the entire FOV of Fig. 4.4 is maximal when the fringe contrast is greatest, indicating the position of ZPD. The downward sloped baseline is due to the loss of battery power during the hour-long measurement.	101
4.6	An example single-pixel interferogram obtained at the position $(x, y) = (117, 141)$ from the image in Fig. 4.4. The oscillations are greatest in magnitude at the ZPD position since all wavelengths are constructively (or destructively) interfering. Away from ZPD the oscillations approach the constant value $(\bar{I}_0 + \bar{I}_s)/2$ (see Eq. 4.18). The downward sloped baseline is due to the loss of battery power during the hour-long measurement.	102
4.7	The average spectrum (complex magnitude) over the entire FOV of Fig. 4.4 shows that the NIR source is broadband with a central wavenumber near 1060 cm^{-1} , consistent with the source's 940 nm wavelength specification. The spectrum is obtained from the Fourier transform of each pixel's interferogram (e.g., Fig. 4.6) after centering about the ZPD obtained from the variance (Fig. 4.5) and removing a best-fit second-order polynomial baseline to account for the D.C. term $(\bar{I}_0 + \bar{I}_s)/2$ (see Eq. 4.18), as well as the sloped behavior due to the battery's decay. The apparent double peak is likely due to an absorbance from the beam-splitters, which contains a band near that position (see Fig. 4.8).	102

4.8	Absorbance spectrum of one of the beamsplitters used in the interferometer in Fig. 4.3 shows a strong band near 9950 cm^{-1} , consistent with the wedge observed in the same location of the emission spectrum of the NIR source in Fig. 4.7.	103
4.9	A MiTeGen micro loop similar to the one used as a sample in Sec. 4.5. Shown is a mid-infrared absorption measurement, integrated over all wavelengths. The total field of view is $141 \times 141\text{ }\mu\text{m}^2$	104
4.10	The variance over small regions located on the micro-loop, and away from it (labeled Air) shows a negative shift in the ZPD of the micro-loop, expected due to its extended optical path length. This shift is unique to the setup where a sample is placed inside one of the paths, and is not observed in traditional Fourier-transform spectroscopy where the sample is placed outside of a Michaelson interferometer.	104
4.11	Magnitudes and phases at the two peak positions from the emission spectrum in Fig. 4.7. The phase has been unwrapped using [159, 160], and a large overall slope has been subtracted using an estimate obtained along its vertical edge.	105
4.12	Back-propagation results (right) of the hologram (left), using modified MATLAB code made available by Latychevskaya and Fink [79] with an assumed plane wave model. Shown are magnitude images.	106
5.1	Left: Chemogram projection image of a $2\text{ }\mu\text{m}$ pinhole measured with a global infrared source. Image is cropped from 128×128 to 64×64 , and each pixel maps $\approx 1.1\text{ }\mu\text{m}$ in size. Right: Chemogram PSF slice through the center along z -axis, measured from $z = 0$ to $30\text{ }\mu\text{m}$ in $5\text{ }\mu\text{m}$ steps and interpolated to $1\text{ }\mu\text{m}$ steps. Due to the extended acquisition times required when the pinhole is out-of-focus, data are only acquired along the positive z -axis; symmetry is assumed and the data are mirrored about $z = 0$ and processed with a bilateral filter to suppress noise.	125
5.2	Step 1: A column of z measurement data are extracted from a window positioned in x , and y . Step 2: The column of data is filtered such that positions in z containing minimal focus (by measuring e.g. contrast) are attenuated. Step 3: The filtered column of data is added back into the reconstructed dataset. The process repeats for a new overlapping window shifted by one pixel.	128
5.3	1D inverted Mexican hat function.	130
5.4	From left to right, images are captured with the micro-loop positioned at the focal planes: $-20\text{ }\mu\text{m}$, $0\text{ }\mu\text{m}$, $20\text{ }\mu\text{m}$	131
5.5	Visible three-dimensional PSF for a $2\text{ }\mu\text{m}$ pinhole. Slice taken through $x = 0$, with the z -axis pointing upwards and y -axis pointing to the right.	132
5.6	Plots of the Michelson contrast calculated for a window positioned in the center of the microloop. Top: A $4 \times 4\text{ px}^2$ window. Bottom: A $16 \times 16\text{ px}^2$ window	133
5.7	Various algorithms applied to the raw bright-field data (top row), each shown at three z positions.	137

5.8	Maximum intensity projection images viewed from an angle. Left: Raw data. Middle: Deconvolved data (Richardson-Lucy with TV normalization, 40 iterations). Right: Digital optical sectioning algorithm. The method fails for large $ z $, where only out-of-focus light ever enters a z window column.	138
5.9	Left: Raw data at $z = 0$. Vertical green line shows the slice used in both the middle and right figures. Middle: Raw data y - z slice at $x = 0$ (z axis points upwards). Right: Digital optical sectioning results capture the angle with which the microloop was mounted.	138
5.10	Volume renders of the digital optical sectioning results. Left: Bird's eye view (looking into the $-z$ direction). Middle: At an angle. Right: Side view, looking into the $-x$ direction (z -axis pointing upwards), showing that the angle with which the microloop was mounted has been captured by the algorithm.	138
5.11	Average spectrum at $z = 0$. Yellow regions are attributed to polyimids in the micro-loop while pink regions are attributed to functional groups in the nail polish.	139
5.12	Volume renderings from y - x (leftmost) to x - z (rightmost) using color-coded baseline-integrated regions from the spectrum in Fig. 5.11.	139
5.13	Average spectrum at $z = 0$. Yellow regions are attributed to polyimids in the micro-loop while pink regions are attributed to functional groups in the nail polish.	140
A.1	Common path in-line holography recording configuration. An incident plane wave U_0 induces a field U_s from a weakly-scattering object \mathbf{O} . The fields U_0 and U_s interfere at the hologram plane located a distance D to the right. . .	164
A.2	The in-line hologram is reconstructed by illuminating the hologram with the original reference field U_0 . To the right of the hologram, three components emerge superimposed: the zero-order due to U_0 , a real image (which is the phase conjugate of the original object's field), and a virtual image of \mathbf{O} appearing out-of-focus at the detection screen.	166
A.3	In a Mach Zehnder interferometer, the source is split into two paths with strengths U_0 by the beamsplitter BS_1 (with a perfect transmitting/reflecting ratio assumed for simplicity). The total field along the sample path just before the second beamsplitter BS_2 is $U_0 + U_s$, where U_s is the scattered field due to the sample. This field is combined with the reference U_0 that was transmitted by BS_1 , and the total combined field at the camera by BS_2 is $U_0 + \frac{1}{2}U_s$	167
A.4	Point source diffraction at coordinates (x_p, y_p) produce the Fresnel zone holograms in Fig. A.5 for various distances D . The point source \mathbf{P} may be due to a small obstruction (e.g., dust), or from a small opening of an opaque screen, in which case a double-path configuration is required to interfere with a reference field (not shown).	170
A.5	Example Fresnel zone plates due to a point source located at various distances D from the hologram plane (Fig. A.4). The hologram is a 128×128 image with a linear pixel size of $1.1 \mu\text{m}$, capturing the interference of a point source located at the origin, radiating with a wavelength $\lambda = 5 \mu\text{m}$	170

LIST OF TABLES

2.1	<p>Simulation results for the particles in Figs. 2.4 and 2.3. Included are the constant refractive index n_0, particle radius a, the size parameter $2\pi a\tilde{\nu}_r$, the Fano fit parameters σ_0 and q, along with the expansion errors for Q'_{exp} and Q'_Δ (Eq. 2.17 and 2.19). The percent errors are calculated as the maximum difference between the expansion and Q', divided by the overall scale of Q' (e.g. $100\% \times \left\ \frac{\max [Q' - Q'_{\text{exp}}]}{\max [Q'] - \min [Q']} \right\$)</p>	35
-----	---	----

ACKNOWLEDGMENTS

This work would not have been possible without all of the support I have received throughout my graduate schooling and during the preparation of this dissertation. There are many people I wish to thank who have either contributed directly to this work, or who have supported me financially, emotionally, or otherwise during my graduate career.

First and foremost, I would like to thank Professor Carol J. Hirschmugl, for whom it has been an absolute pleasure to have as my Ph.D. advisor. From her I have received a tremendous deal of guidance, expertise, and freedom throughout my studies. She has an exceptional instinct for physics, and with it an ability to guide and motivate—especially when faced with obstacles or dwindling confidence. I thank her not just for continually challenging me, but also for the freedom and trust she placed in me, without which much of the work contained here wouldn't exist. I appreciate all that she has done for me—above all, teaching me how to be a professional scientist. Thank you for making this all possible.

I have also had the pleasure of working alongside an amazing group over the years. To my colleagues, Dr. Ebrahim Aboulizadeh, Nicholas Walter, Sugato Ray, and Dr. Ghazal Azarfar, I thank you for all your discussions, support, and friendships. I'd like to thank Ebrahim and Nick for their kind welcoming and mentoring when I first joined the group. I additionally want to acknowledge Nick's efforts in Chapters 3 and 4, for his experimental contributions and help with the construction of our microscope. Thank you also to Sugato for his exceptionally hard work, notably his contributions in automating the data acquisition for our microscope prototype. He has also proofread many portions of this dissertation and provided a great deal of feedback. I also want to thank Ghazal for the many discussions, and especially for her perspectives and ideas during the construction of our microscope.

It has also been a pleasure working with our many collaborators, each of whom I would like to acknowledge and thank for their contributions to this dissertation. Weekly insightful discussions were had over the years with Professor Reinhold Blümel from Wesleyan University, and Professor Achim Kohler, Dr. Tatiana Konevskikh, Dr. Rozalia Lukacs, and

Johanne Solheim from the Norwegian University of Life Sciences. I especially want to thank Reinhold for his invaluable contributions to the work in Chapter 2. I believe that his meticulous care for the details and presentation of its content helped in both its publication and selection for Editor’s Pick in the Journal of Chemical Physics. I would also like to thank Achim and Rozalia for their contributions in supplying simulations for this work, along with other various suggestions and technicalities that were included.

Our local collaborators, Professor Yongjin Sung and Dr. Hamid Balyani, have provided valuable expertise during the construction of our microscope prototype presented in Chapter 4. Thank you, Yongjin and Hamid, for all of your help.

Additional sample preparation was performed by Karl Stuen from the University of Wisconsin, Madison. He is acknowledged for his preparation of the polystyrene beads in polyurethane film sample analyzed in Chapter 3.

My gratitude also extends to the support of my committee: my advisor Professor Carol J. Hirschmugl, along with Professors Michael Weinert, Valerica Raicu, Reinhold Blümel, and Achim Kohler. I have had the pleasure of being a student of Professors Weinert and Raicu, both of whom are excellent teachers, and to have closely collaborated with Professors Blümel and Kohler. I thank them for their time and generosity, especially their feedback and suggestions regarding the content and structure of this dissertation.

I also have the fortune of being blessed with an incredibly supportive and loving family. I wish to extend my love and gratitude to my wife Taylor and our beautiful baby daughter Lucy. I could not ask for a more supportive wife who shouldered so many extra responsibilities, sacrificed so much sleep, always ensuring that I had ample time to focus on writing. This is in addition to being an amazing mother, all while working full time as a physician, and earning an additional Master’s degree. Thank you Taylor, I love you. Lucy, while you may be overly vocal when I’m not exclusively playing, holding, or reading to you, you’re an absolute joy and the best thing to have happened in my life. You are adorable and I love you.

I want to thank my parents Laurie and Marvin for all of their caring and loving support. I acknowledge not only the extra help they offered during the writing of this dissertation, but their incredible love, guidance, and support that they have provided throughout my life. I am very fortunate to have you as parents and role models, thank you so much for everything! I also wish to thank Shannon for all of her support, especially for helping with Lucy during the writing process of this dissertation. I love you all very much!

A very special thanks is owed to my mother- and father-in-law Carol and Jim, without whom this dissertation wouldn't have been completed for another three years. You are amazing parents, grandparents, and foster parents; Taylor and I are eternally grateful for all of your help.

Thank you to my loving sister Kaitlyn for all of her gracious support. I particularly want to thank her and Derek for all of their help with Lucy. I also thank my in-laws, Megan, Kelly, and Pete, for all their considerate kindness. To each of my nieces and nephews, Aidan, Elijah (expected), Alma, and Samuel, you are wonderful kids, for which I am proud to have in my life. I love you all dearly!

Thank you to my grandparents Carol and Robert, Jorja (Bob), and Jerry (Ellen), for all of their support. I particularly want to thank Carol and Robert for their generous financial contributions through my undergraduate years. And to my great-grandmother Jean who made it to my wedding, held her great-great-granddaughter, and almost saw me graduate, I love you. Thank you also to my aunts and uncles, Brian (Julie), Barb, Phil (Heather), Cathy (Tom), and Kolina (Eric), for all of their loving support. Thank you so much, I love you all.

I also want to thank my close friends: Jon, Chris, Angela, Shelby, and Luz. Jon and Chris may now rest assured that, after years of persistent nagging, I will finally have time to download Fortnite (maybe). I am grateful to have each of you as loving and caring friends, and I thank you all for your support and understanding during the writing of this dissertation. I also want to thank Luz and her family's generous hospitality that gave me

many weekends to work without interruption.

Finally, I wish to acknowledge the financial support received during my time at UWM, allowing me to focus on the research for this dissertation, including: the National Science Foundation (award number CHE-1508240); the David Lichtman Memorial Award; numerous Chancellor's Graduate Student Awards; and other awards and fellowships provided from the UWM Physics Department—all of which I very much appreciate.

Chapter 1

Introduction

1.1 Infrared Spectroscopy Background

The interaction between electromagnetic radiation and matter may be categorized in a broad sense by its effect on atomic and molecular states. For instance, gamma, x-ray, and ultraviolet radiation are sensitive to electronic interactions, particularly the ionization of atoms and molecules. Similarly, light in the visible region is often associated with atomic state transitions. Infrared (IR) radiation, on the other hand, is closely associated with molecular vibrations, while microwave and radio waves are generally reserved for changes in molecular orientation (e.g., rotations and electric currents).

The molecular vibrations associated with IR radiation may be studied by considering the spectrum of interactions across distinct wavelengths. IR-active matter contains induced or permanent dipoles whose response most notably includes stretching, bending, rocking, wagging, and twisting [1]. Intermolecular interactions are also possible; for example, secondary structures such as beta sheets and alpha helices may have distinct IR-active vibrational modes. Rotational modes may also resonate with IR radiation (especially molecules in gaseous states), although the effect is much stronger in the microwave region. These various responses are highly dependent on both the material's chemical makeup, and radiation

wavelength. Distinct bands where IR radiation is converted to vibrational energy may be observed in measurements of a material’s ability to attenuate a radiating source as a function of wavelength. Infrared spectroscopy is therefore an extremely useful tool for studying the chemical properties of matter, since unique configurations of absorbance band strengths and positions present for different chemical and higher-order structures.

Obtaining a spectral decomposition of infrared radiation does not share in the simplicity often afforded in visible spectroscopy by the use of dispersive prisms and diffraction gratings. Indeed, early IR-spectroscopy used such optical elements, but insensitive recording materials severely limited both the spectral resolution and signal-to-noise ratios (SNR). It was not until the early 1970’s, following both the discovery of Fellgett’s advantage (in which interferometric, or multiplexed measurements have an increased SNR over wavelength-scanning methods), along with the fast Fourier transform, that a practical realization of infrared spectroscopy would be possible. Fourier-transform infrared (FTIR) spectroscopy has since become the standard instrumental method for infrared spectroscopy [1, 2].

The core operation of an FTIR spectrometer is based on the Michelson interferometer, named after its inventor Albert Michaelson in the late 1800’s. In FTIR spectroscopy, an interferogram is measured for a broadband signal by varying the path-length of the interferometer. Upon Fourier transforming the interferogram, one obtains a spectrum representing the strength (or amount) of each constituent wavelength contained within the broadband signal. Applied to infrared spectroscopy, this method may reveal important chemical information when a sample is used as a filter for an IR source. In other words, resonating bands of an IR-active material acts as an attenuating filter at distinct frequencies, resulting in observed spectral peaks in the measured spectrum. Using a *background* measurement of the source (i.e., an emission spectrum without a sample in place), the ratio of the sample and background spectrum provides a transmission spectrum that ideally depends only on the sample itself, without any environmental, instrumental or contributions from the radiating source.

FTIR excels in applications where chemical information from bulk, homogeneous materials are desired. The technique is therefore attractive in many disciplines where materials are studied. For example, chemists may use FTIR for identifying chemical compounds or impurities; biologists may be interested in the content of components such as proteins, lipid, DNA and RNA in tissues or cells – often for the purpose of pathology [3, 4]; geologists may be interested in classification of fossils, the evolution of organic and inorganic matter [5], or the diagenesis of organic matter in lake sediments at different depths [6].

1.2 Spectral Analysis and Scattering

Ideally, IR radiation is linearly absorbed as it propagates through a bulk, homogeneous material. The Beer-Lambert relation states that, in terms of electromagnetic theory of dielectric media, the total absorbance is proportional to the product of the imaginary component n_i of the material’s complex refractive index (RI), and its thickness. The imaginary RI is related to the wavelength-dependent dielectric properties of the material; distinct vibrational resonance bands appear at various wavelengths for distinct chemistry. Since the measured absorbance is sensitive to the size (and possibly other factors such as temperature), interpretation of spectra often relies on relative band strengths. *Therefore, proper interpretation and analysis of spectra demands accurate measurement of band positions and strengths.*

Instrumental errors, environmental effects, and scattering caused by the presence of spatial inhomogeneities in the real RI (most notably are air-sample interfaces) may significantly alter the apparent absorption from the ideal Beer-Lambert law. The spectral effect of scatter and other instrumental effects often manifest simply as sloped baselines that may be removed in a preprocessing step [1, 2, 7]. However, more complicated baselines and band distortions may be present when scattering effects become large. Fringes due to multiple internal reflections from thin films or microscope slides may be observed as a sinusoidal baseline in the apparent absorbance spectrum [8]. Romeo and Diem in 2005 observed contributions from

the real RI component on the edges of samples [9]. The real RI, which is related to the imaginary component by the Kramer’s-Kronig transform [10], has a derivative-like appearance; superimposed on the ideal spectrum, it results in a shift of the apparent positions of bands. While Romeo and Diem provided a method for correcting the effect, its underlying physical explanation and relation to electromagnetic scattering was rigorously established by Davis, Carney and Bhargava in 2010 [11, 12].

1.2.1 Spherical Scattering

One of the earliest exactly solved problems in electromagnetism comes from Gustav Mie in 1908, who provided an infinite series solution for scattering by spheres [13]. The Mie solution however, was not practical without computers [14]; various approximations for small and optically soft particles were provided in the meantime by Reyleigh and van de Hulst [15]. Nearly a century later in 2005, Mohlenhoff and Romeo et al first reported Mie-like scattering from the nuclei of cells in mid-infrared absorbance spectra [16]. They observed broad baseline oscillations that were consistent with the van de Hulst approximation for spherical scatterers of constant refractive index.

A method for correcting the oscillating Mie baseline was introduced by Kohler et al, whose Extended Multiplicative Scatter Correction (EMSC) process linearized the non-linear van de Hulst approximation using principal component analysis (PCA) [17]. While this was an important first step in resolving large scattering contributions from apparent absorbance spectra, band distortions were not accounted for in the EMSC model. The so-called *dispersion artifact*¹ was explained by Bassan and Byrne et al in 2009 as the manifestation of the real component of the complex refractive index in the apparent absorbance [18], much like the observations reported by Romeo and Diem for non-spherical materials [9].

Resonant Mie Scattering (R-MieS) correction was presented by Bassan and Kohler et al in 2010 as an iterative method for correcting the distorted bands using Mie theory [19].

¹It must be emphasized that these distortions are not actually an artifact – they are a real physical phenomenon due to scattering [7]

Significant limitations, however, included high computational demands and dependence on a reference spectrum. For many biological materials, the Matrigel reference spectrum was accurate [19]; after many iterations, however, the corrected spectrum would begin to resemble the reference spectrum. An efficient algorithm for fast R-MieS correction using the van de Hulst approximation for a complex refractive index was presented by Konevskikh and Lukacs et al in 2016 [20], who also in 2018 gave an improved method that reduced the effect of its convergence to the reference spectrum [21]. Further improvements were made by Solheim and Gunko et al in 2019, who published a highly optimized resonant Mie open source package [22]. At present, the primary limitation for resonant Mie correction is its reliance on user interactivity for initialization of input parameters.

Despite the significant advances in Mie scatter correction over the past decade, the algorithms have inherently been model-based and therefore limited in generality. Strong non-spherical scattering effects remain challenging to correct (if at all possible), without changes to the experiment itself. However, the observation of distorted spectral bands in both Mie and non-Mie scattering [9] motivated our group to investigate whether such effects could be understood by other physical processes. In particular, since the distorted absorbance line-shapes had a Fano-like resemblance, we sought whether Fano theory may provide any additional insight, and also whether it may be used as an alternative scatter correction approach – especially for non-spherical scattering.

1.2.2 Fano Line-shapes

Ugo Fano gave a theoretical description for asymmetric line-shapes that had previously been observed in atomic spectra of two-electron excitation decay [23]. In 1935, Fano showed that scattering experiments where quantum interference between discrete autoionization and continuous scattering probabilities occur would result in such asymmetric line-shapes [24]. A seminal paper in 1961 provided a general formula applicable to the coupling between discrete quantum states and a background continuum process [25]. While the context of Fano’s work

was based on ionization spectra, the principal mechanism behind his iconic results have been shown to be ubiquitous across many systems where wave-like resonances occur [26, 27].

Schofield et al contributions: We began our investigation into Fano resonances by considering spherical scatterers containing a single Lorentzian absorption band. It was hypothesized that if there were a Fano-like coupling between a resonance and background continuum process, it is likely that the broad oscillating baselines observed in Mie scattering [16, 17] would be the background very process that couples to absorption bands causing the Fano-like appearance. Indeed, we showed in 2019 (Chapter 2) that Fano line-shapes may occur in absorbance spectra of scattering dielectric spheres, and that the Fano parameters are related to the broad background oscillations [28].

Comparison with other work: To our knowledge, the modeling of Fano line-shapes from *absorbing* dielectric spheres has not been reported previously. Limonov and Rybin et al published a Nature Photonics review in 2017 providing a comprehensive overview of Fano resonances in many systems, including spheres and cylinders [27]. The significant difference separating our publication from their work is the underlying physics producing the Fano line-shape. Namely, they demonstrate that Fano line-shapes occur due to a coupling between resonating Mie modes and a background component. This is in contrast to our results where discrete resonances are due to Lorentzian absorption bands (from molecular vibration resonances). In fact, the Fano line-shapes appear in two very distinct domains: Limonov and Rybin et al show its occurrence for relatively large dielectric constant values ($\epsilon \sim 60$), whereas our results are valid for weak dielectric values ($\epsilon \sim 1.3$). In particular, we show that the Fano line-shape appears as the limiting behavior of weak Mie scattering in the highly specific case of an isolated Lorentzian absorbance band. The observed effect is due to a superposition of the real and imaginary RI components, which is also consistent with Romeo and Diem’s observations in 2005 for non-spherical samples [9].

The specific case of an isolated Lorentzian absorbance band is not very realistic for most systems, as even pure chemicals may have multiple vibrational bands [1, 2]. Since it is

therefore very difficult to manufacture an experiment adhering to the requirements of a homogeneous sphere with a weak, isolated absorbance band embedded in a non-absorbing medium whose refractive index is close to that of the sphere, the results in Chapter 2 have only theoretical appeal. However, by relaxing the restriction of weak and isolated bands, the same mathematical approach used for single Fano bands may be generalized for practical applications in the mid-infrared. In Chapter 3, a multi-peak modeling approach is presented with an experimental demonstration. While strictly speaking the Fano line-shape occurs for isolated resonances, the generalization to multi-peak modeling was motivated by the Fano-like appearance of the bands and the results for isolated bands in Chapter 2. This generalized Fano effect can therefore be understood as a superposition of the real and imaginary RI components, where the strength of each is wavelength-dependent and analytically given (in the case of spherical scattering) by Mie theory.

The approach for multi-peak Fano modeling allows one to estimate the imaginary RI (up to a scaling factor) when its composition is approximately composed of Lorentzian oscillators. It also estimates a Mie parameter containing the product of the sphere’s radius and relative RI difference Δ (i.e., the difference between the sample’s average RI and the medium’s). Therefore, if the size is known (e.g., from brightfield measurements, or the manufacturer), the value of Δ may be estimated – which also determines the correct imaginary refractive index scaling. We demonstrate recovery of a portion of the imaginary RI from measurements of a polystyrene bead of known size, embedded in a potassium-bromide medium.

In certain instances, having the imaginary RI may be more valuable than the pure absorbance spectrum. The imaginary RI is an inherent property of the sample, providing very similar chemical information as the absorbance but without dependence on the sample’s thickness [10, 29]. However, much work remains to be done if the multi-peak Fano approach is to compete with the latest, highly efficient Mie scatter-correction methods [22]. Presented in Chapter 3 is a very basic algorithm for both peak detection and fitting. Immediate improvements in stability and performance may be made by implementing an established

algorithm for non-linear least squares fitting, such as the Levenberg-Marquardt method [30, 31]. Statistical measures for selecting dielectric band models and distinguishing signal and noise may also be utilized, such as the Akaike Information Criterion [32, 33].

However, the value of Fano and multi-peak Fano fitting is not limited to explicit scatter correction. Often, curve fitting is applied using sums of Lorentzians or Gaussians [1, 2] using, for instance, the Levenberg-Marquardt method [34]. The methods that have been applied in our work on spheres strongly suggests that even for non-spherical scatterers, proper curve-fitting should also account for the real RI component. This is also supported by previous observations by Romeo and Diem [9], along with the work of Davis, Carney and Bhargava [11, 12]. For example, an investigation of mineral biological tissues in 2015 performed peak fitting using the Levenberg-Marquardt method with Lorentzian bands [35]. Observations of their spectra however, show the signature Fano-like characteristics, and may therefore have benefited from including the real RI component.

1.3 Hyperspectral Infrared Spectroscopy

Until recent decades, single infrared spectra would be measured for bulk, homogeneous materials. Therefore, any chemical inhomogeneities are approximately averaged over the measured field of view (FOV). Early methods for FTIR hyperspectral imaging were possible by raster scanning with a narrow FOV, although the process is lengthy and inherently limited in resolution. In recent decades, development of focal plane array (FPA) detectors have provided researchers with rapid FTIR hyperspectral imaging capabilities. In hyperspectral imaging, each pixel of an image contains a spectrum that is approximately averaged along the optical axis (i.e., the sample’s depth), providing a two-dimensional mapping of chemical inhomogeneities across a sample [36].

Recently, a novel realization of three-dimensional hyperspectral infrared imaging using computed tomography (CT) has been demonstrated [37]. Three-dimensional voxelated spec-

tra are capable of revealing distinct chemical depth layers that would otherwise be mixed together. For instance, these methods have been applied by Luca Quaroni, et. al., who report subcellular resolution by discerning nuclei and vacuole from their cellular wall [38]. Their results offer an alternative approach for distinguishing distinct spectra from components within cells without complimentary methods such as fluorescence staining [39], or the need to grow cells in a controlled process [40]. Tomographic FTIR has also been important in cases where non-destructive chemical analysis is required, such as in the investigation of a meteorite grain [41].

While tomographic FTIR is very promising, instrumental and theoretical restrictions have limited the applicability to all but a small subset of samples. First, CT reconstruction algorithms require a large set of sample orientation angles that cover a full 360° range [29, 42]. Therefore, CT performs optimally on small cylindrically-bound samples that are no more than about $20\text{ }\mu\text{m}$ in radial extent (to avoid defocus and large absorption artifacts). As many biological films such as cryotome-sliced tissues are planer (with a lateral extent that may be on the order of centimeters), the quality of CT reconstructions on these type of samples will suffer due to the restricted range of measurement angles.

Methods for improving the so-called “missing wedge” problem in limited-angle tomography remain an active interest to the CT community. Iterative regularization methods use physical constraints such as RI positivity [43, 44], while other recent advances have utilized the latest state-of-the-art techniques, including compressive sensing [45–47] and neural networks [48]. Significant advances in digital breast tomosynthesis, where limited-angle CT is desired to reduce radiation exposure, have been made by optimizing geometry and algorithms [49, 50]. Similarly, laminography methods have shown that missing wedge artifacts may be reduced with monochromatic radiation and proper parallel-beam (or plane-wave) geometry, as opposed to focused (cone-beam) illumination [51].

However, the second major limitation faced when adopting CT to microscopic samples in the infrared is due to the effect of scatter. There are two fundamental reasons that one

would expect scatter to manifest in IR measurements:

1. Whereas in classical x-ray CT the refractive index (RI) is close to unity for tissues [52], the average RI for biological materials in the infrared region may be on the order of 1.3 to 1.6 [53, 54].
2. Since we are measuring samples whose extent (or features of interest) are on the order of the radiation wavelength, geometrical ray-optics is an insufficient approximation [55].

The first of these points means that unfortunately, refraction and multiple scattering effects such as fringes and shape resonances must be expected for all but the smallest of samples whose dimensions do not exceed by very much the radiation wavelength [56]. The second point implies that a more accurate model of the physical situation should account for the wave nature of the optical system. Diffraction tomography (DT), for example, is a well-established method for wave-like systems such as acoustics and optics [29, 42]. However, direct application of DT to FTIR microspectroscopy is challenging for two reasons. First, standard DT approximations (i.e., Born and Rytov) require weak scattering which is difficult to satisfy for the relatively large RI values often encountered in for biological materials. Second, the lack of spatial coherence and phase information in commercial FTIR systems prohibits the use of standard DT algorithms.

1.3.1 Electromagnetic Phase

Electromagnetic scattering involves interactions of the complex electric field, which contains both amplitudes and phases. In particular, the field's phase provides crucial information about how the field has propagated and interacted with different media [56, 57]. However, most imaging devices only respond to the field intensity (averaged over very many oscillation cycles), and therefore cannot directly measure the field's phase [57, 58].

Diffraction phase microscopy provides contrast information that is important for topographic details, such as accurate thickness profiles for homogeneous red blood cells [59, 60]. More broadly, quantitative phase imaging (QPI) are a class of techniques that image the phase shifts from effectively transparent samples (such as cells) to provide visual and quantitative contrast [61, 62]. This phase information is useful in providing additional physical insight such as cell dry mass (an important quantity when studying cellular development and pathology) [63], or the dynamics of cell neurons under stress, which changes the observed phase [64].

Many phase retrieval methods exist that require very few modifications from existing microscopic systems [57, 65, 66]. For instance, Teague related the irradiance and phase with the transport of intensity equation (TIE) in 1983 [67]. Subsequently, Streibl showed in 1984 that using the TIE, phase may be recovered from measurements of the irradiance over multiple focus positions of a sample [68]. The TIE method is appealing for its simplicity (e.g., can be used with brightfield microscopes), and also its inherent phase unwrapping ability. That is, the recovered phase is not bounded by modulo 2π as is usually obtained in interferometric setups [69]. There are, however, a number of limitations that have precluded us from adopting it for FTIR hyperspectral imaging. The first is that the TIE method is predominantly used for phase-only objects; large errors may be introduced for absorbing objects without modifications to the experiment [70, 71]. Second, even when the TIE assumptions are valid, the method involves solving a second-order differential equation, which requires user-specified boundary conditions that may give erroneous results if chosen incorrectly. The TIE method is also prone to artifacts due to its sensitivity to noise, although these may be reduced using a larger number of measurements [72–74]. Ultimately, the fact that large absorbances and noise are often measured in FTIR compared with typical brightfield imaging, and the additional measurement overhead required, interferometric methods such as holography have stronger appeal for mid-infrared spectroscopy.

1.3.2 Holography

The problem of imperfect optics in electron microscopy led Dennis Gabor in 1948 to discover the holographic process, wherein a scattered field’s phase is recorded through its interference with a reference wave [75, 76]. Gabor’s “in-line holography” method records the interference between a source field and small scattering objects that lie in its path to the detection plane (see Appendix 5.2.5). Reconstructions are performed by illuminating the (semi-transparent) recording with the reference field (or, in Gabor’s case: a reference field with a different wavelength to perform magnification). This setup is limited, however, since the recording contains extraneous and ambiguous information. That is, on reconstruction, not only is the source field inseparable from the desired object field, but a conjugate of the object field is also superimposed with the desired object field. It wasn’t until the availability of lasers (which had superior coherence properties) in the early 1960s, that pioneering work by Leith and Upatnieks propelled the field of holography into mainstream. Most notably, they showed that a separation of the object field from its conjugate and reference field could be achieved with an off-axis configuration [77, 78].

Digital holography has afforded the ability to digitally record and reconstruct wave fields from holograms [79]. Aside from being a substantially faster process, a significant benefit is that expensive lenses and optical components may be replaced with digital filters. Furthermore, iterative algorithms may be used that, for example, remove the reference and conjugate images (a.k.a., the “twin image”) in Gabor’s in-line setup [80, 81], or suppress out-of-focus contributions from three-dimensional optical sections of weak scatterers by deconvolution [82, 83]. Above all, holography is a very versatile technique for obtaining phase information, which is crucial quantity for a whole breadth of applications [56] (see Sec. 1.3.1).

There are a number of difficulties with holography however, such as generally more complicated and vibration-sensitive setups [84, 85]. Digital holography is also very demanding of pixel count and small pixel pitch [85], and therefore tends to be more limited in achievable resolution (especially with off-axis configurations). Another consideration is the impact of

speckle, which are random noise-like intensity patterns due to surfaces or features that are rough on the scale of the wavelength [86]. In and of itself, speckle contains very important information about the sample [86, 87], however when conflated with optical defects, instrument and photon noise, they present as artifacts that degrade focused image quality [88]. A recent 2018 overview of speckle reduction techniques and denoising algorithms are given by Bianco and Memmolo et al [89]. It is not evident at this time the degree to which speckle noise will be an issue in FTIR spectroscopy of biological materials.

The case for using digital holography with FTIR is strong since additional phase information may help improve scatter correction and three-dimensional hyperspectroscopy. Additionally, it inherently provides the benefits of QPI, allowing both spectral and quantitative phase information to be obtained simultaneously. For instance, combining traditional FTIR spectroscopic pathology techniques [3, 7, 39, 90–93] with QPI [61, 63, 64] may provide powerful new analysis capabilities for histopathology without requiring correlation between multiple microscope instruments.

However, a practical realization of infrared digital holography is met with a few challenges, especially when implementing it with existing FTIR systems. First, holography requires a spatially coherent source. Typical FTIR systems use a thermal source, which is an incoherent blackbody radiator (much like an incandescent light bulb). Synchrotron sources provide coherent illumination; however, access to such sources is limited, but also not practical for compact design. Supercontinuum (SC) [94] and quantum cascade (QC) lasers [95] are a fast-growing solution offering powerful performance and compactness, however full continuous mid-IR spectral coverage is not yet possible.

Direct implementation of lasers with typical bench-top FTIR systems is also challenging since holography requires very particular optical arrangements with high-quality components. Since typical FTIR microscopes use a spatially incoherent source, the image quality is much more forgiving to optical defects such as dust and scratches. With coherent laser sources, however, we found that these defects present as a large number of Fresnel-like fringes at

the detector. Furthermore, reflecting Schwarzschild imaging objectives are typically used in FTIR systems, which contains a central obstruction held in place by a number of arms, all of which block and/or scatter laser radiation, severely reducing the hologram quality. The use of spatial filtering with other components such as beamsplitters and refractive optics also proved challenging due to the restricted working spaces within the microscope. It is for these reasons that building a customized holographic FTIR microscope from the ground-up was a preferable solution over direct integration with an existing microscope.

Schofield et al contributions: Described in Chapter 4 is our design for holographic FTIR, based on the Mach Zehnder interferometer (MZI) [96, 97]. The primary modification from the classical MZI is the addition of a closed-loop translation stage, which allows interferograms to be collected by sweeping over the path-length difference, as it is traditionally performed in FTIR. The mathematical principles of Fourier-transform spectroscopy (FTS) are extended to our Fourier-transform holographic spectroscopy (FTHS) design, where a complex spectrum related to the amplitude and phase of the sample is obtained. The FTHS process is shown to be a generalized version of phase-shifting holography [98], applicable to broadband rather than monochromatic illumination.

Comparision with other work: While many phase-shifting approaches have been reported for multi-wavelength and broadband illumination [85, 99, 100], we have not found any whose purpose is to extract hyperspectral holograms from transmission-type experiments in the style of FTIR spectroscopy. Our design presented in Chapter 4 for FTHS shares a few similarities with low coherence spectroscopy (LCS), heterodyne holography, and optical coherence tomography (OCT). OCT often is concerned with surface and depth profiling, and therefore uses a Michaelson interferometer where one of the mirrors is replaced with the sample of interest. Similarly, LCS is a spectroscopic-based OCT method [101], which for example has been used for in-vivo layered spectroscopic measurements of skin [102]. Transmission OCT has been used with scattering models to distinguish multiple scattering in turbid media using a Mach-Zehnder setup with balanced reference and sample optical

paths [103]. Another transmission OCT method has been reported by Trull et al in 2015, who recover group RI, along with spectral absorbance and scattering coefficients for bulk homogeneous materials in the visible [104, 105].

The design and principals of operation of transmission OCT [104] are very similar with our FTHS method in (Chapter 4), although with a few differences. First, our FTHS method is more generalized than the design presented by Trull et al, whose methods were developed for bulk, homogeneous samples (they acknowledge however, without detail, that their methods may be extended to inhomogeneous samples). In fact, FTHS is inherently holographic-based, and makes no a priori assumption about the sample. That is, FTHS obtains a hologram of the transmitted field for each wavelength in the spectrum. Having a hyperspectral hologram allows digital holographic methods to be applied on a per-wavelength basis, such as autofocusing, back propagation, phase contrast (see Sec. 1.3.1). Second, while Trull et al obtained spectra in the near-IR, our focus is on mid-infrared spectroscopy. Since FTHS shares in its similar design with transmission OCT, it has the additional benefit over typical monochromatic holography that the group phase is naturally unwrapped.

1.3.3 FTIR Holography: Future Work

As mentioned previously (Sec. 1.3.2), an immediate application of FTHS is the simultaneous acquisition of both FTIR and QPI information. Combining these techniques may provide correlated pathological methodologies that improve analysis. For instance, it is common practice in FTIR to normalize absorbance spectra from biological samples to the Amide I/II peaks [7]. This helps reduce thickness variations from impacting chemical classifications, however it inherently assumes that the protein concentration is homogeneous throughout the sample. Therefore, the phase may be used to provide additional concentration information (such as cell dry mass [63]), which may be combined with traditional FTIR analysis to resolve this normalization limitation. While combination of FTIR and QPI may indeed provide powerful new analysis techniques for biological pathology, we are also motivated by

the goal of improving three-dimensional FTIR hyperspectral imaging.

Diffraction Tomography

The relatively large RI for typical biological samples in FTIR means that weakly scattering approximations such as Born and Rytov for three-dimensional imaging may lead to severe reconstruction artifacts [29, 42]. Techniques for multiple scattering have only recently begun gaining interest compared to single-scattering using the Born and Rytov approximations [106]. This is likely due to computational demand required for dealing with the non-linearity of the inhomogeneous wave equation solution, and that practical solutions such as embedding samples in a RI-matched medium are more feasible. For example, Sung et al performed diffraction tomography in cells flowing through an RI-matched microfluidic channel [107, 108]. However, embedded mediums are often difficult to make, or come at the cost of reduced spectral coverage (e.g., in the case of aqueous solutions, mid-infrared spectra are dominated by very strong H₂O bands), or even changing the chemical signature [1, 7].

Liu et al presented in 2017 a novel, but computationally demanding technique (using compressive sensing) for reconstructing from larger RI media, where multiple scattering is modeled with the full non-linear Lippmann-Schwinger equation (i.e, the inhomogeneous Helmholtz solution) [109, 110]. A more computationally efficient approach was given by Soubies et al in 2017 [111], while alternative methods were presented in 2018 using deep learning (Sun et al [112]), and learned tomography (Lim et al [113]). Meanwhile, Lim et al show in 2017 that multiple scattering effects may in fact be exploited to achieve super resolution, while also significantly improving the missing-cone problem [114].

Schofield et al contributions: Due to the large amount of data in three-dimensional hyperspectral imaging (there may be $\sim 10^3$ per-wavelength volumetric reconstructions required), a computationally efficient method is desirable. While Soubies et al achieved efficient reconstructions, their peak performance is still on the order of 10 minutes per wavelength on a higher-end server (Dell PowerEdge T430) [111]. Even with only a hundred or so wavenum-

bers, this amounts to about a day of computation time. To this end, we investigate in Chapter 5 (Sec. 5.1) whether the inherent spectral information may be used to improve diffraction tomography reconstructions. In particular, a few physical assumptions about the sample are proposed with the goal of inverting the exact Lippman-Schwinger equation and removing multiple-scatter effects using the spectral axis. However, further work including simulations, or preferably experimental data, is necessary to test the validity of these assumptions.

3D Deconvolution

The limitations of applying classical tomography to typical FTIR (as discussed in Sec. 1.3), including the missing-cone problem for planar film-like samples, motivated an approach for optical sectioning that would exploit the natural defocusing of the sample at different depths. Chapter 5 (Sec. 5.2) discusses a method for filtering out-of-focus portions of the sample at different depths, which was inspired by convolutional neural networks (CNNs) [115].

Previous methods had been developed that, for example, estimate depth from focus [116, 117], or simulating infinite depth of focus in typical brightfield measurements [118, 119]. However, these techniques were primarily developed for surface reconstructions; transparent media, which are usually the subject of FTIR spectroscopy, requires a different treatment. We approached the problem first using three-dimensional deconvolution [120, 121], followed by an algorithm loosely based on CNN theory [115].

While the three-dimensional deconvolution approach did not achieve the desired results, our CNN algorithm showed promise. However, an automated translation stage was not available to us at the time; due to the lengthy acquisition times and required positioning precision, the work was put on hold until further testing and optimization could be performed. The method also did not take into account multiple scattering (e.g., focusing and shape resonances).

Future work may revisit the approach using automated stage control and holographic

techniques, such as Fourier ptychography microscopy [122]. Three-dimensional ptychographic transmission microscopy has been demonstrated by Maiden et al using a multi-slice approach for thin samples [123], while extending their methods to thicker samples in 2014 [124]. The method is attractive since it inherently accounts for multiple scattering. Ptychography has also been used to achieve super-resolution [125], and also a non-holographic approach has been demonstrated using LEDs [126]. Finally, a similar method of performing diffraction tomography using a through-focus stack was achieved by Kim et al with white light [127].

1.4 Thesis Overview

In **Chapter 2** we demonstrate on simulations that Fano line shapes in FTIR transmission spectra can occur for homogeneous spheres that possess a weak and isolated absorbance band. Furthermore, by fitting Fano line shapes to these bands, recovery of the peak position and pure absorption strength can be obtained with high accuracy. Additionally, for small and optically soft spherical scatterers, recovery of one or the other of the constant refractive index difference from its embedded non-absorbing medium, or the sphere’s radius (given approximate knowledge of the other), is possible.

Chapter 3 generalizes the results from Fano modeling, extending its validity to multiple, stronger, overlapping bands. Also presented is an algorithm for modeling such Mie spectra of scattering spheres. The algorithm is demonstrated on simulated spectra, along with an experimental application on a measurement of polystyrene microspheres embedded in a potassium-bromide medium. Future work and applications for Fano modeling are discussed at the end of the chapter (Sec. 3.6).

A microscope design and mathematical details for obtaining spatially- and spectrally-resolved holographic mid-infrared images are presented in **Chapter 4**. Future work for extending IR microscopic techniques using holography are discussed in **Chapter 5**. In par-

ticular, a spectral-based method for handling the multiple-scattering problem in diffraction tomography for typical FTIR biological samples is discussed in Section 5.1, while a technique for non-holographic digital confocal microscopy, with possible extension to holographic FTIR is presented in Section 5.2.

Chapter 2

Spherical Scattering Part I: Isolated Peaks and the Fano Effect

Mid-infrared absorbance spectra obtained from spatially inhomogeneous and finite samples often contain scattering effects characterized by derivative-like bands with shifted peak positions. Such features may be interpreted and accurately modeled by Fano theory when the imaginary part of the complex dielectric function is small and Lorentzian in nature—as is the case for many biological media. Furthermore, by fitting Fano line shapes to isolated absorbance bands, recovery of the peak position and pure absorption strength can be obtained with high accuracy. Additionally, for small and optically soft spherical scatterers, recovery of one or the other of constant refractive index or radius (given approximate knowledge of the other), is possible.

2.1 Introduction

Asymmetrically distorted spectral peaks are often encountered in FTIR absorbance spectra—particularly noticeable in the Amide-I band, where a derivative-like line shape may be observed [2, 17, 128]. Previously, it has been shown that these derivative features occur due to a non-linear mixing between the absorbance and dispersive spectra on top of a smooth-

varying broadband baseline [16, 17, 19, 128]. In such cases, identification of chemical bands in a scattering sample may be deceptive, as the distorted bands frequently suffer from a shift in peak position [17, 19, 128]. Identification and correction of such distortions are critical for FTIR spectroscopy if one seeks a quantitative understanding of the sample under investigation.

2.1.1 Fano Resonances

In atomic spectroscopy, interference between discrete state transitions and a background continuum of states results in a particular distortion of the line shape, characterized by a derivative-like appearance of an energy band. This interference was first described by Fano, who models the relative scattering cross-section σ/σ_0 for an energy E by the equation [25]

$$\frac{\sigma}{\sigma_0} = \frac{(q + \epsilon)^2}{1 + \epsilon^2} - 1, \quad (2.1)$$

where q is an asymmetry parameter (often referred to as the Fano parameter), and the reduced energy ϵ is expressed in terms of the resonant peak energy E_r , and peak full width at half maximum Γ_E as

$$\epsilon = \frac{E - E_r}{\frac{1}{2}\Gamma_E}. \quad (2.2)$$

The Fano parameter q introduces asymmetry in an otherwise Lorentzian band shape, as can be seen in Fig. 2.1 for various q . As $q \rightarrow 0$ the peak becomes inverted, while finite values of q produce an asymmetric line profile with a shift in the peak position away from the resonance at $\epsilon = 0$. The direction of peak shift is determined by the sign of q : positive q shifts the peak towards positive ϵ , while negative q shift towards negative ϵ (compare $q = 1$ and $q = -2$ in Fig 2.1). At $|q| = 1$ the line shape becomes perfectly antisymmetric about $\epsilon = 0$ (occasionally referred to as anti-Lorentzian in this paper). As $|q| \rightarrow \infty$ however, the line shape approaches a symmetric Lorentzian centered about the resonance energy E_r

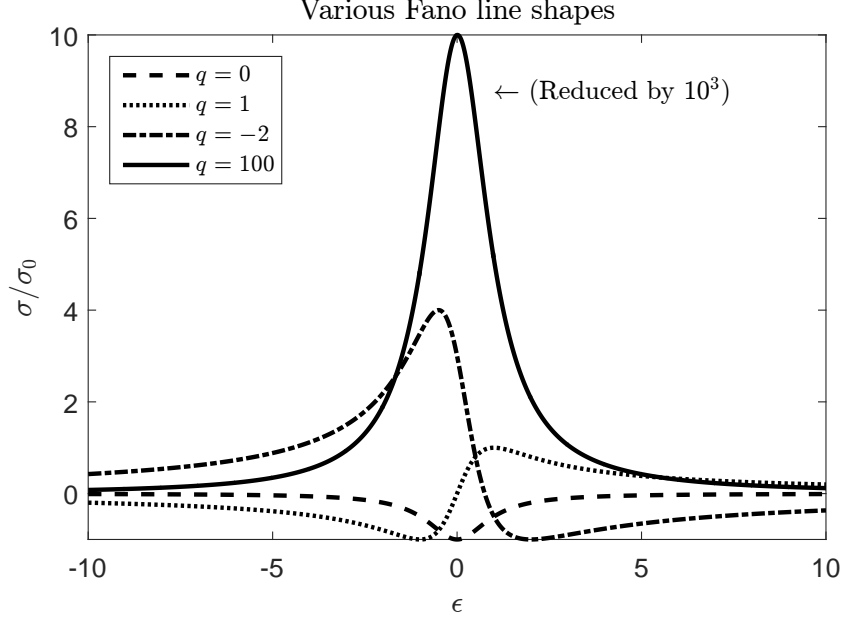


Figure 2.1: Fano line shapes for various values of the Fano parameter q . The line shapes are plotted in terms of the reduced coordinate $\epsilon = (E - E_r)/\frac{1}{2}\Gamma_E$, where $\epsilon = 0$ corresponds to the exact resonance position $E = E_r$. For finite $|q| > 0$, the peak shifts away from the resonance at $\epsilon = 0$, such that the peak position alone is insufficient for identifying the resonance energy. For $q > 0$, the peaks shift toward positive ϵ , and toward negative ϵ for $q < 0$.

($\epsilon = 0$)

$$\frac{\sigma}{\sigma_0} \approx \frac{q^2}{1 + \epsilon^2}. \quad (2.3)$$

Such limiting behavior as $q \rightarrow \infty$ can be seen in Fig. 2.1 for $q = 100$, where the line shape is Lorentzian in appearance.

While Fano theory was originally developed in the context of quantum spectroscopy [24], it has since been shown to be a general interference phenomenon applicable to a wide range of classical and quantum resonating systems [26, 129–131]. Generally speaking, Fano resonances occur due to a coupling between multiple oscillators; in many physical systems this can be interpreted as an interference between a resonance of interest and a “background process.”

2.1.2 Fano Line Shapes in FTIR Spectroscopy

Asymmetric, derivative-like peaks are often observed in FTIR transmission and absorbance spectra, attributed to the “dispersion artefact” [18], which involves a distortion of the transmission spectrum due to reflectance line shapes [128, 132]. Absorbance spectra that contain such dispersion effects, however, also share these signature features and bear a striking resemblance to Fano line shapes. With this motivation, we evaluate whether observed spectral features may be interpreted as Fano resonances, where sharp resonating bands are coupled to a slowly-varying background process. Above all, we evaluate whether these features can be accurately modeled with Fano theory, and whether they can be corrected (i.e., related to a pure Lorentzian absorption line shape), and if so, to what extent and under what conditions.

Previous work has shown that very small spherical scatterers may exhibit “unconventional” Fano resonances [133]. These Fano line shapes present as a function of the dielectric function, manifesting from interfering shape resonances and occurring in particles with large refractive indices in the absence of absorption. In contrast, our work focuses on absorbing scatterers with smaller refractive indices (applicable to typical biological media), and instead of presenting as a function of the dielectric function, as in [133], the resonances in our work appear as a function of wavenumber, as is appropriate for FTIR spectroscopy.

Using Mie theory, which models the interaction of electromagnetic radiation with an absorbing sphere, we show that Fano line shapes emerge in certain limiting cases, when scattering effects are sufficiently weak. For such situations, a link between an absorbing sphere’s physical size and constant refractive index can be established to the parameters of a Fano line shape that has been fit to the data. We also show that using our Fano approach, the bulk absorptivity, characteristic for an infinite medium, can be extracted from the line shapes measured for finite (spherical) samples.

Presented are results for various simulated spectra using Mie scattering theory, which have been fit with a Fano line shape. We establish that accurate recovery of the peak resonance shift for an isolated absorbance is possible using Fano theory. Additionally, extraction

of the pure absorbance strength is obtained for small, optically soft spheres. Finally, we demonstrate how Fano modeling can be used for the recovery of the constant refractive index given an estimate of the particle size, and vice versa.

2.2 Methods

One of the central goals of IR spectroscopy is the extraction of the spectral optical depth $\tau(\tilde{\nu})$ from measured transmission spectra. The spectral optical depth is a quantity that characterizes the absorption strength of an infinite medium without boundaries and interfaces. It is defined as the product of the molar extinction coefficient, $\epsilon(\tilde{\nu})$, the chemical concentration, c , of the absorber, and the propagation distance, d , of the radiation inside of the medium [10, 16, 134], i.e.,

$$\tau(\tilde{\nu}) = \epsilon(\tilde{\nu})cd, \quad (2.4)$$

where $\tau(\tilde{\nu})$, via the molar extinction coefficient $\epsilon(\tilde{\nu})$, depends on the wavenumber $\tilde{\nu}$. Inside of the medium, the intensity $I(\tilde{\nu})$ of the IR radiation propagates according to the (Boguer-) Beer-Lambert law [134], i.e.,

$$I(\tilde{\nu}) = I_0(\tilde{\nu}) \exp[-\tau(\tilde{\nu})], \quad (2.5)$$

where $\tau(\tilde{\nu})$ is defined in Eq. 2.4. This shows that the optical depth is related to the transmittance

$$T(\tilde{\nu}) = \frac{I(\tilde{\nu})}{I_0(\tilde{\nu})} \quad (2.6)$$

via

$$\tau(\tilde{\nu}) = -\ln[T(\tilde{\nu})] \quad (2.7)$$

According to convention, in chemistry, biochemistry, and biophysics, the quantity of interest is the absorbance $A(\tilde{\nu})$, defined as

$$A(\tilde{\nu}) = -\log_{10}[T(\tilde{\nu})] \quad (2.8)$$

As Eqs. 2.7 & 2.8 show, optical depth and absorbance are closely related. In fact, there is a simple linear relationship between optical depth and absorbance in such infinite media, i.e.,

$$A(\tilde{\nu}) = \tau(\tilde{\nu}) / \ln(10) \quad (2.9)$$

Just like the optical depth, the absorbance refers to a bulk property of a given substance, independent of its geometry. Therefore, if intensity propagation measurements inside of the substance could be performed in the lab, the absorbance $A(\tilde{\nu})$ is obtained from the internally measured intensities $I(\tilde{\nu})$ and $I_0(\tilde{\nu})$ via equations 2.6 and 2.8. However, such experiments are extremely difficult to perform, especially if one is interested in the absorption properties of microscopically small samples. Instead, one usually settles for measuring the transmission through thin films, single cells, or other finite-sized biological samples. This, however, immediately introduces interfaces between the embedding medium, containing the source of the IR irradiance, the sample, and the detector. These interfaces act as sources of exterior and interior reflection and scattering of IR radiation. Thus, the measured absorbance is no longer connected to the optical depth via the simple, linear relationship in Eq. 2.9, which holds only for the pure, bulk absorbance. In such cases one defines the apparent absorbance

$$\hat{A}(\tilde{\nu}) = -\log_{10} \left(\frac{\hat{I}(\tilde{\nu})}{I_0(\tilde{\nu})} \right), \quad (2.10)$$

where $\hat{I}(\tilde{\nu})$ is the measured intensity transmitted to the detector in the presence of interfaces and scattering, and I_0 is the irradiance of the sample. Thus, apparent absorbance is a good approximation of absorbance only if scattering effects on interfaces between embedding medium, sample, and detector can be neglected. Depending on the desired accuracy, even for the relatively small indices of refraction of typical biological materials, the scattering effects caused by interfaces may be too large for the apparent absorbance $\hat{A}(\tilde{\nu})$ to be an acceptable approximation of the pure absorbance $A(\tilde{\nu})$. The distorting effect of interfaces is particularly severe for approximately spherical microscopic samples, such as single cells,

and is compounded by the existence of refraction and diffraction effects. Thus, the basic task of IR spectroscopy is to extract the pure absorbance $A(\tilde{\nu})$ from the measured, apparent absorbance $\hat{A}(\tilde{\nu})$. Our method, discussed in this paper, is to deconvolve the measured line shapes containing scattering, refraction, and diffraction effects by using Fano theory, and thus to extract the pure absorbance $A(\tilde{\nu})$ from the measured, apparent absorbance $\hat{A}(\tilde{\nu})$. In order to prove the viability and power of our method, we model biological cells with spheres, since for spheres an analytical theory, i.e. the Mie theory [10, 15], is available that allows analytical insight into our methods and procedures.

2.2.1 Scattering on Spheres

When electromagnetic radiation interacts with a dielectric sphere, it undergoes a form of scattering that is analytically solved by Mie theory. An approximate equation for the extinction efficiency² Q_{ext} of an absorbing sphere of radius a and complex refractive index $\tilde{n} = n_r(\tilde{\nu}) + in_i(\tilde{\nu})$ is given by van de Hulst as [15]

$$\begin{aligned} Q_{ext}(\tilde{\nu}) = & 2 - 4 \exp \{ -\rho \tan \beta \} \left(\frac{\cos \beta}{\rho} \right) \sin (\rho - \beta) \\ & - 4 \exp \{ -\rho \tan \beta \} \left(\frac{\cos \beta}{\rho} \right)^2 \cos (\rho - 2\beta) \\ & + 4 \left(\frac{\cos \beta}{\rho} \right)^2 \cos 2\beta \end{aligned} \quad (2.11)$$

where

$$\rho(\tilde{\nu}) = 4\pi a \tilde{\nu} (n_r(\tilde{\nu}) - 1) \quad (2.12)$$

$$\tan \beta = \frac{n_i(\tilde{\nu})}{n_r(\tilde{\nu}) - 1} \quad (2.13)$$

In the vicinity of chemical absorption bands, $n_r(\tilde{\nu})$ exhibits large and rapid variations as

²In the geometric-optics limit and for a wide enough detector aperture, the extinction efficiency Q_{ext} is related to the transmittance $T = I/I_0$ via $T = 1 - (g/G)Q_{ext}$, where $g = \pi a^2$ is the geometric cross section of the sphere, a is the radius of the sphere, and G is the detector aperture (see [10, 20] for details).

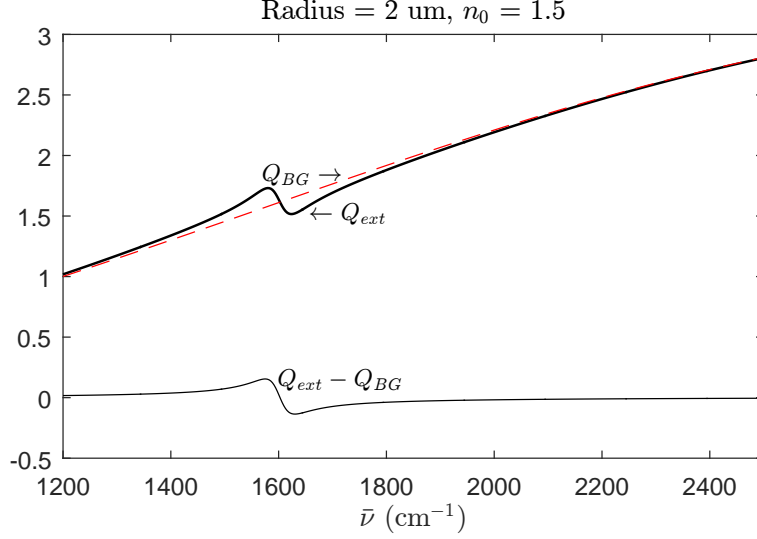


Figure 2.2: Extinction curve Q_{ext} and the Mie background Q_{BG} for a particle of radius $2\ \mu\text{m}$ and constant refractive index $n_0 = 1.5$. Removal of Q_{BG} from the extinction curve Q_{ext} leaves a curve that approaches zero away from the resonance.

a function of $\tilde{\nu}$. Away from absorption bands, however, $n_r(\tilde{\nu})$ may be approximated by a real, constant n_0 . For this constant refractive index n_0 we define the background extinction efficiency Q_{BG} according to

$$Q_{BG}(\tilde{\nu}) = 2 - \frac{4}{\rho_0} \sin \rho_0 + \frac{4}{\rho_0^2} (1 - \cos \rho_0) \quad (2.14)$$

where here

$$\rho_0(\tilde{\nu}) = 4\pi a \tilde{\nu} \Delta, \quad \Delta \equiv n_0 - 1 \quad (2.15)$$

Denote by $Q' \equiv Q_{ext} - Q_{BG}$ the removal of the background Q_{BG} from Q_{ext} , revealing the “interesting” spectral features (see Fig. 2.2). We then consider the behavior of Q' for a Lorentzian line shape $n_i(\tilde{\nu}) = f_0/(1+z^2)$ whose peak strength is f_0 , and the reduced spectral variable

$$z = \frac{\tilde{\nu} - \tilde{\nu}_r}{\Gamma_{\tilde{\nu}}/2} \quad (2.16)$$

is defined for a resonance about ν_r , with a peak width at half maximum $\Gamma_{\tilde{\nu}}$ in the same spirit as in Eq. 2.2. It is then shown in the Appendix that, to first order in f_0 , a local expansion of Q' about $\tilde{\nu} = \tilde{\nu}_r$ gives

$$Q'_{\text{exp}}(\tilde{\nu}) \equiv \frac{8}{\rho_r^2 \Delta} \left\{ \Phi_1(\rho_r) \left(\frac{f_0}{1+z^2} \right) + \Phi_2(\rho_r) \left(\frac{f_0 z}{1+z^2} \right) \right\} \quad (2.17)$$

where

$$\rho_r \equiv \rho_0(\tilde{\nu}_r) = 4\pi a \tilde{\nu}_r \Delta \quad (2.18)$$

and $\Phi_1(\rho_r)$ and $\Phi_2(\rho_r)$ are expressions involving sines and cosines of ρ_r (see Eqs. 2.47 & 2.48). To understand the behavior of $\Phi_1(\rho_r)$ and $\Phi_2(\rho_r)$, we further expand Eq. 2.17 to second order in Δ

$$\begin{aligned} Q'_{\Delta}(\tilde{\nu}) \equiv & \left(\frac{4\rho_r}{3} - \frac{2\rho_r^3}{5} \right) \left(\frac{f_0/\Delta}{1+z^2} \right) \\ & + \left(\frac{4\rho_r \frac{\Gamma_{\tilde{\nu}}}{2}}{3\tilde{\nu}_r} - \rho_r^2 - \frac{6\rho_r^3 \frac{\Gamma_{\tilde{\nu}}}{2}}{5\tilde{\nu}_r} \right) \left(\frac{f_0 z/\Delta}{1+z^2} \right) \end{aligned} \quad (2.19)$$

Here, the expansion leading to Eq. 2.19 requires that ρ_r is small, which restricts the expansion's validity to a limited class of particles. However, we are only considering small ρ_r to illustrate our methods and procedures; the full local expansion for arbitrary ρ_r (Eq. 2.17) is valid for all radii and indices of refraction for relevant biological tissues, provided the peak height f_0 is small, $\Gamma_{\tilde{\nu}}/(2\tilde{\nu}_r)$ is small, and a suitable background extinction Q_{BG} can be estimated.

2.2.2 Connection to Fano Theory

We aim to model asymmetric absorbance bands using the approximations contained in Eqs. 2.17 & 2.19, with the purpose of extracting the pure absorbance A . As described in the

Appendix, directly fitting to these equations is not possible: there exists five parameters, while only four may be considered independent. In particular, Eqs. 2.17 & 2.19 may only be determined up to a scaling factor, as f_0/Δ occurs in both terms. A simple replacement of f_0/Δ with a generic scaling parameter would suffice; however, as the observed asymmetric bands resemble Fano resonances, the Fano model will instead be used to explicitly highlight the occurrence of these line shapes in Mie theory. We will show that the four Fano parameters may be predicted by Mie theory, and with them, explicit analytical results are obtained for the recovery of the absorbance A of chemical absorption bands under the conditions assumed in Eq. 2.19 (i.e., a small radius and constant refractive index). We therefore start by fitting a Fano line shape model to Eq. 2.19, and demonstrate that a connection is established between its model parameters and the scatterer's radius and complex refractive index.

To fit Fano line shapes to transmission spectra, we rewrite Eq. 2.1 in terms of the dimensionless quantity $z = z(\tilde{\nu})$ (see Eq. 2.16). The factor σ_0 serves as a scaling parameter that essentially captures the line shape's strength. It will then prove useful to break it into the following form, so that equivalence between the Fano parameters and scattering models can be easily made by inspection

$$\begin{aligned}\sigma(\tilde{\nu}) &= \sigma_0 \left(\frac{q^2}{1+z^2} + \frac{2qz}{1+z^2} + \frac{z^2}{1+z^2} - 1 \right) \\ &= \sigma_0(q^2 - 1) \left(\frac{1}{1+z^2} \right) + 2\sigma_0 q \left(\frac{z}{1+z^2} \right)\end{aligned}\tag{2.20}$$

With this form, a few observations are immediately apparent. For large $|q|$, the first term dominates and σ has the form of a symmetric Lorentzian. For finite q , a mixture of a Lorentzian and anti-Lorentzian results; when $|q| = 1$, the band shape is purely anti-Lorentzian. Furthermore, the necessity that σ is finite requires that as $q^2 \rightarrow \infty$, $\sigma_0 \rightarrow 0$ such that $\sigma_0(q^2 - 1) \rightarrow \text{Const.}$

It can be seen by inspection, comparing the extinction Q'_Δ expanded in Δ (Eq. 2.19) with the Fano model (Eq. 2.20), that the Fano parameters σ_0 and q are related to the radius a ,

absorption strength f_0 , and constant refractive index n_0 by the two equations

$$\sigma_0(q^2 - 1) = \frac{f_0}{\Delta} \left(\frac{4\rho_r}{3} - \frac{2\rho_r^3}{5} \right) \quad (2.21)$$

$$2\sigma_0 q = \frac{f_0}{\Delta} \left(\frac{4\rho_r \frac{\Gamma_{\tilde{\nu}}}{2}}{3\tilde{\nu}_r} - \rho_r^2 - \frac{6\rho_r^3 \frac{\Gamma_{\tilde{\nu}}}{2}}{5\tilde{\nu}_r} \right) \quad (2.22)$$

An additionally useful (although not independent) equation, obtained from the difference between the maximum and minimum of Q'_{exp} (also taken to second order in Δ ; see Eq. 2.46 of the Appendix), gives

$$\sigma_0(q^2 + 1) = \frac{f_0}{\Delta} \left(\frac{4\rho_r}{3} - \frac{\frac{\Gamma_{\tilde{\nu}}}{2}\rho_r^2}{\tilde{\nu}_r} - \frac{\rho_r^3}{40} \right) \quad (2.23)$$

Recovery of the pure absorbance A as defined in Section 2.2 from a Fano line shape in the case of an absorbing sphere can be achieved by noting that the absorbance strength at the resonance position $Q'(\tilde{\nu} = \tilde{\nu}_r)$ —in the limit that scattering due to a constant refractive index is negligible ($\Delta \rightarrow 0$)—approaches³

$$\begin{aligned} A &= \lim_{\Delta \rightarrow 0} \{ -\log_{10} [1 - Q'_{\Delta}(\tilde{\nu}_r)] \} \\ &= -\lim_{\Delta \rightarrow 0} \frac{1}{\ln(10)} \ln [1 - Q'_{\Delta}(\tilde{\nu}_r)] \\ &\approx \lim_{\Delta \rightarrow 0} \frac{1}{\ln(10)} [Q'_{\Delta}(\tilde{\nu}_r)] = \frac{4f_0\rho_r}{3\Delta \ln(10)} = \frac{16\pi a\tilde{\nu}_r f_0}{3\ln(10)}. \end{aligned} \quad (2.24)$$

Combining Eq. 2.21, 2.22, and 2.23, while considering only terms of order $\mathcal{O}\left(\frac{\Gamma_{\tilde{\nu}}}{2\tilde{\nu}_r}\right)$, gives an expression for A in terms of the Fano fit parameters σ_0 , q , $\Gamma_{\tilde{\nu}}$ and $\tilde{\nu}_r$

$$A \approx \frac{\sigma_0}{15} \left[15q^2 + 17 - 32q \frac{\Gamma_{\tilde{\nu}}}{2\tilde{\nu}_r} \right] \quad (2.25)$$

³For simplicity, it is assumed that the detector's aperture is set tightly about the particle, so that its geometrical area G is close to the particle's cross-sectional area g . In this case the transmittance is directly related to the extinction $T = 1 - (g/G)Q_{\text{ext}} = 1 - Q_{\text{ext}}$ (see [10, 20]). In the case that $g \neq G$, the scaling factor g/G (determined from the experimental setup) must be included in the derivation of Eq. 2.24. The results in Eqs. 2.26 & 2.27 are, however, independent of the g/G scaling factor.

Furthermore, one may have a reasonable estimate of either the material's radius a (e.g., from a bright-field measurement), or the material's constant refractive index n_0 . For either such case, the known quantity may be used to recover the other unknown (either n_0 or a) in terms of the Fano fit parameters by combining Eq. 2.21 and 2.25 for A

$$n_0 = 1 + \frac{\sqrt{10/3}}{4\pi a \tilde{\nu}_r} \sqrt{1 - \frac{\sigma_0(q^2 - 1)}{A_{\text{Beer}}}} \quad (2.26)$$

$$a = \frac{\sqrt{10/3}}{4\pi \Delta \tilde{\nu}_r} \sqrt{1 - \frac{\sigma_0(q^2 - 1)}{A_{\text{Beer}}}} \quad (2.27)$$

Finally, a note about the removal of Q_{BG} from Q_{ext} : this can be done exactly with simulated data, as the “background” Mie contribution (given by Q_{BG} in Eq. 2.14) can be subtracted from the simulated data. In practice, however, ρ_0 is unknown, and methods that estimate a suitable baseline must be employed. Such methods include EMSC [17], which estimates the broad, smoothly varying contribution Q_{BG} to the spectrum. However, the primary necessity is that an appropriate broad background Q_{BG} must be found such that, as $|\tilde{\nu} - \tilde{\nu}_r| \rightarrow \infty$, $(Q_{ext} - Q_{BG}) \rightarrow 0$ as accurately as possible.

2.3 Results

Numerical simulations, fitting, and analysis were written and conducted in MATLAB [135]. Simulations of absorption from a spherical scatterer were produced using the van de Hulst approximation Eq. 2.11. Although the size parameter $2\pi a \tilde{\nu}$ [15] depends only on the product of a and $\tilde{\nu}$, we choose to discern between particle size and resonance wave number $\tilde{\nu}_r$, to ground the analysis on a practical footing. We choose to simulate a sphere with an isolated absorption band at $\tilde{\nu}_r = 1600 \text{ cm}^{-1}$. The choice of $\tilde{\nu}_r$ is consistent with observations of Fano line shapes in the Amide-I band. Given the resonance wave number $\tilde{\nu}_r$, we vary the sphere's radius such that ρ_r (Eq. 2.18) is between about 0.1 and 2, which gives an indication for which conditions these methods are and are not valid.

Extinction spectra are simulated for 100 spheres with refractive indices and radii ranging from 1.1 to 1.5, and 0.6 μm to 2 μm , respectively. With an absorption band at $\tilde{\nu}_r = 1600 \text{ cm}^{-1}$, this corresponds to size parameters of approximately 0.6 to 2.01 near the resonance. The restriction of small ρ_r in deriving the approximated Q'_Δ (Eq. 2.19) means that the applied methods for many of these particles (particularly as n_0 becomes larger than about 1.2), are not expected to be valid.

A complex dielectric function is modeled in MATLAB [135] using wave numbers $\tilde{\nu}$ ranging from 1000 cm^{-1} to 4000 cm^{-1} , with $\approx 3 \text{ cm}^{-1}$ resolution, as

$$\tilde{\epsilon} = 1 - f_{\text{diel}} \frac{\frac{\tilde{\nu} - \tilde{\nu}_r}{\Gamma_{\tilde{\nu}}/2}}{1 + \left(\frac{\tilde{\nu} - \tilde{\nu}_r}{\Gamma_{\tilde{\nu}}/2}\right)^2} + i f_{\text{diel}} \frac{1}{1 + \left(\frac{\tilde{\nu} - \tilde{\nu}_r}{\Gamma_{\tilde{\nu}}/2}\right)^2} \quad (2.28)$$

where we have chosen a strength $f_{\text{diel}} = 0.1249$, width $\Gamma_{\tilde{\nu}}/2 = 26 \text{ cm}^{-1}$, and peak position $\tilde{\nu}_r = 1600 \text{ cm}^{-1}$. The complex refractive index $\tilde{\eta}$ is then calculated as $\tilde{\eta} = \sqrt{\tilde{\epsilon}}$, resulting in a complex refractive index whose imaginary component n_i has a peak strength of $f_0 \approx 0.06$. The value of f_{diel} (and hence f_0) was chosen to bring the absorbance of a bulk measurement with an optical depth $d \sim 10 \mu\text{m}$ (using Eq. 2.9) just under unity. The real part of $\tilde{\eta}$ fluctuates with a small amplitude in the immediate vicinity of 1; we add various values of Δ such that the constant refractive indices fall between about $n_0 = 1.1$ and 1.5 for each of the particles.

We first compare the accuracy of the expansions Q'_{exp} and Q'_Δ (Eq. 2.17 and 2.19) to the exact Q' for selected simulations in Fig. 2.3 (with the associated parameters in Table 2.1).

Next, fits are made to the simulated spectra, which provide the Fano fit parameters: σ_0 , q , $\tilde{\nu}_r$, and $\Gamma_{\tilde{\nu}}$. Fitting is performed using a least-squares gradient descent algorithm in MATLAB [135]. Fano fits and extracted Lorentzian line shapes for select simulations are shown in Fig. 2.4. The examples selected in Fig. 2.3 and 2.4 encapsulate the average and extreme cases of the results.

The error in recovered resonant positions $\tilde{\nu}_r$ for various constant refractive indices n_0 are

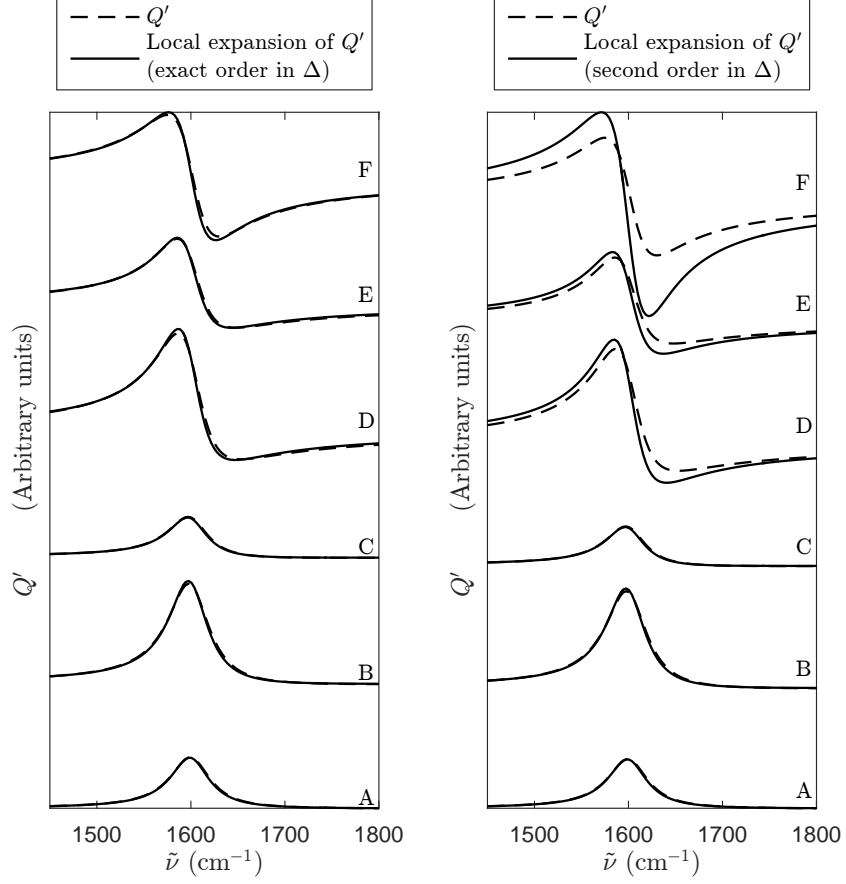


Figure 2.3: Comparing select simulated Mie spectra for a single absorbance band in the vicinity of 1600 cm^{-1} with its local expansion. The associated constant refractive index, radius, size parameters and errors are given in Table 2.1. **Left:** Simulated spectra Q' and their local expansion Q'_{exp} (Eq. 2.17, to first order in f_0 exact in Δ). **Right:** Simulated spectra Q' and its local expansion Q'_{Δ} (Eq. 2.19, to first order in f_0 , and second order in Δ).

shown in Fig. 2.5. We also estimate the constant refractive index n_0 for each particle using Eq. 2.26, with the assumption that the radius is known. We show how these estimates of n_0 compare with exact values in Fig. 2.6 as a function of q (left), and of the size parameter $2\pi a\tilde{\nu}_r$ (right).

Finally, the percent error in extracted Lorentzian peak heights for select simulations are shown in Fig. 2.7 (solid markers). This can be compared with the absorbance strengths that would be obtained by naïvely subtracting the anti-Lorentzian component of the Fano line, shown in Fig. 2.7 (hollow markers). Removal of the dispersive component gives an apparent

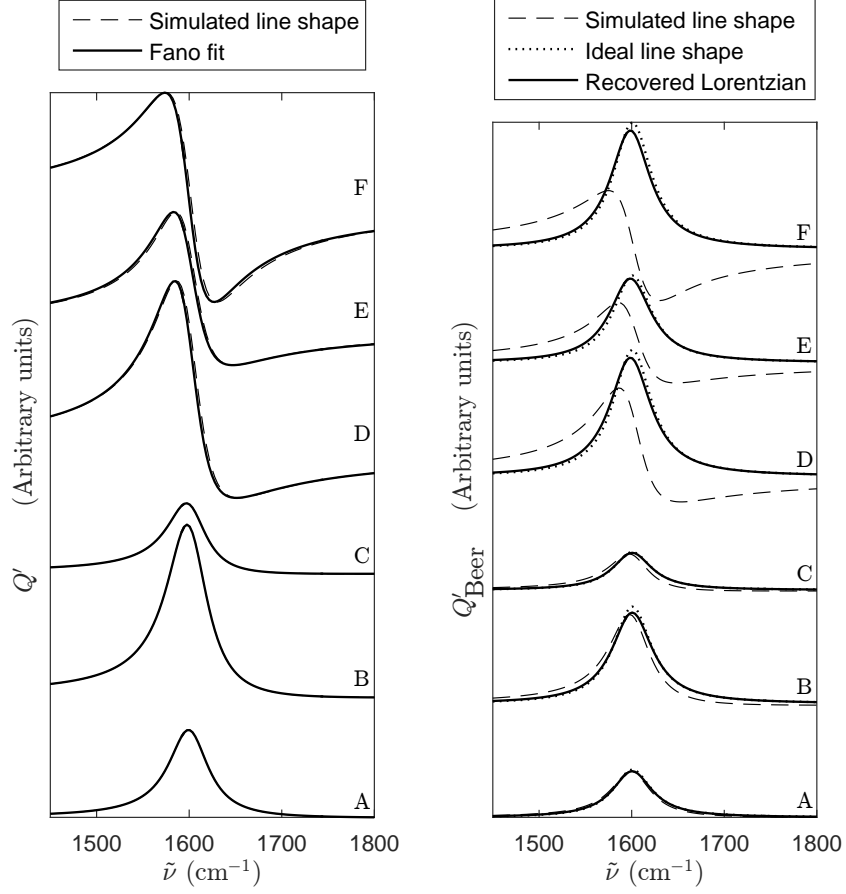


Figure 2.4: Select simulated Mie spectra for a single absorbance band in the vicinity of 1600 cm^{-1} . The associated constant refractive index, radius, size parameters and Fano fit parameters q are given in Table 2.1. **Left:** Simulated spectra with the background removed and the associated Fano fits. **Right:** The ideal Lorentzian line shapes that would be measured in the absence of scatter effects, and the recovered Lorentzian line shape using the Fano fit parameters.

absorbance

$$\sigma_{\text{abs}} = \sigma_0(q^2 - 1) \quad (2.29)$$

2.4 Discussion

It is reasonable that the derivative line shape that arises from electromagnetic interference can also be understood as interference between a broadband continuum of states and a

Table 2.1: Simulation results for the particles in Figs. 2.4 and 2.3. Included are the constant refractive index n_0 , particle radius a , the size parameter $2\pi a\tilde{\nu}_r$, the Fano fit parameters σ_0 and q , along with the expansion errors for Q'_{exp} and Q'_Δ (Eq. 2.17 and 2.19). The percent errors are calculated as the maximum difference between the expansion and Q' , divided by the overall scale of Q' (e.g. $100\% \times \left\| \frac{\max[Q' - Q'_{\text{exp}}]}{\max[Q'] - \min[Q']} \right\|$)

Label	Simulated parameters			Fano fit parameters		Expansion errors (%)	
	n_0	a	$2\pi a\tilde{\nu}_r$	$\sigma_0(\times 10^{-3})$	q	Q'_{exp}	Q'_Δ
A	1.10	0.76	0.75	0.29	-20.7	3.5	3.5
B	1.10	1.53	1.57	2.75	-9.3	3.5	3.7
C	1.32	0.60	0.60	1.85	-7.2	3.8	4.0
D	1.32	2.00	2.01	63.76	-1.9	5.9	17.9
E	1.50	1.38	1.38	50.96	-1.8	5.0	19.4
F	1.50	2.00	2.01	135.51	-1.1	7.3	57.6

discrete absorption band, as it occurs in Fano theory. In the case of Mie scattering, the broadband continuum of states can be attributed to the dielectric interactions that produce the constant (in the mid-IR region) refractive index. This is evident from Eq. 2.19: as n_0 becomes large, the line shape gains its characteristic Fano-like asymmetry.

The goal to extract the pure absorbance from Fano line shapes arises from the desire to recover quantitative chemical understanding from observations. This is desirable, especially when conducting imaging experiments where spatially resolved chemistry can provide critical insight for the question at hand. For example, there are extensive infrared imaging efforts based on cancer diagnosis and evaluation [90–92]. The protein bands cannot be used for evaluation in these cases, since tissues at edges can lead to scattering signatures that can modify the peak frequency and absorption band line shape. However, proteins provide large signatures that could prove useful if they could be accurately recovered. Furthermore, extracting the bulk absorbance from the measured Fano profiles is imperative for 3-dimensional infrared imaging; standard tomographic reconstruction algorithms assume bulk absorption, i.e., the validity of Beer’s law, at a fundamental level [136].

2.4.1 Simulations

Based on our simulated data, we first compare the accuracy of the expansions Q'_{exp} and Q'_{Δ} . For weak absorption bands, Q'_{exp} should be accurate for arbitrary radii and refractive indices. Figure 2.3 (left) shows the accuracy of the expansion, and Table 2.1 verifies that the simulations are within 10% error. However, the small radii and refractive index expansion (Fig. 2.3, right) Q'_{Δ} clearly breaks down when the refractive index exceeds $n_0 \gtrsim 1.2$.

Next, results of fitting Fano line shapes to simulations are shown in Fig. 2.4. Particles with small radii a and constant refractive indices n_0 have a symmetric Lorentzian appearance whose peak is nearly centered on the resonance frequency $\tilde{\nu}_r$. Figure 2.4 (A) shows, for a small particle of radius $a = 0.76 \mu\text{m}$ and constant refractive index $n_0 = 1.1$, that the magnitude of q is relatively large in order to model the near Lorentzian symmetry. As the particle size doubles to $a = 1.5 \mu\text{m}$, Fig. 2.4 (B) displays how scattering effects begin to present ever so slightly, and the Fano q parameter decreases in magnitude to $q = -9.3$.

The effect of scattering becomes much more prominent as one increases the constant refractive index. Figures 2.4 (C) and (D) show the line shapes when the constant refractive index is increased to $n_0 = 1.3$. When increased even further to $n_0 = 1.5$, Fig. 2.4 (E) and (F) show that the line shapes begin to appear nearly anti-Lorentzian, and $q^2 \rightarrow 1$ as required to make the leading term in the Fano Eq. 2.20 zero.

2.4.2 Bulk-absorption Limit

As our primary motivation is to recover the pure absorbance in the bulk-absorption limit (Eq. 2.24), i.e., in the limit where no boundaries or interfaces are present, three quantities are necessary to reconstruct a Lorentzian line shape. These include the resonance position $\tilde{\nu}_r$, the pure absorbance strength A (see Eq. 2.24), and the width at half maximum $\Gamma_{\tilde{\nu}}$.

Recovery of $\tilde{\nu}_r$ is reliable to better than 0.2% for nearly all particles considered in our simulations. Figure 2.5 shows for select constant refractive indices n_0 that as the size parameter $2\pi a\tilde{\nu}_r$ and n_0 increase, the percent error in peak position of the spectrum containing

scatter climbs to as much as 1.5%. The parameters from the Fano fitting, however, reduce the error to under 0.1% for most cases.

While recovery of the Lorentzian width $\Gamma_{\tilde{\nu}}$ from the Fano fitting falls within 2% error for large $|q| > 6$ (i.e., when the peak is mostly Lorentzian), our algorithm experiences difficulty as the peak becomes more antisymmetric. This is seen in Fig. 2.8, where the error is scattered to as much as 6% when $|q| < 6$. It is unclear whether this error is due to the precision of our algorithm, or if there may be an inherent limitation on the ability to extract q and $\Gamma_{\tilde{\nu}}$ simultaneously.

Finally, an important result from the expansion of Q'_{Δ} (Eq. 2.19) is that simply removing the dispersive (anti-Lorentzian) component does not lead to the correct absorbance strength when Mie scattering occurs. Comparing the Lorentzian term in Q'_{Δ} (which is captured by the Fano parameters $\sigma_0(q^2 - 1)$ in Eq. 2.21) with the bulk absorbance in Eq. 2.24, the apparent absorbance is reduced (to second order in Δ) by an amount

$$\frac{128}{5}\pi^3 a^3 \Delta^2 \tilde{\nu}_r^2 f_0 \quad (2.30)$$

Figure 2.7 demonstrates an improvement of the pure absorbance strength compared to a Lorentzian construction that simply uses the height of the original asymmetric line shape. Such naïve reconstruction produces an error reaching over 95% as the size parameter $2\pi a \tilde{\nu}_r$ and constant refractive index increase. Using the corrective Eq. 2.25, the recovered absorbance strengths improve to under 10% for all simulated particles.

2.4.3 Connecting Fano Parameters With Radius and Refractive Index

Recovery of the constant refractive index n_0 given knowledge of the particle radius a is shown in Fig. 2.6, where dark markers signify calculations that fall within 1% of the exact value, and light markers signify calculations that fall outside 1% error.

The requirement that ρ_r is small in deriving the approximation Q'_Δ in Eq. 2.19 restricts the class of particles for which the analysis is valid to constant refractive indices $n_0 \lesssim 1.2$. However, while Fig. 2.6 shows that estimates of n_0 using Eq. 2.26 are most accurate for very small constant refractive indices, there is still reasonable accuracy for the larger refractive indices where many biological media fall (between 1.3 and 1.5 [137]).

These limitations are due in part to the expansion Q'_Δ (Eq. 2.19) which, because it assumes small ρ_r , does not hold as n_0 becomes significant. In particular, Eq. 2.21 and 2.22 are accurate to only $\mathcal{O}(\Delta^2)$. Future development could take into account higher orders of Δ when expanding Q'_{exp} , thus improving the accuracy of Eq. 2.21 and 2.22.

Finally, by fitting multiple Fano line shapes to overlapping spectra, our methods may be extended to more general cases where absorbance bands are not well-isolated, such as Amide-I bands, which typically have neighboring Amide-II and phospholipid bands in biological materials. While in principle Fano theory applies to isolated bands, overlapping bands may receive a similar treatment since the background process is the same for both resonances. Similarly, non-Lorentzian bandshapes, such as those due to many closely-packed resonances that cannot be resolved individually (e.g., the Amide-I peak, which often contains a mixture of many proteins), won't fit the Fano line-shape model exactly, but are still described by Fano theory. This is because we have shown that for weak resonances (as we noted are typical for biological media in the infrared), a first-order expansion of the imaginary component and its Kramers-Kronig transform are sufficiently accurate (see Fig. 2.3, Left). The problem is therefore linear, and non-isolated and non-Lorentzian bands can be treated as a sum of independent Fano processes.

2.5 Conclusions

We have shown that Fano line shapes in FTIR transmission and absorption spectra can occur due to Mie scattering, as the complex electromagnetic interference produces a spectrum that

includes contributions from both the real and imaginary components of the refractive index. As absorbance peaks are typically Lorentzian in nature, this superposition is equivalent to the Fano line shape for weakly scattering particles. Fano line shapes cause both a shift in peak frequency position, along with a change in absorbance strength.

While we have focused on spherical scatterers in this report, Fano line shapes are not restricted to this particular geometry. Any general first-order mixing of the real and imaginary refractive indices is equivalent to Fano line shapes for sufficiently weak Lorentzian absorbance bands. As scattering occurs due to a changing refractive index, we attribute the occurrence of Fano line shapes in the infrared regime to interference between sharp molecular vibration resonances with a background continuum process.

We also presented that, by fitting Fano line shapes to simulated spectra, in general, recovery of the peak shift can be found to within 0.1% in most cases when the peaks are isolated. Applying our fitting algorithm to spectra from small spherical scattering particles with various constant refractive indices, we demonstrated a link between the Fano fit parameters and the particle’s radius and constant refractive index. In particular, if one has a reasonable estimate of either the radius or constant refractive index, one may obtain the other quantity with reasonable accuracy. We also demonstrated that recovery of the bulk absorbance is possible for spherical particles.

In many cases a reasonable estimate of the particle size and refractive index will be known (e.g. by the manufacturer, or bright-field measurements), which would immediately inform whether one is working within the limitations presented in Sec. 2.4. However, the method presented may still be useful in cases where these values are either unavailable, or are outside the range of validity, where the full Mie theory is required. In this case, the task of fitting directly to the Mie model requires knowledge of the dielectric function, along with the material’s size and refractive index. As we discussed in Sec. 2.4.2, and illustrate in Fig. 2.4 (Left), the Fano line shape is a very accurate model for determining the Lorentzian parameters, without suffering from the limitations imposed on the size and refractive index.

The limitation on refractive index and particle radius occur due to the limited accuracy of the expansion when moving from Eq. 2.17 to Eq. 2.19. The method presented therefore allows one to rapidly extract the resonant position and width without resorting to a full implementation of the Mie equations. From there, if one wished, an iterative forward calculation using full Mie theory could be performed using the Lorentzian features that were extracted from the Fano method as a starting place. This would effectively reduce the search space from $(3N + 1)$ parameters to $(N+1)$, where N are the number of isolated Lorentzian peaks in the spectrum.

We also reemphasize that while it would be advantageous to simply fit directly to Eqs. 2.17 and 2.19 to obtain the full set of parameters, this is not possible since these equations deceptively contain only four independent parameters (see Appendix 2.6). Since the Fano formalism also contains four parameters, there is no loss of information when using this model.

Finally, we stress that an experimental evaluation of our methods is very challenging, as it requires manufacturing an experiment where an isolated homogeneous sphere containing an isolated absorption band is embedded in an infinite, non-absorbing homogeneous medium whose refractive index is closely matched with that of the sphere's. However, if the effects of a finite medium are forgivable, experiments where micro-spheres are embedded in a non-absorbing medium (e.g. potassium bromide) would be a natural starting point. Unfortunately, however, for many standard micro-spheres (e.g., polystyrene, silica, or PMMA), the requirement of well-isolated absorbance bands remains difficult to satisfy. Therefore, the next logical step is to generalize the methods presented to the more realistic situation of overlapping absorbance bands. As such a generalization will necessarily deviate from the strict Fano model, those situations fall outside the scope of this article, where emphasis on the Fano mechanism will be reduced.

Although standard methods exist for correction of entire spectral regions [17, 19, 128], we believe that understanding scattering phenomena for small spheres with isolated resonances

in terms of Fano theory may set the stage for corrective methods that may generalize to more complicated spectra, and possibly to arbitrary morphology.

2.6 Appendix

When a plane electromagnetic wave (whose wave number $\tilde{\nu}$) interacts with a dielectric sphere of complex refractive index $\tilde{\eta} = n_r(\tilde{\nu}) + in_i(\tilde{\nu})$ and radius a , the coherent interference between the incident and scattered waves results in an extinction Q_{ext} at a detector in the far field, approximated by van de Hulst [15] as

$$\begin{aligned} Q_{ext}(\tilde{\nu}) = & 2 - 4 \exp \{ -\rho \tan \beta \} \left(\frac{\cos \beta}{\rho} \right) \sin (\rho - \beta) \\ & - 4 \exp \{ -\rho \tan \beta \} \left(\frac{\cos \beta}{\rho} \right)^2 \cos (\rho - 2\beta) \\ & + 4 \left(\frac{\cos \beta}{\rho} \right)^2 \cos 2\beta \end{aligned} \quad (2.31)$$

where

$$\rho(\tilde{\nu}) = 4\pi a \tilde{\nu} (n_r(\tilde{\nu}) - 1) \quad (2.32)$$

$$\tan \beta = \frac{n_i(\tilde{\nu})}{n_r(\tilde{\nu}) - 1} \quad (2.33)$$

The imaginary part of the refractive index, $n_i(\tilde{\nu})$, is a dimensionless quantity inherent to the medium, and is related to the real component of the refractive index, $n_r(\tilde{\nu})$, through the Kramers-Kronig transformation

$$n_r(\tilde{\nu}) - n_0 = \frac{2}{\pi} P \int_0^\infty \frac{\Omega n_i(\Omega)}{\Omega^2 - \tilde{\nu}^2} d\Omega \quad (2.34)$$

$$n_i(\tilde{\nu}) = -\frac{2\tilde{\nu}}{\pi} P \int_0^\infty \frac{n_r(\Omega)}{\Omega^2 - \tilde{\nu}^2} d\Omega \quad (2.35)$$

Here, $n_0 \geq 1$ is assumed constant (in the mid-infrared region), and P denotes the Cauchy principal value required because of the singularity in the integrand (see, e.g., [20, 138]). It is also assumed that the refractive index surrounding the spherical medium is air, approximately equal to unity.

Concealed in Q_{ext} (Eq. 2.31) is an oscillating “background” spectrum where resonating features are superimposed. Away from resonances (that is, where $n_i(\tilde{\nu}) \rightarrow 0$), this background Q_{BG} appears as

$$Q_{BG} = 2 - \frac{4}{\rho_0} \sin \rho_0 + \frac{4}{\rho_0^2} (1 - \cos \rho_0) \quad (2.36)$$

where here

$$\rho_0 = 4\pi a \tilde{\nu} (n_0 - 1) \quad (2.37)$$

Band resonances in FTIR spectra typically [2] (p.23) take the shape of a Lorentzian L , centered on the resonance position $\tilde{\nu}_r$ as

$$L = \frac{f_0}{1 + z^2} \quad (2.38)$$

where the reduced spectral dimension $z = (\tilde{\nu} - \tilde{\nu}_r)/\frac{\Gamma_{\tilde{\nu}}}{2}$ is defined for the peak width at half maximum $\Gamma_{\tilde{\nu}}$. While technically the dielectric function $\tilde{\epsilon}$ follows the Lorentzian model, the complex refractive index $\tilde{\eta}$ is related to the complex dielectric function (for a non-magnetic material) as

$$\tilde{\eta} = \sqrt{\tilde{\epsilon}} \quad (2.39)$$

and for small peaks it is sufficient to approximate the refractive index to be composed of

Lorentzian line shapes

$$\tilde{\eta} \approx (n_0 - zL) + iL \quad (2.40)$$

We therefore write $n_i(\tilde{\nu})$ as a Lorentzian of height f_0 , and its Kramers-Kronig transform $n_r - n_0 = K[n_i(\nu)]$ as

$$n_i(\tilde{\nu}) = \frac{f_0}{1 + z^2} \quad \text{and} \quad n_r(\tilde{\nu}) - n_0 = \frac{zf_0}{1 + z^2} \quad (2.41)$$

Denote by $Q' \equiv Q_{ext} - Q_{BG}$ the removal of the background Q_{BG} from Q_{ext} , revealing the “interesting” spectral features (see Fig. 2.2). We then consider the behavior of Q' for a Lorentzian line shape $n_i(\tilde{\nu}) = f_0/(1 + z^2)$.

An expansion that assumes small f_0 is first performed on Q' , following a local expansion about z . However, it will first prove useful to rewrite Eq. 2.32 and 2.33 for ρ and β as

$$n_r(\tilde{\nu}) - 1 = \Delta + K[n_i(\tilde{\nu})] \quad (2.42)$$

where $\Delta \equiv n_0 - 1$, and $K[n_i(\tilde{\nu})]$ is the Kramers-Kronig transform of n_i as defined on the right-hand side of Eq. 2.34. Indeed n_i and $K[n_i]$ are typically very small, and Δ is typically less than 0.5 in the infrared region for dilute biological media [16, 132, 139]. In such cases, expanding Q' (using the computer algebra system SageMath [140]) to linear order in f_0 , followed by a first-order expansion of the numerator gives

$$Q' \approx \frac{8f_0\tilde{\nu}_r^2(\Psi_1 + \Psi_2z)}{\rho_r^2\Delta\left(\frac{\Gamma_{\tilde{\nu}}}{2}z + \tilde{\nu}_r\right)^2(1 + z^2)} \quad (2.43)$$

where

$$\Psi_1 = \rho_r \cos(\rho_r) + \left(\frac{\rho_r^2}{2} - 1\right) \sin(\rho_r) \quad (2.44)$$

$$\Psi_2 = -\left[\rho_r \sin(\rho_r) - 1 - \left(\frac{\Gamma_{\tilde{\nu}}/2}{2\tilde{\nu}_r} \rho_r^3 + \frac{\rho_r^2}{2} - 1\right) \cos(\rho_r)\right] \quad (2.45)$$

Assuming that $\tilde{\nu}_r \gg \Gamma_{\tilde{\nu}}$, the factor $(\frac{\Gamma_{\tilde{\nu}}}{2}z + \tilde{\nu}_r)^{-2}$ in Eq. 2.43 approximates to $(1 - \frac{\Gamma_{\tilde{\nu}}}{4\tilde{\nu}_r}z)/\tilde{\nu}_r^2$, and the extinction is approximated as

$$Q'_{\text{exp}}(\tilde{\nu}) \equiv \frac{8f_0(\Phi_1 + \Phi_2 z)}{\rho_r^2 \Delta(1 + z^2)} \quad (2.46)$$

where Φ_1 and Φ_2 are related to Ψ_1 and Ψ_2 by

$$\Phi_1 = \Psi_1 \quad (2.47)$$

$$\Phi_2 = \Psi_2 - \frac{\Gamma_{\tilde{\nu}}}{4\tilde{\nu}_r} \Psi_1 \quad (2.48)$$

The numerator was expanded to linear order so that Q'_{exp} has the expected boundary conditions (i.e., $Q' \rightarrow 0$ as $\tilde{\nu} \rightarrow \pm\infty$). Note also that the same expression for Q'_{exp} may be derived by assuming a solution of the form $\phi(z) = (\phi_1 + \phi_2 z)/(1 + z^2)$ and equating coefficients of a linear expansion in both ϕ and Q' .

An additionally useful result is the difference in Q'_{exp} at its maximum and minimum values $\tilde{\nu}_{\text{max}}$ and $\tilde{\nu}_{\text{min}}$. Using SageMath [140], an expression for this difference is obtained and expanded to second order in Δ , giving

$$Q'_{\text{exp}}(\tilde{\nu}_{\text{max}}) - Q'_{\text{exp}}(\tilde{\nu}_{\text{min}}) \approx \frac{f_0 \left(\begin{aligned} &160(\Gamma^4 + 2\Gamma^2\tilde{\nu}_r^2 + \tilde{\nu}_r^4)\rho_r \\ &- 120(\Gamma^3\tilde{\nu}_r + \Gamma\tilde{\nu}_r^3)\rho_r^2 \\ &- 3(48\Gamma^4 + 64\Gamma^2\tilde{\nu}_r^2 + \tilde{\nu}_r^4)\rho_r^3 \end{aligned} \right)}{120\Delta\tilde{\nu}_r(\Gamma^2 + \tilde{\nu}_r^2)\sqrt{\Gamma^2 + \tilde{\nu}_r^2}} \quad (2.49)$$

Assuming again that $\tilde{\nu}_r \gg \Gamma_{\tilde{\nu}}$, Eq. 2.49 is approximated to $\mathcal{O}(\frac{\Gamma_{\tilde{\nu}}}{2\tilde{\nu}_r})$ as

$$Q'_{\text{exp}}(\tilde{\nu}_{\text{max}}) - Q'_{\text{exp}}(\tilde{\nu}_{\text{min}}) \approx \frac{f_0}{\Delta} \left(\frac{4\rho_r}{3} - \frac{\frac{\Gamma_{\tilde{\nu}}}{2}\rho_r^2}{\tilde{\nu}_r} - \frac{\rho_r^3}{40} \right) \quad (2.50)$$

It is noted that while Eq. 2.50 contains five parameters (f_0 , $\tilde{\nu}_r$, $\Gamma_{\tilde{\nu}}$, a , and Δ), only four are independent. Observe that only terms containing the product of radius a and relative refractive index Δ appear in ρ_r , while f_0 and Δ only ever occur in both terms as the ratio f_0/Δ .

Finally, investigating Q'_{exp} for small, optically soft particles, a further expansion of Eq. 2.46 to second order in Δ gives

$$\begin{aligned} Q'_{\Delta}(\tilde{\nu}) \equiv & \left(\frac{4\rho_r}{3} - \frac{2\rho_r^3}{5} \right) \left(\frac{f_0/\Delta}{1+z^2} \right) \\ & + \left(\frac{4\rho_r \frac{\Gamma_{\tilde{\nu}}}{2}}{\tilde{\nu}_r} - \rho_r^2 - \frac{2\rho_r^3 \frac{\Gamma_{\tilde{\nu}}}{2}}{5\tilde{\nu}_r} \right) \left(\frac{f_0 z/\Delta}{1+z^2} \right). \end{aligned} \quad (2.51)$$

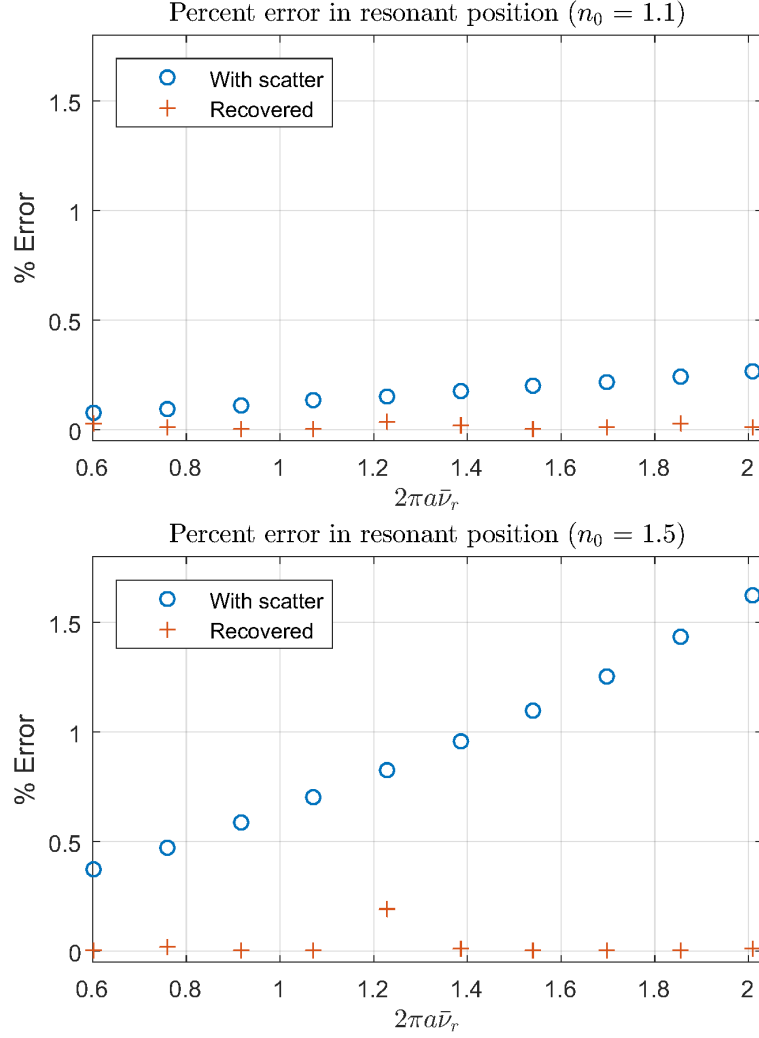


Figure 2.5: Recovered resonant position $\tilde{\nu}_r$ for select refractive indices n_0 as a function of size parameter $2\pi a\tilde{\nu}_r$. Shown are the error in position estimates that would be predicted from the simulated transmission spectrum (with scatter), and the recovered positions. As the constant refractive index n_0 increases, the peak position can be shifted by as much as 1.6%, but we are able to recover the true positions $\tilde{\nu}_r$ to within 0.2% or better.

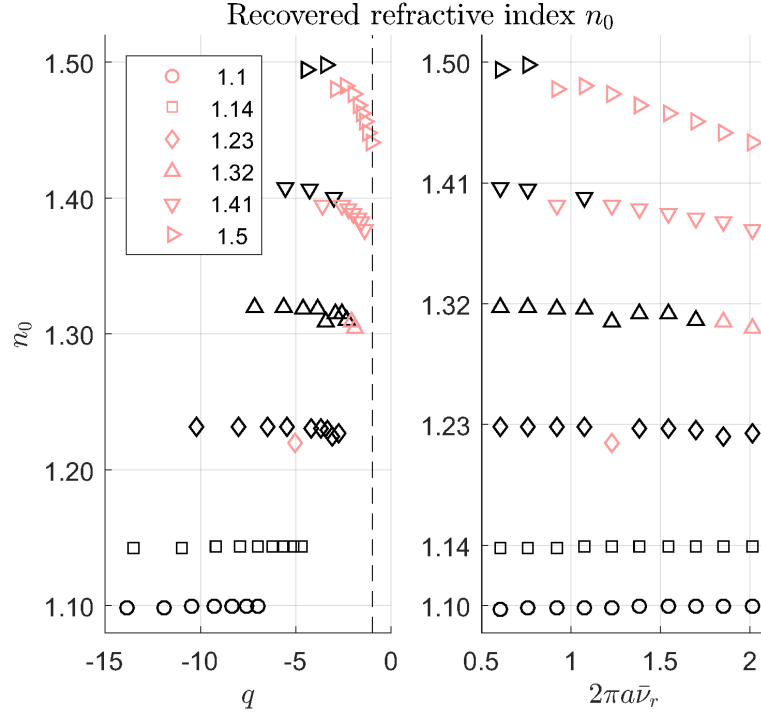


Figure 2.6: How refractive indices calculated from Fano fitting compare to exact values. **Legend:** Actual constant refractive indices n_0 for various sphere sizes. Dark markers indicate calculations that fall within 1% of the exact value. **Vertical axis:** Calculated n_0 with knowledge of the particle's size, using Eq. 2.26. **Left:** Calculated n_0 vs Fano fit parameter q . Dashed line at $q = -1$ are anti-Lorentzian line shapes, while large q approach pure Lorentzians. **Right:** Calculated n_0 vs size parameter $2\pi a \tilde{\nu}_r$ for radius a and resonating band $\tilde{\nu}_r$.

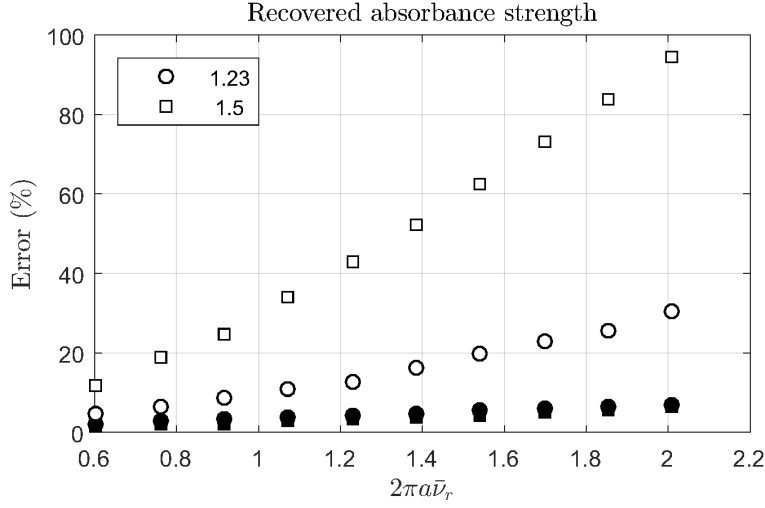


Figure 2.7: Error in absorbance strengths as a function of size parameter $2\pi a \tilde{\nu}_r$ for various constant refractive indices n_0 (see legend). Solid markers are recovered absorbance strength errors (using Eq. 2.25), while hollow markers are the error if one were to simply remove the anti-Lorentzian contribution (using Eq. 2.29 from Fano fit parameters). All calculations fall under 10% for each of the particles in our simulations.

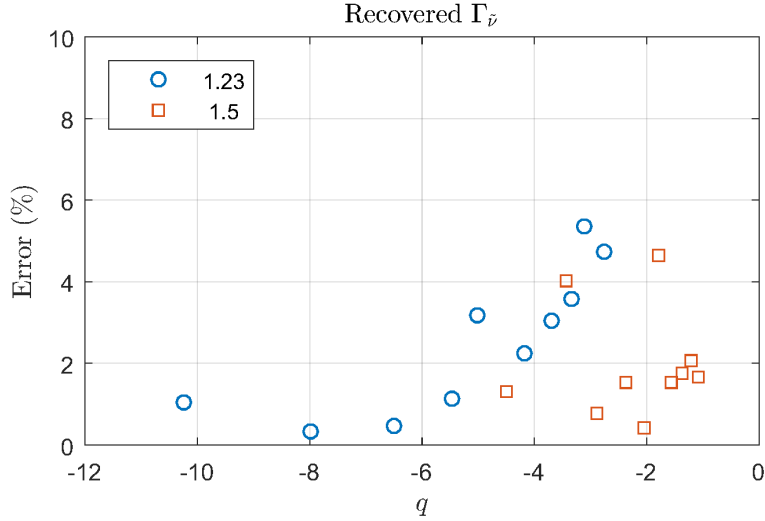


Figure 2.8: Recovered full width at half maxima $\Gamma_{\tilde{\nu}}$ from fitted Fano line shapes have an error that appear to depend mostly on the fit parameter q . When $|q| > 6$ the line shape is mostly Lorentzian and the error in determining peak width is nearly under 2%. However, when $|q| < 6$ the line shape loses symmetry and the error climbs to nearly 6%.

Chapter 3

Spherical Scattering Part II: Multiple Peaks and the Generalized Fano Effect

Previously, it has been shown that observed derivative-like features of absorbance bands in mid-infrared spectra of scattering spheres may be modeled as Fano resonances in certain cases [28]. An inherent limitation, however, is the restriction to isolated absorbance bands. Here, we generalize the results obtained from Fano modeling to multiple, overlapping absorbance bands, under the same conditions previously assumed [28]. Presented is an algorithm for modeling Mie spectra of scattering spheres, with a demonstration on simulated spectra, along with an experimental application on a measurement of polystyrene microspheres embedded in a potassium-bromide medium.

3.1 Introduction

Scattering effects often occur in infrared spectroscopy, where deviations from the idealized Beer-Lambert absorption limit produces notable spectral features such as fringing [8, 141], baseline effects [17, 18], and even band distortions [2, 17, 28, 128]. Particularly, it has been shown that for spherical scatterers, derivative-like bandshape distortions may be modeled by Mie theory, where the observed spectra are described as a non-linear mixing between the

absorbance and dispersive spectra on top of a smooth-varying broadband baseline [16, 17, 19, 128].

For soft matter where absorption bands are relatively weak (as is often the case for many materials and biological media in the infrared [16, 132, 139]), it is possible to linearize this mixing process—which, for the case of an isolated absorbance band, results in simple Fano line shapes whose parameters may be modeled and equated to properties of the scatterer [28].

3.2 Methods

While an exact solution to the extinction efficiency¹ of a scattering sphere is solvable with Mie theory [10], the solution is non-linear and unnecessarily complex for many of the cases encountered in FTIR imaging of biological samples. Fortunately, the van de Hulst approximation has validity in cases where small, optically soft spheres are measured. The extinction efficiency Q approximated by van de Hulst is given by [15]

$$\begin{aligned} Q_{\text{ext}}(\tilde{\nu}) = & 2 - 4 \exp \{ -\rho \tan \beta \} \left(\frac{\cos \beta}{\rho} \right) \sin (\rho - \beta) \\ & - 4 \exp \{ -\rho \tan \beta \} \left(\frac{\cos \beta}{\rho} \right)^2 \cos (\rho - 2\beta) \\ & + 4 \left(\frac{\cos \beta}{\rho} \right)^2 \cos 2\beta \end{aligned} \quad (3.1)$$

where

$$\rho(\tilde{\nu}) = 4\pi a \tilde{\nu} (n_r(\tilde{\nu}) - 1) \quad (3.2)$$

$$\tan \beta = \frac{n_i(\tilde{\nu})}{n_r(\tilde{\nu}) - 1} \quad (3.3)$$

¹In the geometric-optics limit and for a wide enough detector aperture, the extinction efficiency Q_{ext} is related to the transmittance $T = I/I_0$ via $T = 1 - (g/G)Q_{\text{ext}}$, where $g = \pi a^2$ is the geometric cross section of the sphere, a is the radius of the sphere, and G is the detector aperture (see [10, 20] for details).

and n_r and n_i are the real and imaginary components of the relative refractive index $n(\tilde{\nu})/n_m = n_r - in_i(\tilde{\nu})$. It is assumed hereafter that the sphere has a spectrally-dependent complex refractive index $n(\tilde{\nu})$, while its surrounding medium n_m is real (i.e, non-absorbing) and spectrally constant.

Although the van de Hulst formulation is clearly still a non-linear function of both the complex refractive index and sphere size, we showed previously that certain linearities could be extracted from this model, equating to Fano line shapes in situations where isolated absorbance bands exist [28]. In particular, we showed that when absorbance bands are weak and Lorentzian, a local expansion about its resonance position produces a linear combination of a Lorentzian and anti-Lorentzian (i.e., the Kramer's-Kronig transform of the Lorentzian) component. This superposition, or degree of mixing, is controlled by physical properties including its size and real refractive index.

When dealing with multiple, overlapping bands, however, this approach is complicated by the fact that any particular band will see a non-constant real refractive index due to fluctuations from neighboring bands. Therefore, a different approach is necessary.

A simple way to generalize to multiple peaks is, instead of a local expansion about a single band, expand about the more general imaginary refractive index. Assuming the real refractive index can be written as the sum of a constant n_0 and fluctuating component $\hat{n}_i(\tilde{\nu})$ (where $\hat{n}_i(\tilde{\nu}) = -K[n_i(\tilde{\nu})]$ is the negative Kramer's-Kronig transform [10, 28, 138]),

$$n_r(\tilde{\nu}) = n_0 + \hat{n}_i(\tilde{\nu}), \quad (3.4)$$

define the following parameters

$$\begin{aligned} \Delta &= n_0 - 1 \\ \gamma &\equiv 4\pi a \Delta \\ \rho_0 &= \gamma \tilde{\nu} \end{aligned} \quad (3.5)$$

Performing a second-order expansion about ρ gives [15]

$$Q_{\text{ext}} \approx \frac{4}{3}\rho \tan \beta + \frac{1}{2}\rho^2 (1 - \tan^2 \beta) \quad (3.6)$$

For very weak absorption bands (often seen in biological media [28]), a linear expansion about $n_i(\tilde{\nu})$ and $\hat{n}_i(\tilde{\nu})$ gives

$$Q_1(\tilde{\nu}) \equiv \frac{4}{3} \frac{\gamma \tilde{\nu}}{\Delta} n_i(\tilde{\nu}) - \frac{\gamma^2 \tilde{\nu}^2}{\Delta} \hat{n}_i(\tilde{\nu}) + \frac{1}{2} \gamma^2 \tilde{\nu}^2 \quad (3.7)$$

This model says that the extinction spectrum is a (wavelength-dependent) linear superposition of the imaginary refractive index and its Kramer's-Kronig transform. For stronger bands that may be observed in certain inorganic media (e.g., plastics and silica), these can be taken to second order

$$Q_2(\tilde{\nu}) \equiv Q_1(\tilde{\nu}) + \frac{\gamma^2 \tilde{\nu}^2}{2\Delta^2} (\hat{n}_i^2(\tilde{\nu}) - n_i^2(\tilde{\nu})) \quad (3.8)$$

From a theoretical perspective, the approximations presented in Eqs. 3.7 and 3.8 (which are valid for weakly scattering and absorbing spheres) are the desired models upon which to proceed with multi-peak modeling. There remains, however, the task of applying these theoretical models to practical measurements of a sample's transmission spectrum.

In a practical FTIR measurement, one measures two intensity spectra: the sample emission spectrum $I(\tilde{\nu})$, and a reference (or background) $I_0(\tilde{\nu})$. The ideal relation between Q_{ext} and the transmission $T = I/I_0$ is, in the geometric-optics limit and for a wide enough aperture

$$Z(\tilde{\nu}) \equiv \frac{g}{G} Q_{\text{ext}}(\tilde{\nu}) = 1 - T(\tilde{\nu}), \quad (3.9)$$

where $Z(\tilde{\nu})$ is defined as the extinction efficiency scaled by the ratio of the sphere's geo-

metrical cross section $g = \pi a^2$ to the detector aperture area G [10, 142]. To account for practical effects such as measurement optics and imperfect reference spectra, this relationship is extended to include an arbitrary scaling² σ_0 and a constant offset c_0 . Thus, the approximated extinction models in Eqs. 3.7 and 3.8 are used to model a measured spectrum $A(\tilde{\nu}) = 1 - T(\tilde{\nu})$ as

$$Z_n(\tilde{\nu}) = \sigma_0 Q_n(\tilde{\nu}) + c_0 \quad (3.10)$$

where $n = 1$ or 2 , specifying the desired order³ (Eqs. 3.7 or 3.8, respectively). For the linear case ($n = 1$), this model is given explicitly using Q_1 in Eq. 3.7

$$Z_1 = \sigma_0 \left\{ \frac{4}{3} \frac{\gamma \tilde{\nu}}{\Delta} n_i(\tilde{\nu}) - \frac{\gamma^2 \tilde{\nu}^2}{\Delta} \hat{n}_i(\tilde{\nu}) + \frac{1}{2} \gamma^2 \tilde{\nu}^2 \right\} + c_0 \quad (3.11)$$

It is straightforward to obtain a similar expression for the second-order model Z_2 , using Eq. 3.8.

3.2.1 Multi-peak Modeling

Our goal is to model a measured spectrum $A(\tilde{\nu}) = 1 - T(\tilde{\nu})$ that contains multiple, weakly absorbing bands, using the model $Z_n(\tilde{\nu})$ in Eq. 3.10, with the purpose of extracting γ and the imaginary refractive index (scaled by $1/\Delta$). If one has a suitable a priori reference of the imaginary refractive index (e.g., standard materials, or from a thin film measurement), the modeling process amounts to simple least squares fitting (see Sec. 3.4).

However, if one is not equipped with such a reference spectrum (or simply want to refine an estimated reference), the bands may be modeled directly. This requires, however, some

²The parameter σ_0 is very similar to the scaling parameter used previously by the authors in Fano modeling [28]. In this current work, however, it is given explicit meaning as the overall scaling of the ideal extinction, due to the measurement conditions (such as the optics). This is in contrast to its previous definition, where σ_0 was a catch-all that also included the band's strength.

³The subscript n specifies the expansion order, and should not be confused with the refractive index $n(\tilde{\nu})$, which will never appear as a subscript.

further assumptions regarding the structure of $n_i(\tilde{\nu})$ (and hence, $\hat{n}_i(\tilde{\nu})$).

Since FTIR is often concerned with (relatively weak) molecular vibrational interactions[2], it is assumed that the imaginary refractive index approximately follows the Lorentzian model, composed as a collection of J Lorentzian oscillators. Therefore, the fluctuating components of the refractive index are modeled as

$$\begin{aligned} n_i(\tilde{\nu}) &= \sum_{j=1}^J \frac{\alpha_j}{1 + z_j^2} \\ \hat{n}_i(\tilde{\nu}) &= \sum_{j=1}^J \frac{\alpha_j z_j}{1 + z_j^2} \end{aligned} \tag{3.12}$$

where $z_j = (\tilde{\nu} - \tilde{\nu}_{0,j})/\frac{\Gamma_j}{2}$ is the reduced spectral coordinate for the j^{th} band of strength α_j centered at resonance position $\tilde{\nu}_{0,j}$, and whose half-width-at-half-maximum is $\Gamma_j/2$.

For the $n = 1$ expansion model Z_1 , Eq. 3.11 is linear in the functions $1/(1 + z_j^2)$ and $z_j/(1 + z_j^2)$, whereas cross-terms enter for the second-order model Z_2 . A multi-peak modeling approach for the linear case is developed first; the second order model will use these results in an iterative updating process.

Linear Case

It is first assumed that a collection of J resonances (positions $\tilde{\nu}_{0,j}$ and widths Γ_j) are approximately known. Since the scattering is assumed weak, this means that chemical bands should be distinct from scattering features such as fringes [8, 141], ripples or wiggles [10]; band positions and their widths may therefore be estimated directly from the measured spectrum $A(\tilde{\nu})$. (The possibility of isolating bands from certain scattering features is discussed in Sec. 3.4.)

Inserting the multi-peak refractive index model from Eqs. 3.12 into the linear model

Eq. 3.11 gives

$$Z_1(\tilde{\nu}) = \sigma_0 \sum_{j=1}^J \left\{ \frac{4\gamma\tilde{\nu}}{3} \left(\frac{\alpha_j/\Delta}{1+z_j^2} \right) - \gamma^2\tilde{\nu}^2 \left(\frac{z_j\alpha_j/\Delta}{1+z_j^2} \right) \right\} + \frac{\sigma_0\gamma^2\tilde{\nu}^2}{2} + c_0 \quad (3.13)$$

Although fitting this model to a measured spectrum $A(\tilde{\nu})$ allows determination of the parameters σ_0 and γ , each of the α_j are inseparable from Δ , without additional knowledge. This is because the two only ever appear as the ratio α_j/Δ . These parameters are therefore replaced by a single parameter

$$\beta_j \equiv \frac{\alpha_j}{\Delta} \quad (3.14)$$

There are a number of approaches that may be used to fit these model parameters. We will proceed with an iterative algorithm consisting of three primary solving steps. These steps include two Least squares fitting that solve for the parameters σ_0 , γ , and β_j , followed by a gradient descent routine that optimizes the parameters $\tilde{\nu}_{0,j}$ and Γ_j .

To prepare for least squares fitting, the model Z_1 is rewritten in terms of the coefficients c_1 , c_2 , c_4 and c_0 (note: the jump in subscript indexing is intentional)

$$Z_1(\tilde{\nu}) = \sum_{j=1}^J \left\{ \frac{4c_1\tilde{\nu}}{3} \left(\frac{\beta_j}{1+z_j^2} \right) - c_2\tilde{\nu}^2 \left(\frac{\beta_j z_j}{1+z_j^2} \right) \right\} + \frac{c_4\tilde{\nu}^2}{2} + c_0 \quad (3.15)$$

Before proceeding, the coefficients c_1 and c_2 are initialized with the values $c_1^{(0)}$ and $c_2^{(0)}$, respectively (choices for these initialization values are discussed in Sec. 3.4).

In the first step, the coefficients c_1 , c_2 , and parameters $\tilde{\nu}_{0,j}$, and Γ_j are used from the previous iteration (or from its initialization values on the first iteration), and the β_j are solved from a least squares error minimization. Let the measured transmission spectrum \mathbf{A}

be a column vector whose elements $A_k = A(\tilde{\nu}_k) = 1 - T(\tilde{\nu}_k)$ are the K samples at discrete wavenumbers $\tilde{\nu}_k$

$$\mathbf{A}(\tilde{\nu}) = \begin{bmatrix} A_1 & A_2 & \dots & A_K \end{bmatrix}^T, \quad (3.16)$$

where $k = 1, 2, \dots, K$. The task is to minimize the error $\boldsymbol{\epsilon}$ in the matrix equation

$$\mathbf{A} = \mathbf{M}\boldsymbol{\beta} + \boldsymbol{\epsilon} \quad (3.17)$$

where \mathbf{M} is a $K \times (J + 2)$ matrix formed from the modeling terms in $Z_1(\tilde{\nu})$, and $\boldsymbol{\beta}$ is the vector of oscillator strengths β_j and baseline coefficients c_4 and c_0

$$\boldsymbol{\beta} = \begin{bmatrix} \beta_1 & \beta_2 & \dots & \beta_k & c_4 & c_0 \end{bmatrix}^T, \quad (3.18)$$

The first J columns of \mathbf{M} are given by

$$\mathbf{M}_{kj} = \frac{4c_1\tilde{\nu}_k}{3}L_{k,j} - c_2\tilde{\nu}_k^2\hat{L}_{k,j} \quad (3.19)$$

where

$$\begin{aligned} L_{k,j} &= \frac{1}{1 + \left(\frac{\tilde{\nu}_k - \tilde{\nu}_{0,j}}{\Gamma_j/2}\right)^2} \\ \hat{L}_{k,j} &= \left(\frac{\tilde{\nu}_k - \tilde{\nu}_{0,j}}{\Gamma_j/2}\right) L_{k,j} \end{aligned} \quad (3.20)$$

The remaining two columns of \mathbf{M} are given by the baseline terms from the model $Z_1(\tilde{\nu})$

$$\mathbf{M}_{k,J+1} = \tilde{\nu}_k^2/2 \quad (3.21)$$

$$\mathbf{M}_{k,J+2} = 1 \quad (3.22)$$

Then, the vector $\boldsymbol{\beta}$ is then solved from the least squares solution

$$\boldsymbol{\beta} = (\mathbf{M}^T \mathbf{M})^{-1} \mathbf{M}^T \mathbf{A} \quad (3.23)$$

Finally, a tentative analytic refractive index column vector $\tilde{\mathbf{m}}$ is constructed from this solution, whose elements $\tilde{\mathbf{m}}_k$ contain real and imaginary components given by

$$\tilde{\mathbf{m}}_k = \sum_{j=1}^J \beta_j \left(\hat{L}_{k,j} + i L_{k,j} \right) \quad (3.24)$$

The second step is to use this tentative analytic refractive index $\tilde{\mathbf{m}}$ to refine the coefficients c_1 and c_2 . This is achieved with a second least-squares minimization of the error $\boldsymbol{\epsilon}$ in the matrix equation

$$\mathbf{A} = \mathbf{N} \mathbf{x} + \boldsymbol{\epsilon} \quad (3.25)$$

where here \mathbf{N} is a $K \times 4$ matrix, and \mathbf{x} is the vector of coefficients

$$\mathbf{x} = \begin{bmatrix} c_1 & c_2 & c_4 & c_0 \end{bmatrix}^T \quad (3.26)$$

Here, \mathbf{N} is given by

$$\mathbf{N} = \begin{bmatrix} \frac{4}{3} \tilde{\boldsymbol{\nu}} \odot \Im \tilde{\mathbf{m}} & -\tilde{\boldsymbol{\nu}}^2 \odot \Re \tilde{\mathbf{m}} & \frac{1}{2} \tilde{\boldsymbol{\nu}}^2 & 1 \end{bmatrix} \quad (3.27)$$

where the notation \odot signifies the Hadamard product (i.e., vectors are multiplied element-wise), and the (K -element) column wavenumber vectors are defined as

$$\begin{aligned} \tilde{\boldsymbol{\nu}} &\equiv \begin{bmatrix} \tilde{\nu}_1 & \tilde{\nu}_2 & \dots & \tilde{\nu}_K \end{bmatrix}^T \\ \tilde{\boldsymbol{\nu}}^2 &\equiv \begin{bmatrix} \tilde{\nu}_1^2 & \tilde{\nu}_2^2 & \dots & \tilde{\nu}_K^2 \end{bmatrix}^T \end{aligned} \quad (3.28)$$

As in the first step, the vector \mathbf{x} of coefficients are solved from the least squares solution

$$\mathbf{x} = (\mathbf{N}^T \mathbf{N})^{-1} \mathbf{N}^T \mathbf{A} \quad (3.29)$$

The coefficient values c_1 , c_2 , and c_4 , obtained from the solution \mathbf{x} , allow immediate retrieval of σ_0 and γ by

$$\gamma = c_2/c_1 \quad (3.30)$$

$$\sigma_0 = c_4 (c_1/c_2)^2 \quad (3.31)$$

Finally, since the two least squares steps do not guarantee that the coefficients c_1 , c_2 and β_j have the correct scaling, they are adjusted using the constraints in Eqs. 3.30 and 3.31. In particular, if the coefficients c_1 and c_2 are incorrectly scaled by the factor f , then β_j will be scaled by $1/f$. To illustrate, let c'_1 , c'_2 , and β'_j be the desired (correctly scaled) solutions. Then, the (incorrectly scaled) solutions c_1 , c_2 , and β_j returned by the two least squares fits have been scaled as

$$\begin{aligned} c_1 &= c'_1 f \\ c_2 &= c'_2 f \end{aligned} \quad (3.32)$$

$$\beta_j = \beta'_j / f$$

The factor f is calculated from the coefficients

$$f = c_2/c_4 \quad (3.33)$$

and the adjusted coefficients c'_1 , c'_2 , and analytical refractive index $\tilde{\mathbf{m}}'$ are therefore given by

$$\begin{aligned} c'_1 &= c_1 (c_4/c_2) \\ c'_2 &= c_4 \end{aligned} \quad (3.34)$$

$$\tilde{\mathbf{m}}' = (c_2/c_4) \tilde{\mathbf{m}}$$

As a third, and final step, gradient descent is performed, optimizing $\tilde{\nu}_j$ and Γ_j , while using the updated parameters in Eqs. 3.34. A brief discussion on this approach is given in Sec. 3.4.

The entire three-step procedure is outlined more concisely in the following algorithm:

Algorithm 1. Given a collection of J resonances, with estimated positions $\tilde{\nu}_{0,j}$ and half-widths-at-half-maxima $\Gamma_j/2$, our proposed method for fitting Eq. 3.11 to a measured spectrum $A(\tilde{\nu})$ is as follows:

1. Initialize coefficients

$$\begin{aligned} c_1 &= c_1^{(0)} \\ c_2 &= c_2^{(0)} \end{aligned}$$

2. Form the matrix \mathbf{M} using previous values of c_1 , c_2 , $\tilde{\nu}_{0,j}$ and Γ_j
3. Compute $\boldsymbol{\beta}$ from the least-squares equation

$$\boldsymbol{\beta} = (\mathbf{M}^T \mathbf{M})^{-1} \mathbf{M}^T \mathbf{A}$$

4. Using the values obtained in (3), form the tentative analytic refractive index vector $\tilde{\mathbf{m}}$ whose K elements are each given by

$$\tilde{\mathbf{m}}_k = \sum_{j=1}^J \beta_j \left(\hat{L}_{k,j} + iL_{k,j} \right)$$

5. Form the matrix \mathbf{N} using the complex refractive index obtained in (4)
6. Compute \mathbf{x} from the least-squares equation

$$\mathbf{x} = (\mathbf{N}^T \mathbf{N})^{-1} \mathbf{N}^T \mathbf{A}$$

7. Adjust coefficients and analytic refractive index using Eq. 3.34
8. Fine-tune resonant positions $\tilde{\nu}_j$ and half-widths-at-half-maxima $\Gamma_j/2$ by gradient descent (which may have its own stopping criteria)
9. Repeat steps (2) through (8) using updated values, until either a desired number of iterations have been performed, or the residual error $|\epsilon|^2 = \epsilon^T \epsilon$ is below a desired threshold

Second-order Case

Extending the linear algorithm to the second order Mie model Z_2 requires very few modifications. The approach we take is to use the modeled analytic refractive index $\tilde{\mathbf{m}}$ calculated from the previous iteration for each of the second-order components. The model Z_2 is rewritten in terms of the coefficients c_1 , c_2 , c_3 , and c_4

$$\begin{aligned}
Z_2(\tilde{\nu}) = \sum_{j=1}^J \left\{ \frac{4c_1\tilde{\nu}}{3} \left(\frac{\beta_j}{1+z_j^2} \right) - c_2\tilde{\nu}^2 \left(\frac{\beta_j z_j}{1+z_j^2} \right) \right\} \\
+ c_3\tilde{\nu} \left(\Re[\tilde{m}_{n-1}(\tilde{\nu})]^2 - \Im[\tilde{m}_{n-1}(\tilde{\nu})]^2 \right) + \frac{c_4\tilde{\nu}^2}{2} + c_0
\end{aligned} \tag{3.35}$$

where the subscript $n - 1$ signifies its value at the end of the previous iteration. The consequence of adding this second-order component is simply a single extra column for both least-squares matrices \mathbf{M} and \mathbf{N} . In particular, the matrix \mathbf{M} is now of size $K \times (J + 3)$, with an additional column vector inserted at position $J + 1$ given by

$$\text{col}_{J+1} \mathbf{M} = \tilde{\nu}^2 \odot \left(\Re[\tilde{\mathbf{m}}_{n-1}]^2 - \Im[\tilde{\mathbf{m}}_{n-1}]^2 \right) \tag{3.36}$$

Subsequently, the coefficients vector $\boldsymbol{\beta}$ also include an additional element; it is therefore given by

$$\boldsymbol{\beta} = \begin{bmatrix} \beta_1 & \beta_2 & \dots & \beta_k & c_3 & c_4 & c_0 \end{bmatrix}^T, \tag{3.37}$$

Likewise, the matrix \mathbf{N} also includes an additional column, inserted in the third position

$$\text{col}_3 \mathbf{M} = \tilde{\nu}^2 \odot (\Re[\tilde{\mathbf{m}}_{n-1}]^2 - \Im[\tilde{\mathbf{m}}_{n-1}]^2) \quad (3.38)$$

The coefficient vector \mathbf{x} is given by

$$\mathbf{x} = \begin{bmatrix} c_1 & c_2 & c_3 & c_4 & c_0 \end{bmatrix}^T \quad (3.39)$$

Finally, to mitigate any possible instabilities, the new analytical refractive index $\tilde{\mathbf{m}}$ is averaged with its previous value $\tilde{\mathbf{m}}_{n-1}$. Aside from this precautionary measure, the steps outlined in Alg. 1 do not change for the second-order case; they only need use the updated matrices presented in this section.

Estimating Bands From Data

The modeling methods outlined above require an estimate of the bands present in the input spectrum. While many (arguably superior) solutions for peak detection exist (e.g., `findpeaks`, from MATLAB’s Signal Processing Toolbox [135]), we opt to demonstrate a complete modeling process without reliance on any additional paid libraries.

Our approach for estimating positions is achieved by simply locating all local minima of the *second derivative* of the input spectrum (see Fig. 3.9). The use of the second derivative helps locate “shoulder” peaks (bands that do not have a local maximum, since they are too close to a larger neighboring band). To combat the inherent enhancement of noise when differentiating signals, the input spectrum may be smoothed before differentiating. While many options are available for smoothing (the simplest being a convolution of the spectrum with a Gaussian kernel), methods such as Savitzsky-Golay filtering, minimum noise fraction, and wavelet de-noising are useful in spectroscopy due to their ability to suppress high-frequency noise without excessive broadening of line-shape information [7].

After estimating band resonance locations, band widths are estimated by finding the

position of the nearest local minimum to each resonance. The half-width at half-maximum is estimated as the horizontal distance between the resonance position, and the point of the band that is halfway between the height at resonance and the height at the nearest local maximum.

Additional constraints may also be imposed, such as discarding peaks whose widths are above (or below) a threshold.

3.3 Results

Evaluation of the methods proposed in Section 3.2 are carried out both on spectra simulated with exact Mie theory [10], and applied to a focal plane array (FPA) measurement of polystyrene (PS) beads embedded in a potassium-bromide (KBr) pellet.

3.3.1 Simulated Mie Spectra

All simulations are written and performed in MATLAB [135]. We use exact Mie theory (MatScat [143, 144]) to simulate spheres embedded in a homogeneous, non-absorbing background medium. Exact Mie theory is chosen over the van de Hulst approximation, in order to be as true to the physical situation as possible. The background medium has a spectrally constant, real refractive index value n_m , while the sphere has a spectrally-dependent complex refractive index n .

The complex refractive index $n(\tilde{\nu})$ is simulated by assuming the electric susceptibility $\chi(\tilde{\nu})$ is composed of a collection of Lorentzian oscillators [10]. Pseudo-random positions and widths are chosen for each of the oscillators, constrained to loosely resemble the Matrigel reference spectrum, which approximates typical biological spectra [19, 145]. From the susceptibility $\chi(\tilde{\nu})$, the refractive index $n(\tilde{\nu})$ is calculated as

$$n(\tilde{\nu}) = \sqrt{\chi(\tilde{\nu}) + n_0^2}, \quad (3.40)$$

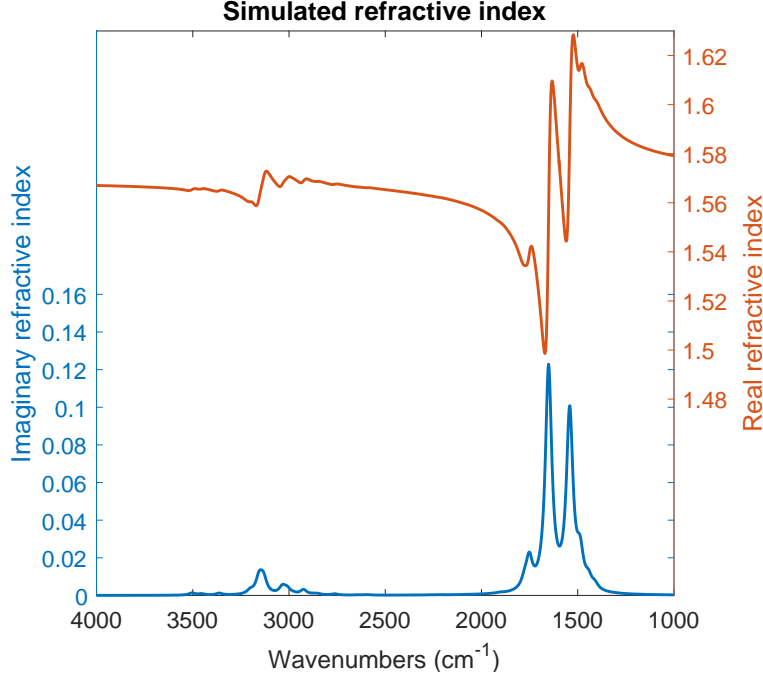


Figure 3.1: A simulated refractive index is composed of Lorentzian bands (visible in the imaginary component) and its Kramer’s-Kronig (visible in the real component). The Kramer’s-Kronig component sits atop a constant refractive index $n_0 = 1.57$.

where the constant refractive index n_0 is added such that, away from absorption bands, $n(\tilde{\nu}) \rightarrow n_0$. A value of $n_0 = 1.57$ was chosen, consistent with polystyrene’s approximate value [146], giving the complex refractive index in Fig. 3.1. The band strengths were chosen to give three distinct orders of magnitude: the weakest bands (~ 0.001) occur around 3500 cm^{-1} ; the second weakest (~ 0.01) are around 3100 cm^{-1} ; the strongest bands (~ 0.1) occur around 1600 cm^{-1} .

The simulated refractive index was used to compare the various models and levels of approximation. Figure 3.2 shows the exact Mie extinction result, compared with the van de Hulst approximation (which we used for obtaining our model), as well as our first and second order approximation models Q_1 and Q_2 (Eqs. 3.7 and 3.8). These results are for a $5 \text{ }\mu\text{m}$ radius sphere with the simulated refractive index $n(\tilde{\nu})$ given above, embedded in a homogeneous non-absorbing background whose (real and constant) refractive index $n_m = 1.53$, approximately consistent with that of KBr [1, 147].

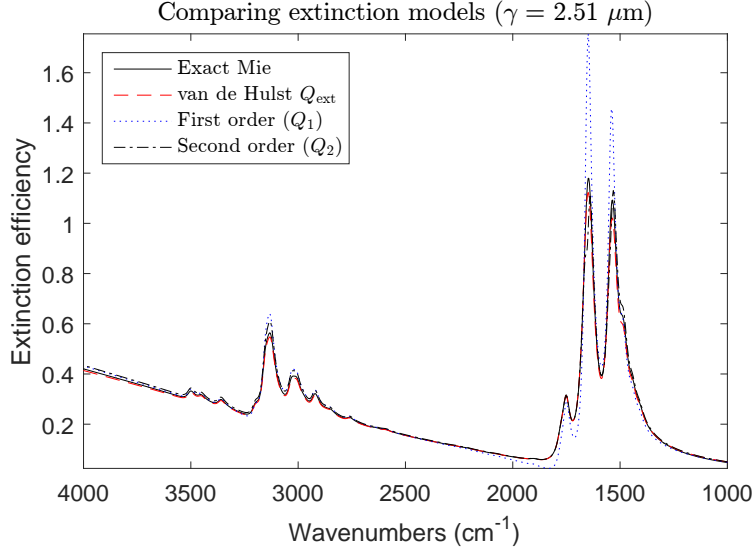


Figure 3.2: Various extinction models are compared against an exact Mie simulation, using the refractive index in Fig. 3.8. Each assume a radius $a = 5 \mu\text{m}$ and a background refractive index $n_m = 1.53$. The first-order model Q_1 shows significant overshoot around the stronger absorbance bands in the 1600 cm^{-1} region. The upper (and lower) bands are examined more closely in Figs. 3.3 and 3.4, respectively.

Figures 3.3 and 3.4 focus on the two primary regions of interest. Figure 3.3 shows results for the weakest- and second-weakest bands, while Fig. 3.4 shows the simulations for the strongest bands.

Fitting was performed using Alg. 1 with the second-order model $Z_2(\tilde{\nu})$ (see Sec. 3.2.1). The results after 150 iterations are shown in Fig. 3.5; the extracted analytical refractive index $\tilde{m}(\tilde{\nu})$ is shown in Fig. 3.6.

Following the results from single Fano-Mie resonances [28], we choose to use an estimated sphere size to estimate the refractive index difference Δ . This choice is motivated by the fact that one often has a very reasonable estimate of the particle size (e.g., brightfield measurements, or from the manufacturer).

3.3.2 PS in KBr

An experimental analog to the simulations in Section 3.3.1 would require embedding a spherical material in an infinite, non-absorbing medium. While this is not practical, we try to

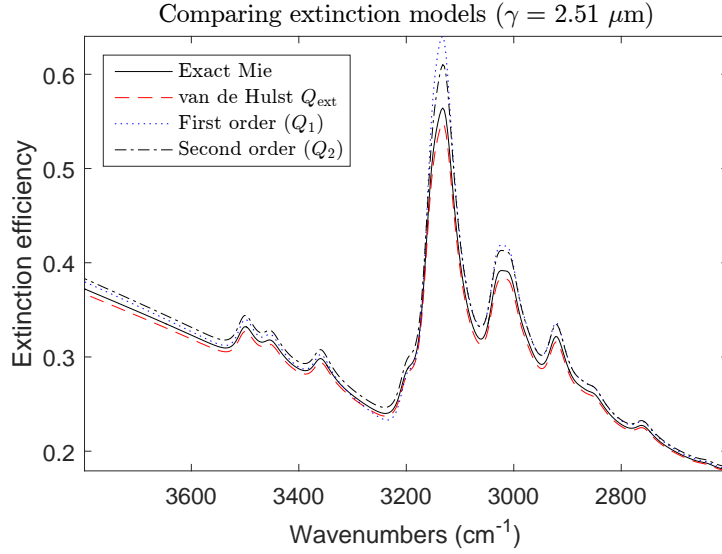


Figure 3.3: Comparing various extinction models in the higher-wavenumber region of Fig. 3.2, where the bands are significantly weaker. Here, while both the first and second order models overshoot slightly from the exact van de Hulst and Mie, there is very little difference between the expansion models Q_1 and Q_2 .

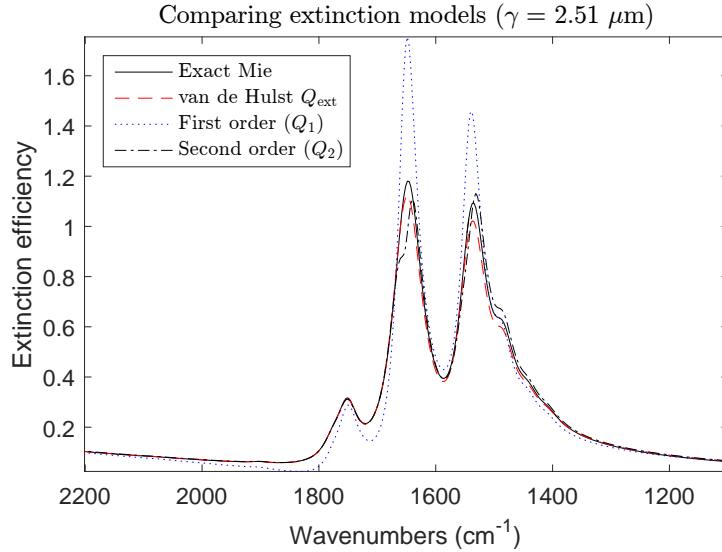


Figure 3.4: The stronger bands from Fig. 3.2 show that accurate modeling requires the second-order model Q_2 when the bands are stronger, as the linear-order expansion model Q_1 shows significant overshoot from the other models.

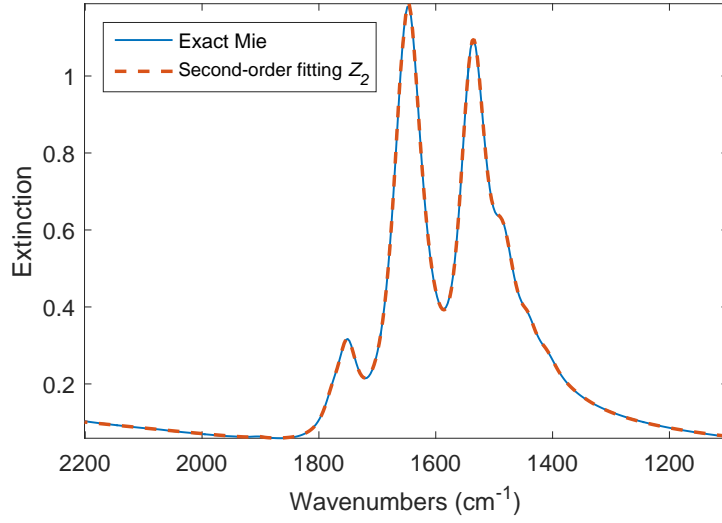


Figure 3.5: Fitting the second order model Z_2 to the stronger bands of the exact Mie simulation in the 1600 cm^{-1} region (Fig. 3.4). The estimated peak positions (and their refined values) are displayed in Fig. 3.7.

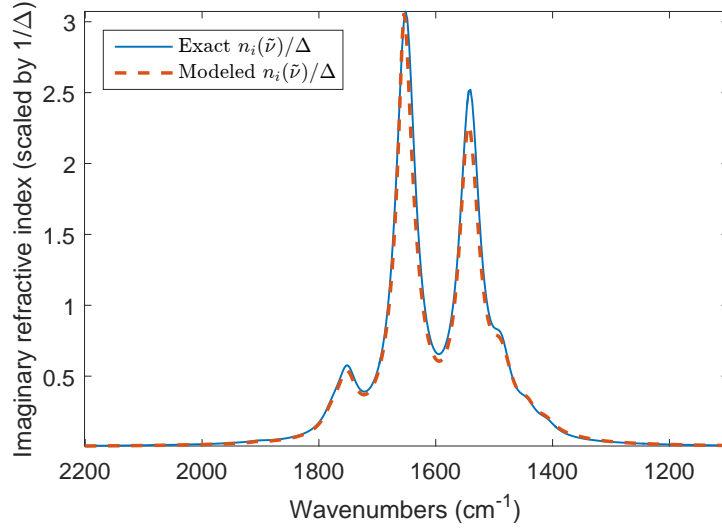


Figure 3.6: The extracted (scaled) imaginary refractive index (from the second-order fitting in Fig. 3.5) compared with the exact refractive index shown in Fig. 3.1. The extracted refractive index is inherently scaled by $1/\Delta$. Although the fitting is nearly perfect in Fig. 3.5, the extracted refractive index shows some discrepancy, due to the model's approximation errors (see Fig. 3.4, Q_2).

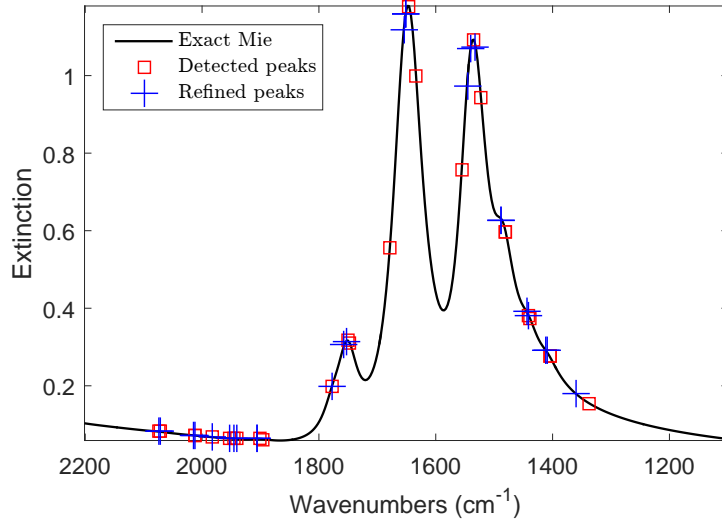


Figure 3.7: Detected peak positions that were used as input for the modeling process in Fig. 3.5. Also displayed are the updated positions that have been refined by the gradient descent step in Alg. 1.

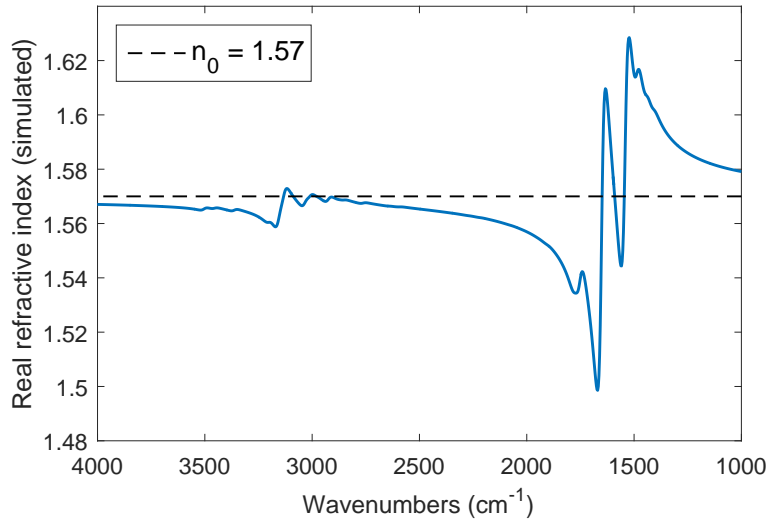


Figure 3.8: The fluctuating component of the real refractive index around 3200 cm^{-1} shows a slight deviation from n_0 , due to residual influences of the strong bands in the 1600 cm^{-1} region.

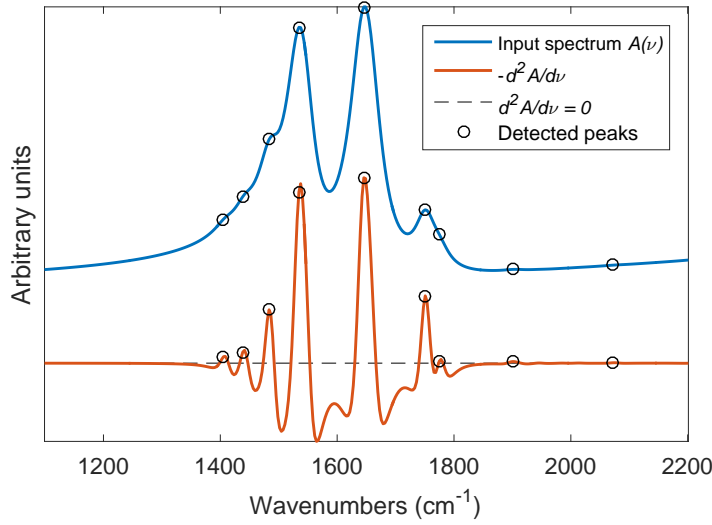


Figure 3.9: Peak detection is performed using the second derivative of the input spectrum $A(\tilde{\nu})$. Shown is the (negative) second derivative of the input spectrum $A(\tilde{\nu})$; each of its local maxima greater than zero (dashed line) identify a peak position.

get close by embedding a 10 μm (diameter) PS bead in an approximately 1 mm thick KBr pellet. To create this pellet, we filled a die halfway with KBr powder and scraped a small amount of PS beads, which had been suspended in water and allowed to dry on a glass slide, into the die. The die was filled with additional KBr and placed in a press to create the pellet.

To measure an individual bead, the pellet was placed in a Bruker Hyperion 3000 microscope, connected to a Bruker Vertex 70 interferometer. The microscope was equipped with a 36 \times Schwarzschild objective, and an isolated bead was located using a visible light camera. Once a bead was selected, an FTIR measurement was performed using an focal plane array detector attached to the microscope. Data was taken from 3847.2 cm^{-1} to 3847.2 cm^{-1} , with a resolution of 1.9 cm^{-1} , averaged over 100 scans.

Figure 3.10 shows an extinction image of the PS bead, obtained at $\tilde{\nu} = 3024 \text{ cm}^{-1}$. An average spectrum over the field of view approximately enclosed by the indicated green circle is provided in Fig. 3.11.

The high-frequency region (about 3500 cm^{-1} to 2500 cm^{-1}) of this spectrum was used

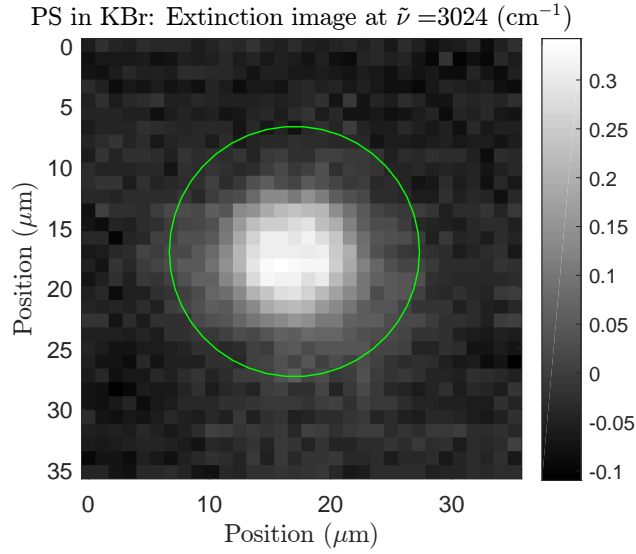


Figure 3.10: Measured extinction image at $\tilde{\nu} = 3024 \text{ cm}^{-1}$. The green circle is the approximate region used to obtain the average spectrum in Fig. 3.11.

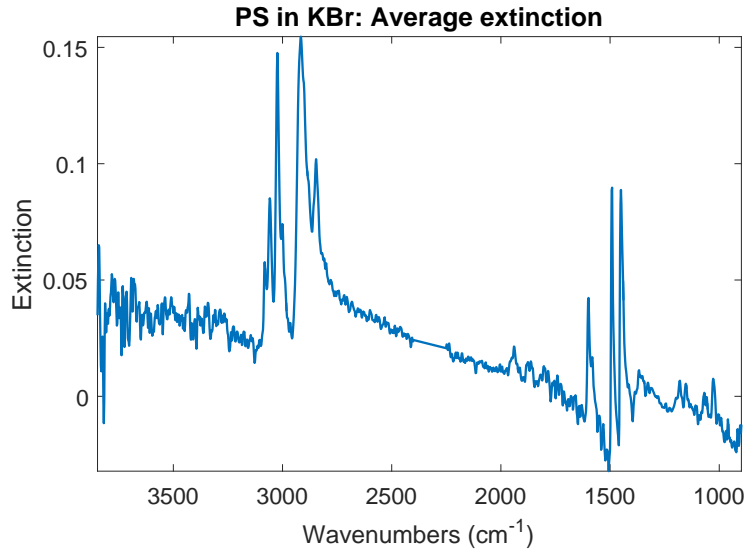


Figure 3.11: Extinction spectrum averaged over the region shown in Fig. 3.10. The CO₂ region (2400 cm^{-1} to 2250 cm^{-1}) has been removed. The high-frequency bands (around 3000 cm^{-1}) are modeled with the second-order model Z_2 (see Fig. 3.12).

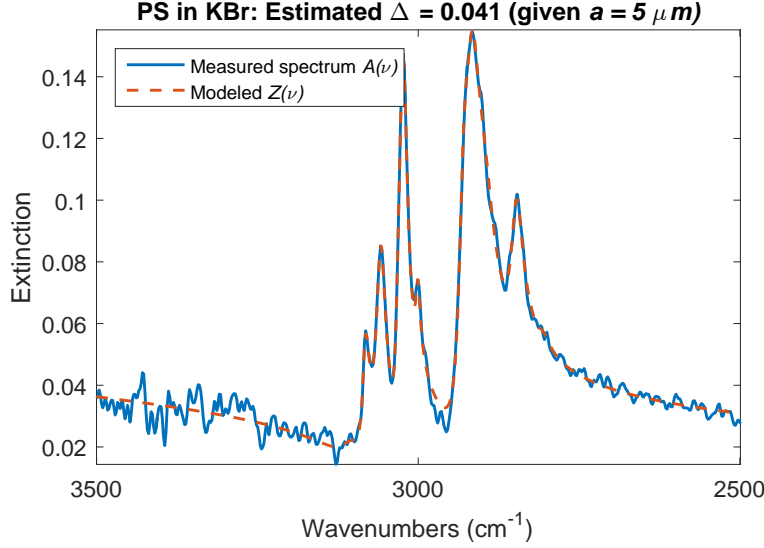


Figure 3.12: Modeling results after 160 iterations. Using the manufacturer's specification of $a = 5 \mu\text{m}$, the estimated refractive index difference is $\Delta \approx 0.041$.

to fit the model $Z_2(\tilde{\nu})$, using Alg. 1. The input spectrum $A(\tilde{\nu})$ and fit model are shown in Fig. 3.12.

The model $Z_2(\tilde{\nu})$ fit to the measured spectrum $A(\tilde{\nu})$ produces the Mie parameter $\gamma \approx 2.58 \times 10^{-4} \text{ cm}$, along with the analytic refractive index $\tilde{m}(\tilde{\nu})$ shown in Fig. 3.13. Using the manufacturer's specification of a $10 \mu\text{m}$ diameter bead (i.e., $a = 5 \mu\text{m}$), the predicted global refractive index difference (in the region around 3500 cm^{-1} to 2500 cm^{-1}) between the PS bead and its surrounding KBr medium is $\Delta \approx 0.041$.

3.4 Discussion

Extending the pure extinction model $Q_n(\tilde{\nu})$ (either Eqs. 3.7 or 3.8) to practical intensity measurements requires additional modifications that take into account various deviations from the idealized mathematical theory. For instance, standard Mie theory is given for a plane wave [10, 15]; the inclusion of apertures, condensers, and focusing optics typically used in FTIR microscopes will alter the measured intensity [142, 148].

Environmental conditions will also affect the validity of the pure extinction model. This

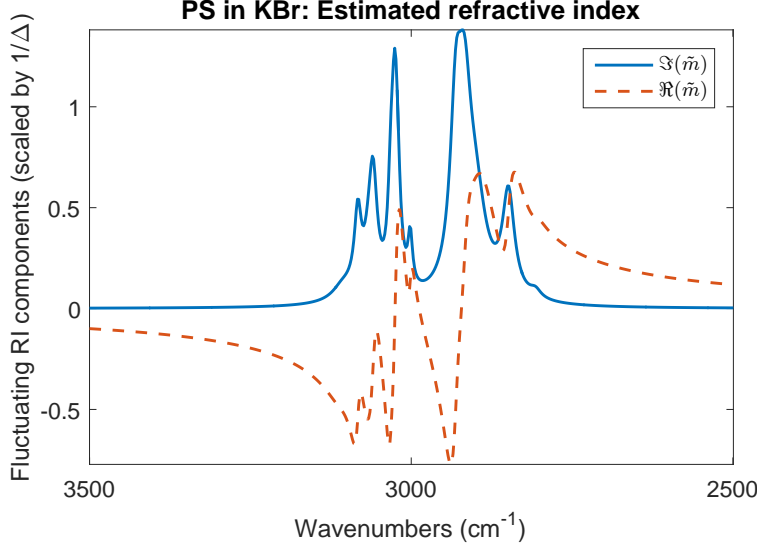


Figure 3.13: Extracted refractive index \tilde{m} for PS using the modeling in Fig. 3.12.

includes standard factors like measurement noise and environmental conditions (e.g., humidity), but also baseline errors due to imperfect reference measurements. Despite cognizant efforts to mitigate this possibility during experiment (e.g., by taking reference measurements in a “clean” region very near to the sample of interest), these effects are sometimes unavoidable.

We attempt to account for many of these factors in our extension of the pure extinction model $Q_n(\tilde{\nu})$ to the generalized extinction model $Z_n(\tilde{\nu})$, although we recognize that this generalization may not provide adequate justice—especially when considering the complex role that optics play. Nonetheless, we proceed using the modifications presented in Eq. 3.10. First included is an overall scaling factor σ_0 , whose role is to approximate the effect of measurement optics [142]. Second, we account for possible differences in the background medium thickness between the sample and reference measurement with the inclusion of an additional constant offset c_0 .

There are a number of options available for modeling $n_i(\tilde{\nu})$ in Eq. 3.8. One method is to use an existing reference spectrum, where extraction of $n_i(\tilde{\nu})$ is accurate in the Beer-Lambert limit—for example in thin film measurements where scattering effects are negligible. The Kramer’s-Kronig transform $\hat{n}_i(\tilde{\nu})$ may be calculated digitally (with accuracy depending on

the edge effects [149, 150]), or if available, obtained from reflection spectra. While indeed such a priori information would significantly simplify the modeling process, our goal is to have as general of a modeling process as possible, applicable to biological media where the refractive index may not be known (or where subtle variations are of interest). We therefore chose to directly model the refractive index using only the assumption of Lorentzian oscillators.

In the algorithm for modeling $Z_n(\tilde{\nu})$ with Lorentzian oscillators, explicit separation of the model into two matrices \mathbf{M} and \mathbf{N} is necessary to constrain the modeled analytic refractive index $\tilde{m}(\tilde{\nu})$ such that its real and imaginary components are Kramer’s-Kronig transform pairs. If a single coefficient for the two Lorentzian functions were used (i.e., only a single least-squares matrix is used), each Lorentzian oscillator may have a different magnitude for its imaginary and real component. Then, when multiple oscillators are summed together, the real and imaginary components will not, in general, have the Kramer’s-Kronig constraint. The modeling therefore requires two least-squares solutions to enforce this condition.

The modeling method presented has assumed Lorentzian oscillators. While these are typical for vibrational spectroscopy, depending on the data and the preprocessing steps (such as interferogram apodization), Gaussian or Voigt bandshapes may model the data more accurately [1, 2].

Finally, since the model $Z_n(\tilde{\nu})$ (Eq. 3.10) is compatible with existing scatter-correction models such as Extended Multiplicative Scatter Correction (EMSC) [17, 18, 22, 145], may also be extended to include additional effects such as fringes [8, 141]. Such an extension would see the same restrictions outlined in that work. In particular, modeling fringes would necessitate an estimate of the fringe frequency. However, if the fringe strength is sufficiently small (and does not confuse with chemical bands), the fringes may be isolated by removal of the fit chemical components. Such modeling is outside the scope of this manuscript.

3.4.1 Simulations

It is not our purpose to develop here a complete software package. The algorithm outlined in Alg. 1 may not be optimal; our foremost focus is an evaluation the accuracy of the model in Eq. 3.10. Therefore, an exhaustive evaluation of the algorithm, including performance and stability analysis are outside the scope of this manuscript. We focus instead on determining the physical conditions required for minimal error between the model $Z_n(\tilde{\nu})$ and a given extinction spectrum $A(\tilde{\nu})$. This includes oscillator α_j strengths and magnitudes of the Mie parameter $\rho_0(\tilde{\nu})$.

3.4.2 PS in KBr

Devising an experiment adhering to the conditions of Mie theory would require a sphere suspended in a homogeneous, non-absorbing background medium of infinite extent. For FTIR microspectroscopy experiments, however, this is not only an impractical requirement, but also highly unrealistic situation. Often very thin samples, on the order of ten microns, are measured—and while this may be approximated as infinite in the lateral extent, the finite thickness often produces multiple scattering artifacts (such as fringing[8, 141]) in the measured spectra. A thicker medium is therefore desired, although this runs the risk of dramatically reducing the signal-to-noise ratio. Furthermore, biological samples will likely have absorption bands that overlap with those of spherical objects of interest (e.g., cells in a tissue), since the overall chemical makeup will be similar.

As noted earlier, exact Mie theory is usually solved by considering a plane wave incident on the sphere, with a collimated detector downstream measuring the forward extinction [10]. However, typical FTIR systems employ focusing optics; a better model for spherical scattering should take these into account, e.g., using methods presented in BIM-SIM [148]. Given the finite thickness of the KBr medium, the possibility of surface imperfections (which may present as fringing artifacts [8, 141]) should also be taken into account.

Nonetheless, application of the modeling presented in Alg. 1 shows that indeed the ap-

proach can model the extinction spectrum of a PS bead embedded in a finite KBr medium (see Fig. 3.12). Furthermore, using the manufacturer’s specified radius $a = 5\text{ }\mu\text{m}$, a global refractive index difference $\Delta \approx 0.041$ is extracted from the modeling, consistent with the theoretical value of about 0.04.

3.5 Conclusions

Presented was an approximation model of the van de Hulst extinction, that is valid for weakly scattering spheres whose absorbance bands are also weak (typical for many mid-infrared spectra of biological materials). The model generalizes previous results that model single, isolated bands with Fano theory [28], to the case of multiple (and overlapping) bands. Then, with the assumption of Lorentzian oscillators, we presented an algorithm that fits this model to measured extinction spectra, allowing extraction of certain Mie parameters, and a scaled model of the fluctuating components of the sphere’s complex refractive index. Additionally, with further information such as the size of the sphere, an estimate of the constant refractive index difference between the sphere and its surrounding medium may be obtained; this allows removal of the scaling from the extracted (fluctuating) complex refractive index. The modeling algorithm is applied to simulated spectra, and a demonstration of the methods on a polystyrene bead embedded in potassium bromide is presented.

In certain instances, having the imaginary RI may be more valuable than the pure absorbance spectrum. The imaginary RI is an inherent property of the sample, providing very similar chemical information as the absorbance but without dependence on the sample’s thickness [10, 29]. However, much work remains to be done if the multi-peak Fano approach is to compete with the latest, highly efficient Mie scatter-correction methods [22]. Presented here is a very basic algorithm for both peak detection and fitting. Immediate improvements in stability and performance may be made by implementing an established algorithm for non-linear least squares fitting, such as the Levenberg-Marquardt method [30, 31]. Statis-

tical measures for selecting dielectric band models and distinguishing signal and noise may also be utilized, such as the Akaike Information Criterion [32, 33].

The value of Fano and multi-peak Fano fitting is not limited to explicit scatter correction. Often, curve fitting is applied using sums of Lorentzians or Gaussians [1, 2] using, for instance, the Levenberg-Marquardt method [34]. The methods that have been applied in our work on spheres strongly suggests that even for non-spherical scatterers, proper curve-fitting should also account for the real RI component. This is also supported by previous observations by Romeo and Diem [9], along with the work of Davis, Carney and Bhargava [11, 12]. For example, an investigation of mineral biological tissues in 2015 performed peak fitting using the Levenberg-Marquardt method with Lorentzian bands [35]. Observations of their spectra however, show the signature Fano-like characteristics, and may therefore have benefited from including the real RI component.

3.6 Future Work Applied to Hyperspectral Imaging

Until this point, the methods and results presented here and for Fano fitting (Chapter 2) have largely been theoretical, without any application to practical experiments. Although the multi-peak modeling algorithm was demonstrated on an experiment to support the methods, practical usefulness of the modeling, especially to hyperspectral microspectroscopic imaging, remains to be resolved.

As discussed in Sec. 3.5, Fano and multi-peak Fano fitting may be useful for proper curve-fitting, which should account for the real RI component. Another possible next step is to incorporate the model with the latest scatter correction algorithms, particularly the extended multiplicative scatter correction (EMSC) approach [21, 22]. The effective linearization of the van de Hulst model (Eq. 3.10) may improve computation speed, valid for weakly scattering spheres.

We discuss here, however, next steps that have been explored in order to extend the

methods to non-spherical scatterers, along with applicability to hyperspectral datasets rather than single spectra that have been collected over a field of view. One possible avenue for dealing with pixelated (hyperspectral images) is to expand on the methods and results presented by Berisha and van Dijk, et al. [148, 151]. These authors provide a highly detailed model for Mie scattering in conventional FTIR microscopes, which includes careful modeling of the Schwarzschild objectives.

Alternatively, we investigate an approach for modeling hyperspectral images acquired for arbitrary non-spherical samples, similar to work performed by Kohler et al in 2005 [152]. There, Kohler et al used extended multiplicative signal correction (EMSC) to resolve physical and chemical information separately. Their methods identified spectral scatter effects as being due to the physical properties of the sample, and that a coupling between the chemical and scatter properties may occur. By preprocessing spectra with EMSC, they were able to separate the scatter from the chemical information. Based on the observation that Fano-like signatures appear in many varieties of infrared samples [9, 128], it is reasonable to expect that a very similar decomposition to that presented by Kohler et al, using Eq. 3.10 may hold for spectra with weak scattering signatures. We therefore fit each pixel from the hyperspectral dataset used in Sec. 3.3.2 to the following model

$$\begin{aligned}
Z(x, y; \tilde{\nu}) = & F(x, y)n_i(\tilde{\nu}) + G(x, y)\hat{n}_i(\tilde{\nu}) \\
& F_2(x, y)n_i^2(\tilde{\nu}) + G_2\hat{n}_i^2(\tilde{\nu}) + H(x, y)n_i(\tilde{\nu})\hat{n}_i(\tilde{\nu}) + \\
& B_2z^2 + B_1z + B_0
\end{aligned} \tag{3.41}$$

where $z = (\tilde{\nu} - \tilde{\nu}_0)/\tilde{\nu}_{\max}$ is the centered and normalized wavenumber axis, equal to $-1, 0$, and 1 for wavenumbers $\tilde{\nu} = \tilde{\nu}_0 - \tilde{\nu}_{\max}$, $\tilde{\nu} = \tilde{\nu}_0$, and $\tilde{\nu} = \tilde{\nu}_0 + \tilde{\nu}_{\max}$, respectively.

The fitting is performed on four sets of measurements, using the real and imaginary components of the extracted analytical refractive index $\tilde{m}(\tilde{\nu})$ shown in Fig. 3.13. The images F, G, B_2, B_1 , and B_0 for this fitting are shown in Fig. 3.14. The images shown in each of these

terms consist of four distinct 10 μm diameter PS beads embedded in KBr; two of the beads present Mie scatter signatures predicted by the modeling in Sec. 3.2 (Fig. 3.15, upper)⁴, while the other two beads present much stronger scatter (Fig. 3.15, lower). The strong scatter signatures are likely attributed to hydration from beads that weren't completely dried before entering the KBr. This is supported by the presence of hydration bands around 3280 cm^{-1} .

The first thing to note is that the images F and G have signs and magnitudes consistent with the expected modeling from Section 3.2. In particular, the expected value of ρ_0 (given by Eq. 3.5) in the region $\tilde{\nu}_0 \approx 3000 \text{ cm}^{-1}$ for a 5 μm radius PS bead whose refractive index difference from its KBr medium is $\Delta \approx 0.04$ is $\rho_0 \approx 0.754$. From Eq. 3.11, ρ_0 should be roughly proportional to the ratio of the images: $\rho_0 \approx -\frac{4}{3}(G/F)$. The upper (low scatter) spheres give $\rho_0 \approx -\frac{4}{3}(-0.14/0.25) = 0.747$, consistent with the predicted value.

The second striking observation is the appearance of diffraction-like features, notably in the linear B_1 images for the two high-scattering spheres. These features are not present for the low-scatter spheres. What is also interesting is the gradient-like feature at the center of both of the high scattering spheres in the quadratic B_2 term. Both spheres show the same sudden transition between negative and positive values at their centers.

Since the overall background $B(x, y; \tilde{\nu}) = B_2 z^2 + B_1 z + B_0$ is wavelength-dependent, a few images are presented in Fig. 3.16 corresponding to the spectral locations shown in Fig. 3.17. While these images appear relatively constant for the weakly-scattering spheres, the two stronger spheres show changing features as a function of wavelength. What is interesting is that the brightest ring transitions from a figure-eight appearance in the higher wavenumber region, to a doughnut appearance toward the lower wavenumber region. Next steps could explore these observed features, perhaps using the methods presented by Berisha and van Dijk, et al. [148, 151], as discussed previously.

The methods developed in Sec. 3.2 assume a homogeneous, non-absorbing background

⁴The first bead (Fig. 3.15, upper left) was in fact used in the results Sec. 3.3

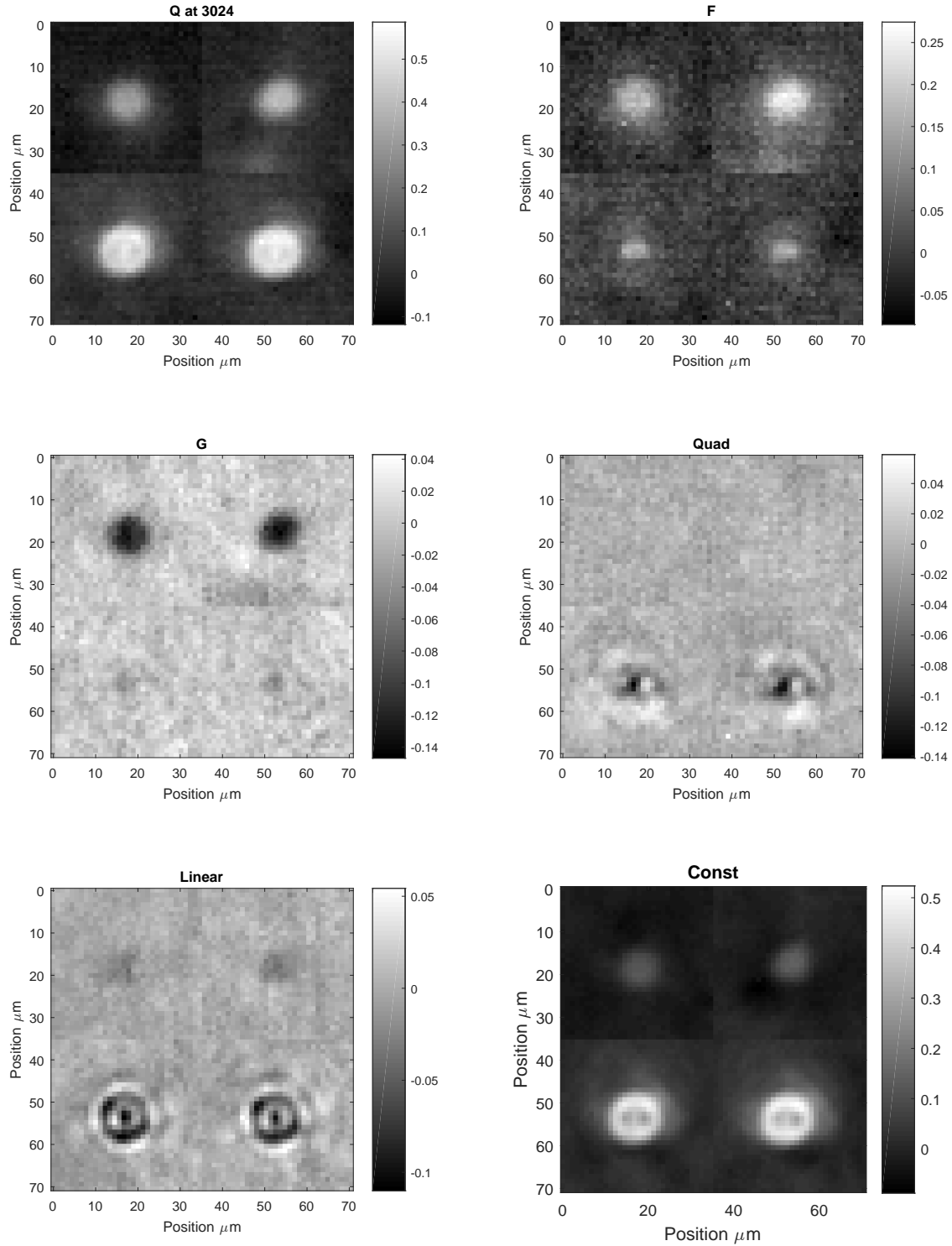


Figure 3.14: Pixelated expansion of using the model in Eq. 3.41. Each of the six images contains four samples; the upper two are weak scatterers (see spectra in Fig. 3.15, upper), while the lower two have stronger scatter signatures (see spectra in Fig. 3.15, lower).

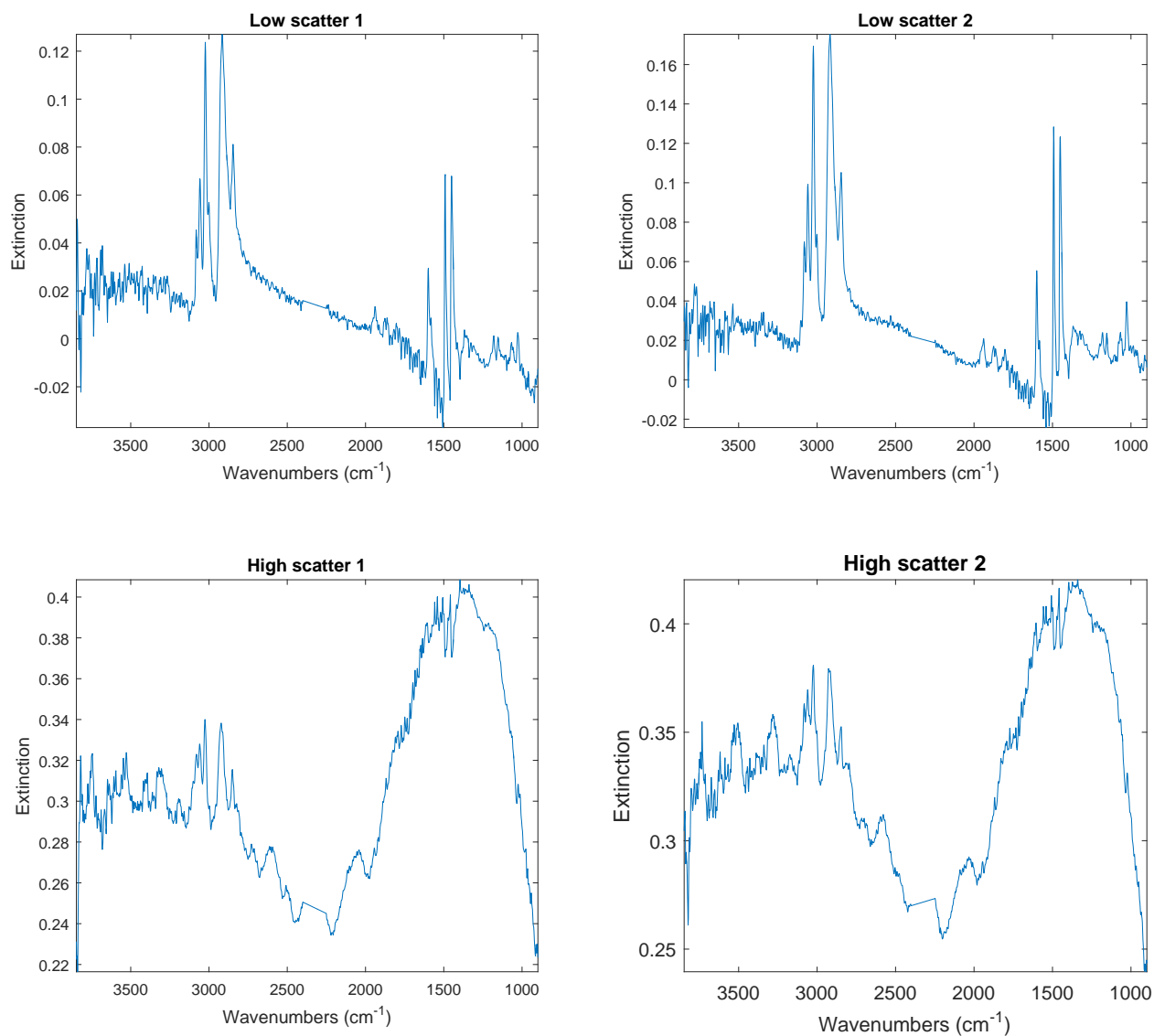


Figure 3.15: Average spectra for each of the four images in Fig. 3.14. The CO₂ region (around 2300 cm⁻¹) has been removed from all spectra.

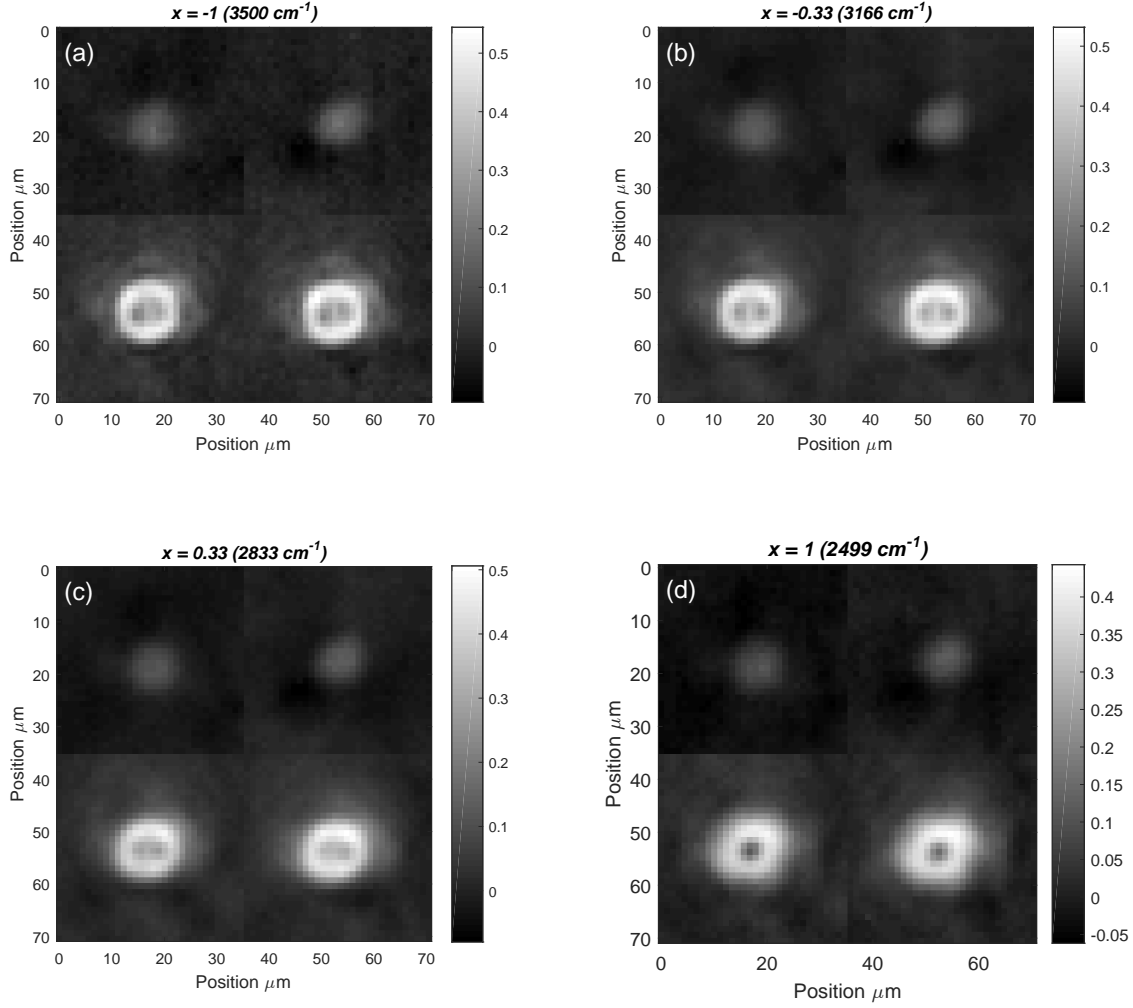


Figure 3.16: The spectral dependence of the background images. The four images ((a) through (d)) are taken at the positions indicated within the spectral range shown in Fig. 3.17. The high wavenumber image (a) shows more diffraction-like features for the bottom two high-scattering spheres. Furthermore, the innermost prominent rings for the bottom two spheres appear to be partitioned down the middle (a slight figure-eight appearance), whereas the rings are completely hollow in the low wavenumber image (d). The structure of the upper (low-scattering) spheres appear very similar accross each of the wavenumber positions in (a) through (d).

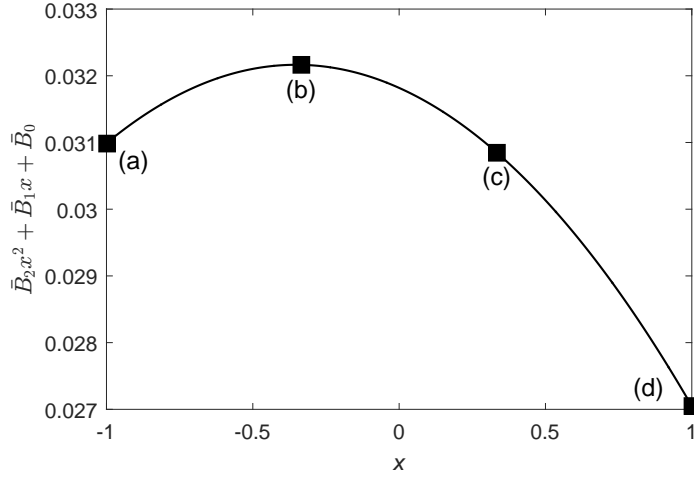


Figure 3.17: The positions corresponding to the background images shown in Fig. 3.16. The displayed curve is the background averaged over all pixels from each of the coefficients B_2 , B_1 , and B_0 .

medium. As this is unrealistic in many situations, especially biological media where the chemistry makeup between scatterers (e.g., cells), and their surroundings are very similar [7, 61], next steps may also include a generalization of the modeling presented in Section 3.2 to account for absorbing background media.

With these limitations understood, the modeling is performed on a dataset of PS in a polyurethane (PU) medium (Fig. 3.18). While thorough analysis is complicated by overlapping bands between PS and PU, the expansion methods are nonetheless applied on the 3026 cm^{-1} band, which is present in PS, but not in the PU medium. Figure 3.18 shows the expansion for the images F , G , B_2 , B_1 , and B_0 , using the same analytic refractive index used previously (obtained in Sec. 3.3.2).

Curiously, these expansions show the presence of a very subtle shift between the peaks (or valleys) in each of the images. The shifting is most evident between F , G , and the linear and constant terms B_1 and B_0 . Without any further evidence, the shifting can only be attributed at this time to the likelihood of the incident beam being at an angle with the sample. In fact, this data was taken with a synchrotron source, which has been noted as being aligned such that it is focused by the condenser at an angle relative to its ideal optical

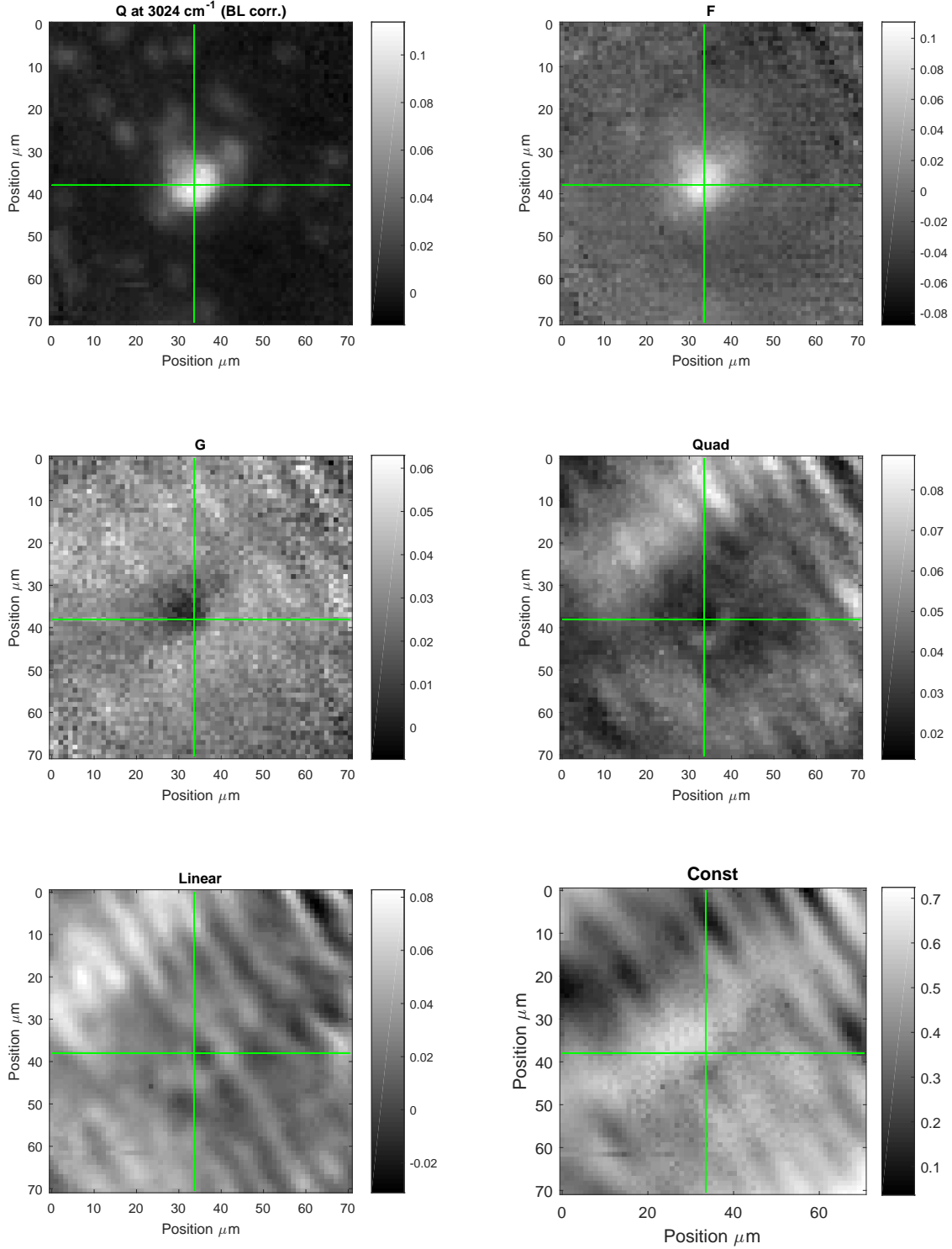


Figure 3.18: Pixelated expansion of PS beads in a PU matrix, using the model in Eq. 3.41. While the analysis is complicated by the overlapping bands between the medium and sample, some interesting features appear. Namely, a very subtle shifting occurs between the apparent bead locations—most notably between F , G , and the linear and constant terms B_1 and B_0 . The extinction image (upper left) has been baseline corrected about the 3024 cm^{-1} band.

axis. Furthermore, the likelihood of the beam being at an angle is supported by the evidence of spatial fringes apparent in the spectral images.

A possible explanation for the observed shift between the absorbance and scatter images in Fig. 3.18 is sketched in Fig. 3.19. While the full wave theory should be used (e.g., using the methods in Ch. 5, Sec. 5.1), ray optics help illustrate the situation. Shown is a medium of finite thickness (infinite in lateral extent), with an embedded spherical scatterer. The central, forward ray is the path traversed by the infrared source, which enters the medium at an angle relative to its normal. Since the medium has a constant refractive index $n_m > 0$, the rays refract when entering or leaving the medium. Therefore, an observer from above will see a displaced image of the spherical scatterer along the forward path, depicted in the diagram as the “forward virtual image.” However, scattered rays appear to originate from a slightly offset position, depicted in the diagram as the “scattered virtual image.” This effect may also be understood simply as an aberration: back-projected rays do not converge to the same location. Since the images in Fig. 3.18 represent a decomposition of scattering and non-scattering terms in Eq. 3.41, the apparent offset behavior may be resolved from this spectral expansion. Another next step may be testing whether this effect is observable when using a stage with precise control over its tilt angle.

In this interpretation, the expansion images G , B_2 , B_1 , and B_0 are likely modeling the scattering behavior of the PS bead; however, the significance of each of the images has yet to be fully understood. A full theory that correctly handles spectral absorbances in the background medium may ultimately be required in order to properly perform this pixelated expansion.

A final observation of this dataset is the suppression of spatial fringes in the F image, compared to the other expansion terms. It is only hypothesized at this point that, since the F term is predominantly related to the absorbance (the imaginary refractive index), this term may have a bias toward absorbance features, whereas the other terms model diffraction or scattering features. This interpretation, however, is purely speculative. Future efforts

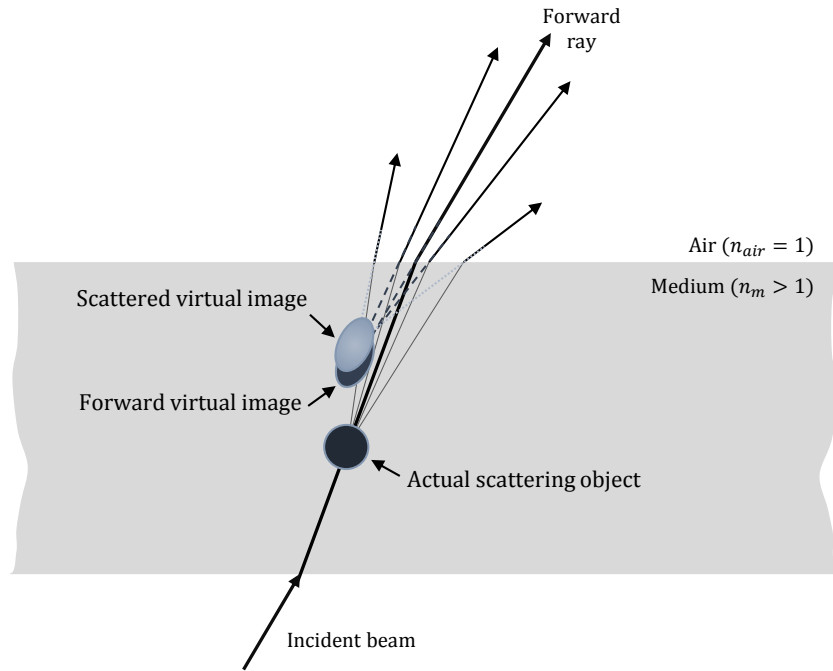


Figure 3.19: A theorized explanation for the observed shift between images in the pixelated expansion shown in Fig. 3.18. Since the incident beam enters at an angle, the scattered rays – while symmetric about the forward ray *inside* the medium – do not exit the medium symmetrically. Therefore, the scattered rays appear to originate from a slightly offset position (“scattered virtual image”), compared to the non-scattered rays (“forward virtual image”).

to investigate this may include diffraction methods presented in Chapter 5 (Sec. 5.1). For example, the the expansion model $Z(x, y; \tilde{\nu})$ (Eq. 3.41) may be improved by incorporating fringing terms [8, 141].

Ultimately, the analyses on hyperspectral images has provided very interesting, albeit difficult to interpret results. Multiple complexities prevent direct application of fundamental electromagnetic theory to the problem, including low spatial coherence, the loss of field phase and polarization information, poor signal-to-noise ratios, and (effectively) hidden optics in the microscope.

The low spatial coherence and SNR comes from the use of a global light source⁵, which is relatively weak compared to synchrotron and laser sources. Many datasets used a synchrotron source (for example, the PS in PU dataset discussed above), which indeed has improved SNR over a global source – so long as a region where the beam is relatively homogeneous over the detector area has been imaged [153, 154]. And while the synchrotron did exhibit a high degree of spatial coherence, both the quality of its wavefront suffered (after passing through the optical system), and the fact that multiple beams were merged [153, 154] results in a loss of coherence.

Another limitation is an inherent loss of electromagnetic phase, as the detector only responds to the field intensity. The field phase is a crucial quantity, especially in inverse scattering problems [42, 56, 58]. For these listed reasons, development of a custom microscope for holographic infrared microspectroscopy is underway. The fundamental theory of its operation is presented next, in Chapter 4, while possible applications and next steps are discussed in Chapter 5 (Sec. 5.1). A basic overview of holography is given in Appendix 5.2.5.

⁵A global source is very similar to an incandescent light bulb, though designed without glass (which blocks infrared radiation).

Chapter 4

Fourier-Transform Holographic Spectroscopy

A method for measuring the electric field phase information in mid-infrared spectroscopy is presented. This is achieved by replacing the typical Michaelson interferometer with a modified Mach Zehnder that contains a translating mirror. We show that interferograms collected with this design may be Fourier-transformed to obtain a complex spectrum whose phase and magnitude are related to that of the sample's scattered electric field. While the design sacrifices modularity, it allows retention the sample's phase spectrum, important for scatter correction and diffraction-type measurements [29, 42, 79, 136]. To demonstrate our methods, a prototype microscope was constructed using off-the-shelf prototyping components from Thorlabs and Newport. The microscope is demonstrated by obtaining an emission spectrum of a near-infrared source, along with a hologram of a small micro-loop, which is digitally re-focused without the twin-image effect (see Appendix). While consumer-grade near-infrared source and optical components were used, ultimately we propose an experimental design that makes use of recent advances in mid-infrared technology, including a supercontinuum laser (Thorlabs), and a high-resolution liquid nitrogen-cooled focal plane array detector.

4.1 Introduction

In classical Fourier-transform spectroscopy (FTS), the transmission spectrum of a sample is obtained by placing it after a Michaelson interferometer. While this arrangement allows for a compact and minimal design, an unfortunate drawback is an inherent loss of phase information upon conversion of the electric field to intensities by the detector. In FTS, the (theoretically) measured interferogram is symmetric about the zero path difference (ZPD); the resulting spectrum (calculated via the Fourier transform) is therefore real-valued.

Fourier-transform holographic spectroscopy (FTHS), on the other hand, sacrifices this modular design in exchange for retaining phase information. FTHS uses a setup based on the Mach Zehnder configuration, where measurements are performed by placing a sample in the arm of one of the paths. Phase changes induced by a sample in this setup are encoded by the interference between the two paths at the detector. In this case, the measured interferogram is no longer symmetric about the ZPD; the resulting spectrum is complex-valued, and its magnitude and phase are related to the absorbance and phase of the scattered field, respectively.

It will be shown how the theory of Fourier-transform spectroscopy can be adjusted for use in a Mach Zehnder interferometer, to record both amplitude and phase information from a sample. Furthermore, FTHS is shown to be a generalized version of phase-shifting holography [98].

4.2 Methods

4.2.1 Fourier-Transform Spectroscopy

In FTS, a Michaelson interferometer is used to split a collimated broadband source into two fields, which are recombined with an induced relative phase difference. An interferogram is obtained by sufficiently sampling over many path-length differences, which may then be

Fourier transformed to obtain the source’s spectrum. Insertion of a sample before (or after) the interferometer multiplies its spectrum with that of the source. By dividing out the source spectrum, a pure sample spectrum is obtained (assuming identical environmental and instrumental conditions in both cases). It is customary to refer to the process without a sample as the “background” measurement, while a “sample” measurement is obtained with the sample in place.

The mathematical details are illustrated by first decomposing a broadband field as a collection of uncorrelated, quasi-monochromatic plane waves whose wavenumber $\tilde{\nu} = 1/\lambda$ is inversely proportional to its wavelength λ . Since the waves are uncorrelated, the total field intensity $\bar{I}(\vec{r})$ at coordinate position \vec{r} may be written as an integral over the intensities of each quasi-monochromatic field [2]

$$\bar{I}(\vec{r}) = \int_0^\infty I_{\tilde{\nu}}(\vec{r}) d\tilde{\nu} \quad (4.1)$$

where $I_{\tilde{\nu}}(\vec{r})$ is the quasi-monochromatic field intensity for the wavenumber $\tilde{\nu}$.

To proceed, the experiment will first be described mathematically for a single quasi-monochromatic field $U(\vec{r})$, with the total measured intensity for a broadband source given by the integral in Eq. 4.1. For notational simplicity, the spatial coordinate \vec{r} will be omitted hereafter, as it does not provide any additional clarity. (The spatial dependence will of course become important once details of the imaging process are considered; for now, we only illustrate the spectroscopic details.)

Given a plane wave $U = A_{\tilde{\nu}} \exp(i2\pi\tilde{\nu}z)$ whose axis of propagation is along z , a Michaelson interferometer splits U into $U_1 = \frac{A_{\tilde{\nu}}}{\sqrt{2}} \exp(i2\pi\tilde{\nu}z)$ and $U_2 = \frac{A_{\tilde{\nu}}}{\sqrt{2}} \exp(i2\pi\tilde{\nu}z)$, which later recombine after traveling their own respective distances. Here, $A_{\tilde{\nu}}(\vec{r})$ is the field’s amplitude at wavenumber $\tilde{\nu}$. For convenience, it is assumed that the field is equally split (and recombined) without any losses. However, a straightforward generalization to imperfect beamsplitters is made in Sec. 4.2.3.

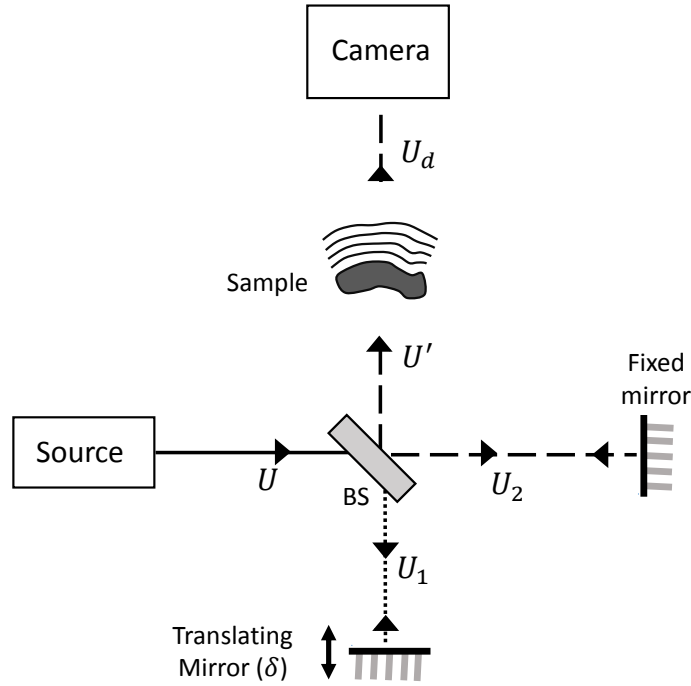


Figure 4.1: Fourier-transform spectroscopy using a Michaelson interferometer. A broadband source is split into two paths by a beamsplitter (BS). Along the first path, the field U_1 is reflected by a translating mirror before transmitting through BS and recombining with the second path. Along the second path, the field U_2 is reflected by a fixed mirror before being reflected by BS and recombining with the first path. The combined fields U' interact with the sample before arriving at the camera.

If the recombined field is U' , it will be given (up to a constant phase factor) by

$$U' = \frac{1}{\sqrt{2}} (U_1 \exp(i2\pi\tilde{\nu}\delta) + U_2) \quad (4.2)$$

where δ is the difference in path length traversed by each of the separated fields, and $\tilde{\nu} = 1/\lambda$ is the wavenumber in terms of the wavelength λ . The path-length difference δ can be achieved in a number of ways, including a simple translation of a single mirror while keeping the other fixed (see Fig. 4.1).

When a sample is placed outside of the interferometer, as shown in Fig. 4.1, both fields $U_1(\vec{r})$ and $U_2(\vec{r})$ equally interact with the sample (assuming a linear response of the sample), therefore experiencing the same change in amplitude and phase. The field at the detector U_d can be written in terms of an attenuation factor $\alpha_{\tilde{\nu}}/2$ and phase change $\phi_{\tilde{\nu}}$ at wavenumber $\tilde{\nu}$

$$U_d = U' \exp(-\alpha_{\tilde{\nu}}/2 + i\phi_{\tilde{\nu}}) \quad (4.3)$$

The measured intensity $I_{\tilde{\nu}}(\delta)$ for a monochromatic field with wavenumber $\tilde{\nu}$, as a function of path-length difference δ is given by

$$\begin{aligned} I_{\tilde{\nu}}(\delta) &= U_d^* U_d \\ &= \exp(-\alpha_{\tilde{\nu}}) [|U_1|^2 + |U_2|^2 + 2|U_1||U_2| \cos(2\pi\tilde{\nu}\delta)] \end{aligned} \quad (4.4)$$

$$= I_{\tilde{\nu},0} \exp(-\alpha_{\tilde{\nu}}) [1 + \cos(2\pi\tilde{\nu}\delta)] \quad (4.5)$$

where $I_{\tilde{\nu},0} \equiv A_{\tilde{\nu}}^2/2$. Considering now a broadband source, the total intensity at the detector

$I(\delta)$ is found by inserting Eq. 4.5 into Eq. 4.1

$$I(\delta) = \int_0^\infty I_{\tilde{\nu}}(\delta) d\tilde{\nu} \quad (4.6)$$

$$= \int_0^\infty I_{\tilde{\nu},0} \exp(-\alpha_{\tilde{\nu}}) (1 + \cos(2\pi\tilde{\nu}\delta)) d\tilde{\nu} \quad (4.7)$$

$$= \bar{I}_s + \int_0^\infty I_{\tilde{\nu},0} \exp(-\alpha_{\tilde{\nu}}) \cos(2\pi\tilde{\nu}\delta) d\tilde{\nu} \quad (4.8)$$

where the D.C. offset term

$$\bar{I}_s = \int_0^\infty I_{\tilde{\nu},0} \exp(-\alpha_{\tilde{\nu}}) d\tilde{\nu} \quad (4.9)$$

$$= \frac{1}{2} I(\delta = 0) \quad (4.10)$$

is the total intensity that would be recorded without the interferometer in place. However, since the interferogram may not sample exactly at the ZPD, this value may be more accurately found in other ways, such as the mean of the interferogram, or the average limiting value of the interferogram as $\delta \rightarrow \infty$.

Recognizing the integral in Eq. 4.8 as a cosine Fourier transform, a spectrum $I(\tilde{\nu})$ of the coefficients $I_{\tilde{\nu},0} \exp(-\alpha_{\tilde{\nu}})$ may be obtained through Fourier inversion. By sufficiently sampling $I(\delta)$ for a range of δ from the zero-path distance (ZPD) $\delta = 0$ to a maximum δ_{\max} , an intensity spectrum $I(\tilde{\nu})$ is calculated from a discretized version of the cosine Fourier transform:

$$I(\tilde{\nu}) = I_0(\tilde{\nu}) \exp(-\alpha(\tilde{\nu})) \quad (4.11)$$

$$= 4 \int_0^{\delta_{\max}} (I(\delta) - \bar{I}) \cos(2\pi\tilde{\nu}\delta) d\delta \quad (4.12)$$

The factor of four occurs due to the symmetric cosine transform, as only half the integrals in both Eqs. 4.8 and 4.12 are needed. In theory, one only needs to sample on one side of the ZPD, since these transforms are symmetric. In practice, however, both sides of the

ZPD are usually measured and combined in a post-processing step [2]. This comes with the added benefit that the ZPD can be more accurately positioned before computing the inverse transform.

Finally, a transmission spectrum $T(\tilde{\nu}) = I(\tilde{\nu})/I_0(\tilde{\nu}) = \exp(-\alpha(\tilde{\nu}))$ is obtained by dividing out the background measurement. Traditionally, an absorbance spectrum $A(\tilde{\nu}) = -\log_{10}(T)$ is then calculated which, assuming Beer-Lambert law is satisfied, gives

$$A(\tilde{\nu}) = \frac{\alpha(\tilde{\nu})}{\ln(10)} \quad (4.13)$$

As noted earlier, one critical drawback to FTS is the inherent loss of the phase component $\phi_{\tilde{\nu}}$ in Eq. 4.3. However, at the expense of additional data collection (and sacrificing instrument modularity), the foundations of FTS can be extended to retain this phase information.

4.2.2 Fourier-Transform Holographic Spectroscopy

Extending the principles of FTS outlined in Sec. 4.2.1 requires only a few mathematical changes. First, assume that the sample is placed inside the first path (see Fig. 4.2). Then, the field along this path just before recombining with the reference field (along path 2) is modified by the factor $\exp(-\alpha_{\tilde{\nu}}/2 + i\phi_{\tilde{\nu}})$. Therefore, the recombined field from Eq. 4.2 is adjusted as

$$U' = \frac{1}{\sqrt{2}} (U_1 \exp(-\alpha_{\tilde{\nu}}/2 + i\phi_{\tilde{\nu}} + i2\pi\tilde{\nu}\delta) + U_2) \quad (4.14)$$

Since there is no longer a sample between the recombining beamsplitter and the detector, the field at the detector U_d is identical to the recombined U' (up to a phase factor), and the

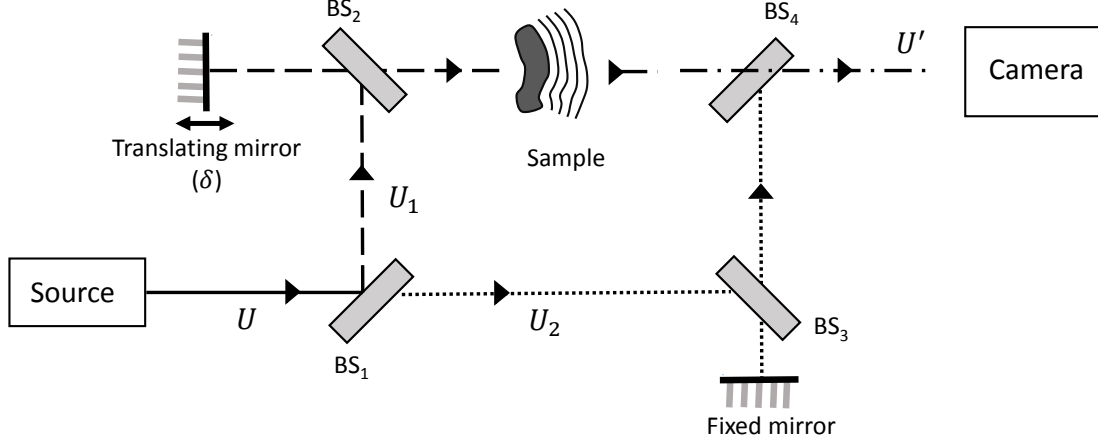


Figure 4.2: Schematic of our modified Mach Zehnder interferometer for performing Fourier-transform holographic spectroscopy. A broadband (temporally incoherent) laser source is split into two paths by the first beamsplitter BS₁. **Along the first path:** the field U_1 reflects off BS₂, reflects from a translating mirror, transmits through BS₂, interacts with the sample, and finally transmits through BS₄ where it is recombined with the second path at the camera. **Along the second path:** the field U_2 reflects off BS₃, reflects from a fixed mirror, transmits through BS₃, and finally reflects off BS₄ where it is recombined with the first path at the camera.

measured intensity $I_{\tilde{\nu}}(\delta)$ for this monochromatic field is given by

$$I_{\tilde{\nu}} = U_d^* U_d \quad (4.15)$$

$$= |U_1|^2 \exp(-\alpha_{\tilde{\nu}}) + |U_2|^2 + 2|U_1||U_2| \exp(-\alpha_{\tilde{\nu}}/2) \cos(2\pi\tilde{\nu}\delta + \phi_{\tilde{\nu}}) \quad (4.16)$$

$$= I_{\tilde{\nu},0} \left[\frac{1}{2} (1 + e^{-\alpha_{\tilde{\nu}}}) + e^{-\alpha_{\tilde{\nu}}/2} \cos(2\pi\tilde{\nu}\delta + \phi_{\tilde{\nu}}) \right] \quad (4.17)$$

Upon integration over all wavelengths, the total recorded intensity $I(\delta)$ at the detector is therefore

$$I(\delta) = \frac{1}{2} (\bar{I}_0 + \bar{I}_s) + \int_0^\infty I_{\tilde{\nu},0} e^{-\alpha_{\tilde{\nu}}/2} \cos(2\pi\tilde{\nu}\delta - \phi_{\tilde{\nu}}) d\tilde{\nu} \quad (4.18)$$

where

$$\bar{I}_0 = \int_0^\infty I_{\tilde{\nu},0} d\tilde{\nu} \quad (4.19)$$

and \bar{I}_s is given in Eq. 4.9. While the form of Eq. 4.18 is very similar to that of Eq. 4.8, there are two important differences.

First, there is an additional D.C. term \bar{I}_0 that enters. This is consistent with the fact that, whereas in FTS both fields U_1 and U_2 interact with the sample, in FTHS only one of the fields interacts with it; the resulting D.C. offset is the average intensity along each of the two paths. Since the additional term \bar{I}_0 is in general greater than \bar{I}_s (the sample will usually absorb or scatter), there results a loss of contrast in the interferogram. In any case, the additional term \bar{I}_0 may be acquired from an additional measurement of the total intensity along the sample arm (where the reference arm is blocked). Alternatively, simply subtracting the mean from the acquired interferogram will remove both D.C. terms.

The second, and more significant difference is the phase term $\phi_{\tilde{\nu}}$ inside of the cosine. This means that the interferogram is no longer a symmetric cosine transform. Using the angle addition identity for cosine, this factor can be rewritten

$$\cos(2\pi\tilde{\nu}\delta - \phi_{\tilde{\nu}}) = \cos(\phi_{\tilde{\nu}}) \cos(2\pi\tilde{\nu}\delta) + \sin(\phi_{\tilde{\nu}}) \sin(2\pi\tilde{\nu}\delta) \quad (4.20)$$

Denoting $I'(\delta) \equiv I(\delta) - (\bar{I}_0 + \bar{I}_s)/2$, the integral in Eq. 4.18 can be expressed as

$$\begin{aligned} I'(\delta) = \int_0^\infty I_{\tilde{\nu},0} e^{-\alpha_{\tilde{\nu}}/2} [\cos(\phi_{\tilde{\nu}}) \cos(2\pi\tilde{\nu}\delta) \\ + \sin(\phi_{\tilde{\nu}}) \sin(2\pi\tilde{\nu}\delta)] d\tilde{\nu} \end{aligned} \quad (4.21)$$

Identifying the integral as a combined sine and cosine Fourier transform, its coefficients are

given by the two inversions

$$I_{\tilde{\nu},0} \exp(-\alpha_{\tilde{\nu}}/2) \cos(\phi_{\tilde{\nu}}) = 2 \int_{-\infty}^{\infty} I'(\delta) \cos(2\pi\tilde{\nu}\delta) d\delta \quad (4.22)$$

$$I_{\tilde{\nu},0} \exp(-\alpha_{\tilde{\nu}}/2) \sin(\phi_{\tilde{\nu}}) = 2 \int_{-\infty}^{\infty} I'(\delta) \sin(2\pi\tilde{\nu}\delta) d\delta \quad (4.23)$$

More compactly, these inversions may be represented as a complex spectrum $\tilde{I}(\tilde{\nu})$

$$\tilde{I}(\tilde{\nu}) \equiv I_{\tilde{\nu},0} \exp(-\alpha(\tilde{\nu})/2) e^{i\phi(\tilde{\nu})} \quad (4.24)$$

Finally, after division by the background measurement, the desired quantities $\exp(-\alpha(\tilde{\nu})/2)$ and $\phi(\tilde{\nu})$ are obtained from the complex spectrum in Eq. 4.24 via

$$\exp(-\alpha(\tilde{\nu})/2) = |\tilde{I}(\tilde{\nu})| \quad (4.25)$$

$$\phi(\tilde{\nu}) = \text{atan2}(\Im(\tilde{I}(\tilde{\nu})), \Re(\tilde{I}(\tilde{\nu}))) \quad (4.26)$$

where the function `atan2` is the two-argument tangent function [155] used to resolve the quotient's sign ambiguity.

It is important to note that the integrals in Eqs. 4.22 and 4.23 must be performed over *both sides* of the ZPD. This is in contrast to traditional FTS, where only one side is sufficient. In other words, from an information standpoint, retrieval of the extra phase information in FTHS requires the collection of *twice* as much data as in FTS. Fortunately, this should not be a concerning drawback, since it is often customary to record both sides of the ZPD anyway.

There is however, one additional subtlety that needs to be mentioned. In traditional FTS, since the interferogram is symmetric about the ZPD, this position is easily determined from the data; shifting errors in the interferogram may be accounted for before Fourier transforming. In FTHS, however, the interferogram is, in general, not symmetric about the ZPD. This means that, at the very least a calibration step must be performed before measurement so that the ZPD location is known. Since a background measurement is required anyway,

the ZPD location may be located from this data—provided that the translating mirror has sufficient repeatability.

4.2.3 General Path Amplitudes

The possibility of imperfect beamsplitters will now be considered. Define the wavenumber-dependent transmission and reflection efficiency of each beamsplitter as $T(\tilde{\nu})$, and $R(\tilde{\nu})$, respectively. Ideally, the ratio $T/R = 1$ and the sum $T + R \leq 1$ is as close to unity as possible. That is, each beamsplitter transmits and reflects 50% of the field's energy. In practice, however, beamsplitters will not perfectly and equally reflect and transmit, nor will any two beamsplitters ever be perfectly equal in quality. The effect of each of these possibilities are therefore considered.

The total field along the two paths U'_1 and U'_2 after the final beamsplitter BS₄ can be expressed in terms of the initial field U just before the first beam-splitter BS₁ (see Fig. 4.2) as

$$U'_1 = t_4 t_2 r_2 r_1 U e^{-\alpha_{\tilde{\nu}}/2 + i\phi_{\tilde{\nu}} + i\delta} \quad (4.27)$$

$$U'_2 = r_4 t_3 r_3 t_1 U \quad (4.28)$$

where $t_i = \sqrt{T_i}$ and $r_i = \sqrt{R_i}$, δ is the free-space optical path difference between the two paths, common phases between the fields are ignored, and the wavenumber-dependency is understood.

First, assume the beamsplitters are each of equal quality. In other words, all beamsplitters possess identical transmission (and reflection) coefficients. In this case, $T_i = T$ and $R_i = R$ (with $i = 1, 2, 3, 4$) for the common transmission and reflection constants T and R (however, in general $T \neq R$). Then, it is obvious from Eqs. 4.27 & 4.28 that both fields experience the

same overall reduction in amplitude

$$U'_1 = \beta^2 A_{\tilde{\nu}} e^{-\alpha_{\tilde{\nu}}/2 + i\phi_{\tilde{\nu}} + i\delta} \quad (4.29)$$

$$U'_2 = \beta^2 A_{\tilde{\nu}} \quad (4.30)$$

where $\beta = \sqrt{TR}$. This results in a simple overall intensity reduction at the detector, and Eq. 4.17 therefore reads

$$I_{\tilde{\nu}} = 4\beta^4 I_{\tilde{\nu},0} \left[\frac{1}{2} (1 + e^{-\alpha_{\tilde{\nu}}}) + e^{-\alpha_{\tilde{\nu}}/2} \cos(2\pi\tilde{\nu}\delta + \phi_{\tilde{\nu}}) \right] \quad (4.31)$$

In this case, after division by a background reference measurement, the $4\beta^4$ quantity cancels and the results obtained in the previous section (Eqs. 4.25 and 4.26) are not changed.

However, if the beamsplitters are close to—but not equal in quality, Eqs. 4.29 and 4.30 need to be modified. Without loss of generality, assume that the attenuation along Path 1 in Eq. 4.27 is still given by β^2 ; since the splitters do not share equal quality, an imperfection term ϵ must manifest along Path 2. Thus,

$$U'_1 = \beta^2 A_{\tilde{\nu}} e^{-\alpha_{\tilde{\nu}}/2 + i\phi_{\tilde{\nu}} + i\delta} \quad (4.32)$$

$$U'_2 = (\beta^2 + \epsilon) A_{\tilde{\nu}} \quad (4.33)$$

and Eq. 4.31 has additional terms

$$I_{\tilde{\nu}} = 4\beta^4 I_{\tilde{\nu},0} \left[\frac{1}{2} \left(1 + \frac{2\epsilon}{\beta^2} + \frac{\epsilon^2}{\beta^4} + e^{-\alpha_{\tilde{\nu}}} \right) + \left(1 + \frac{\epsilon}{\beta^2} \right) e^{-\alpha_{\tilde{\nu}}/2} \cos(2\pi\tilde{\nu}\delta + \phi_{\tilde{\nu}}) \right] \quad (4.34)$$

While the additional terms may change the fringe contrast, they do not affect the results in Sec. 4.2.2. The first group of terms in parenthesis contribute to the interferogram's D.C. value $(\bar{I}_0 + \bar{I}_s)/2$ that is subtracted from $I(\delta)$ before performing the Fourier inversions in Eqs. 4.22 & 4.23. Similarly, the ϵ/β^2 term in the second parenthesis contributes to a scaling

of the cosine that is canceled after dividing out the background measurement.

It has been shown that, mathematically, imperfect beamsplitter transmission and reflection efficiencies do not affect the results of Sec. 4.2.2. However, maximum signal throughput occurs when the beamsplitters have equal transmission and reflection efficiencies (this can be seen by maximizing β^2 subject to the constraint $T + R = 1$). The transmission and reflection's sum and ratio should therefore be as close to unity as possible to maximize the signal and fringe contrast. To illustrate the importance of this, consider the ideal case where $T = R = 1/2$. In the absence of a sample, the average interferogram signal is attenuated by a factor of $\frac{1}{8}$ relative to the source intensity before entering the interferometer. The intensity of the source must therefore be at least eight times greater than what is required by the detection camera for adequate signal-to-noise. Imperfect beamsplitters will therefore increase the source intensity requirement.

4.2.4 Relation to Phase Shifting Holography

It is now shown that FTHS is a broadband generalization of phase-shifting digital holography [98]. Yamaguchi and Zhang introduced the method in 1997 as a solution to remove the zero-order and conjugate phase ambiguity (or, the twin-image). In the case of a monochromatic source (e.g. a single-wavelength laser) of wavenumber $\tilde{\nu}$, the measured interferogram is simply the function $I_{\tilde{\nu}}(\delta)$, and is given by the expression in Eq. 4.16

$$I_{\tilde{\nu}}(\delta) = |U_1|^2 \exp(-\alpha_{\tilde{\nu}}) + |U_2|^2 + 2|U_1||U_2| \exp(-\alpha_{\tilde{\nu}}/2) \cos(2\pi\tilde{\nu}\delta + \phi_{\tilde{\nu}}) \quad (4.35)$$

This has the same form as presented by Yamaguchi and Zhang (Eq. 2 in [98]), where the reference phase ϕ_R in [98] is now represented in Eq. 4.35 by $2\pi\tilde{\nu}\delta$, and $\phi_{\tilde{\nu}}$ is the phase to be recovered (which is $-\phi$ in [98]).

Phase-shifting digital holography requires four¹ measurements to recover the phase. These measurements are performed for the following values of the reference phase $\phi_R = 3\pi/2, \pi/2, 0$, and π . However, since in FTHS an entire interferogram is measured, these phase values occur at the interferogram positions

$$\delta = \frac{3}{4\tilde{\nu}}, \frac{1}{4\tilde{\nu}}, 0, \quad \text{and} \quad \frac{1}{2\tilde{\nu}} \quad (4.36)$$

In this case, where the source is monochromatic, the FTHS interferogram over-determines the phase information. However, in the case of broadband illumination, there is a continuum of $\tilde{\nu}$ and the complete interferogram is required so that all possible sets of δ measurements in Eq. 4.36 are sampled. The Fourier-transform approach in Sec. 4.2.2 relates this spectrum of δ measurements in Eq. 4.36 to the spectrum of phase values $\phi_{\tilde{\nu}}$ to be recovered. In this way, FTHS is a broadband generalization of phase-shifting holography.

4.3 Results

Initial testing of the principles outlined in Sec. 4.2.2 are carried out by constructing a prototype of the modified Mach Zehnder interferometer (as described in Fig. 4.2), using a near infrared (NIR) source and a CCD camera. An areal photograph of the prototype is shown in Fig. 4.3. For this initial test, the prototype is assembled with a few “budget-friendly” items, including the NIR source, collimating lens, and the four beamsplitters. Since these are not commercial grade components, artifacts due to scratches, dust, oils, warping, etc., should be expected. Furthermore, since the NIR source is a battery-powered flash light, its output stability will not be ideal.

The translating stage is driven by a Newport 8310 closed-loop piezo actuator, and images are acquired from a Lumenera INFINITY2-1C CCD camera. The entire assembly is

¹In the original presentation by Yamaguchi and Zhang, four measurements are required to recover phase. This number has since been reduced using various techniques [156–158].

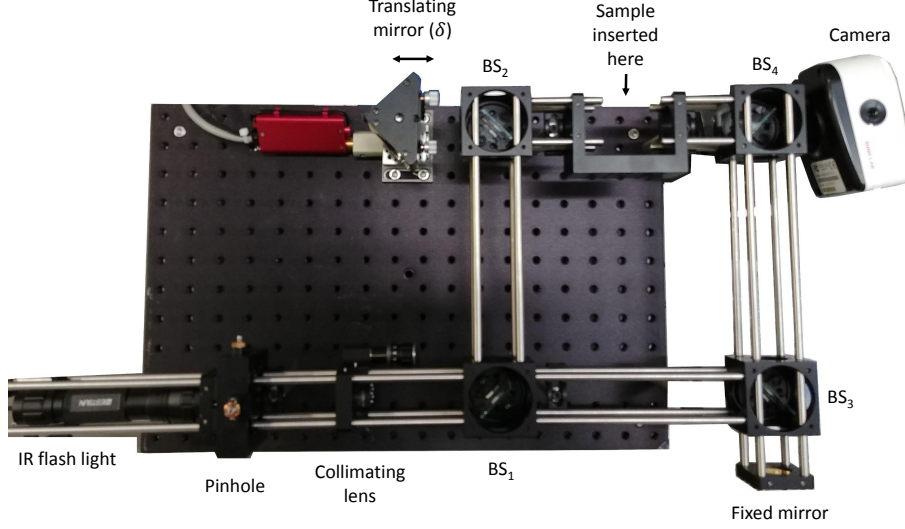


Figure 4.3: Areal photograph of our modified Mach Zehnder interferometer, whose orientation corresponds to the schematic in Fig. 4.2. A near-IR flash light (peak wavelength ≈ 940 nm) is placed against a $25\ \mu\text{m}$ pinhole, and collimated by a 2.54 cm diameter lens whose focal length is 5 cm. (Note: the camera was not properly aligned in this photograph. The detector should be perpendicular to the optical axis—not at the slight angle shown.)

constructed with 30 mm cage components from Thorlabs. For visual aid, system alignment was first performed using a laser diode before installing the NIR source. The NIR flash light is installed flush against a $25\ \mu\text{m}$ diameter pinhole, which is then collimated by a 2.54 cm diameter lens whose focal length is 5 cm. Gold mirrors (Edmund Optics) are chosen due to their improved performance in the infrared.

4.4 Emission Measurement

An emission measurement (without any sample) was performed first. The measured intensity near the estimated zero path-length difference (ZPD) is displayed in Fig. 4.4.

Locating the ZPD is achieved by measuring the variance across the entire image at each stage position. Using the variance helps identify the maximal fringe contrast, which is expected to occur at the ZPD. Figure 4.5 shows the variance as a function of stage position.

An interferogram for the pixel located at $(x, y) = (117, 141)$ from the image in Fig. 4.4 is displayed in Fig. 4.6.

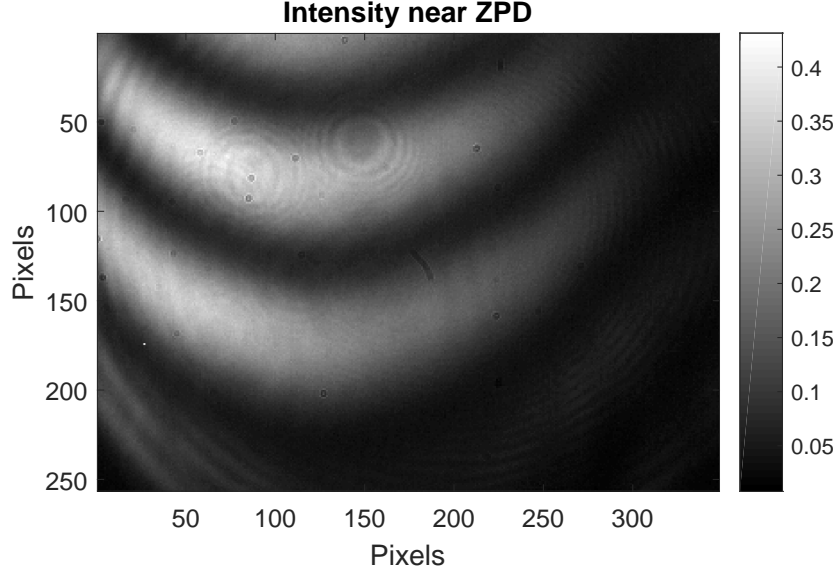


Figure 4.4: Intensity at the approximate ZPD location (see the peak position in Fig. 4.5) shows high contrast fringes due to the constructive (and destructive) interference from the broadband source when the two path-lengths of the MZI are nearly equal.

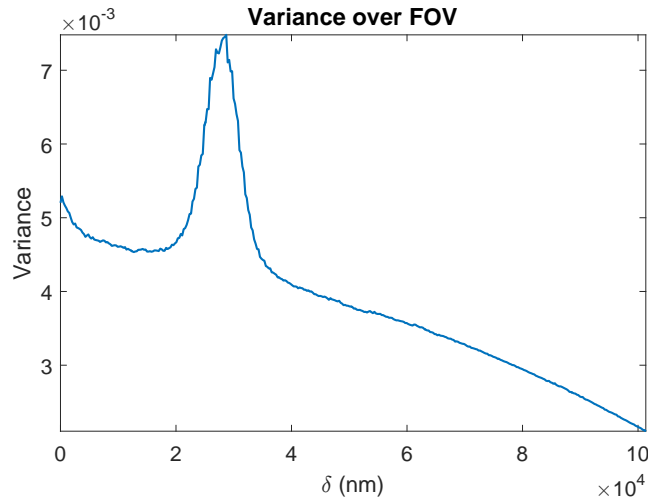


Figure 4.5: The variance over the entire FOV of Fig. 4.4 is maximal when the fringe contrast is greatest, indicating the position of ZPD. The downward sloped baseline is due to the loss of battery power during the hour-long measurement.

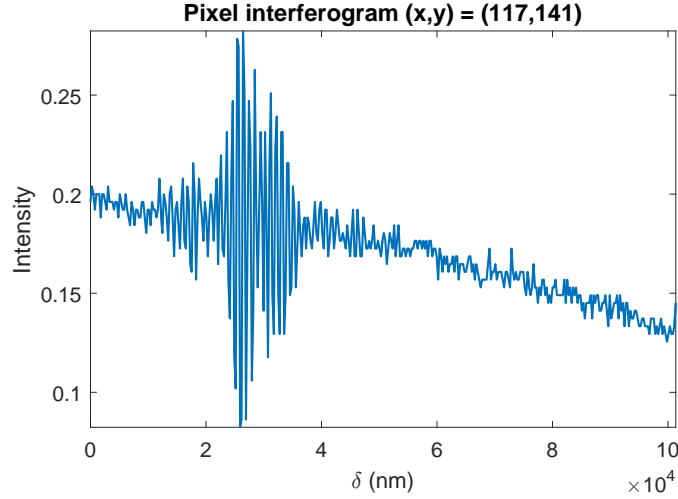


Figure 4.6: An example single-pixel interferogram obtained at the position $(x, y) = (117, 141)$ from the image in Fig. 4.4. The oscillations are greatest in magnitude at the ZPD position since all wavelengths are constructively (or destructively) interfering. Away from ZPD the oscillations approach the constant value $(\bar{I}_0 + \bar{I}_s)/2$ (see Eq. 4.18). The downward sloped baseline is due to the loss of battery power during the hour-long measurement.

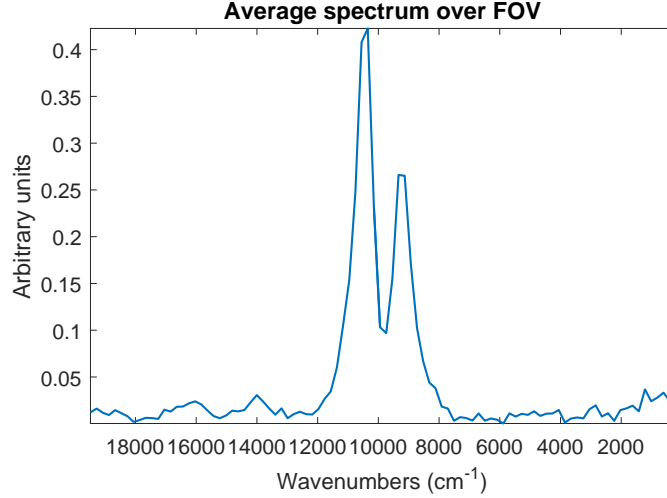


Figure 4.7: The average spectrum (complex magnitude) over the entire FOV of Fig. 4.4 shows that the NIR source is broadband with a central wavenumber near 1060 cm^{-1} , consistent with the source's 940 nm wavelength specification. The spectrum is obtained from the Fourier transform of each pixel's interferogram (e.g., Fig. 4.6) after centering about the ZPD obtained from the variance (Fig. 4.5) and removing a best-fit second-order polynomial baseline to account for the D.C. term $(\bar{I}_0 + \bar{I}_s)/2$ (see Eq. 4.18), as well as the sloped behavior due to the battery's decay. The apparent double peak is likely due to an absorbance from the beam-splitters, which contains a band near that position (see Fig. 4.8).

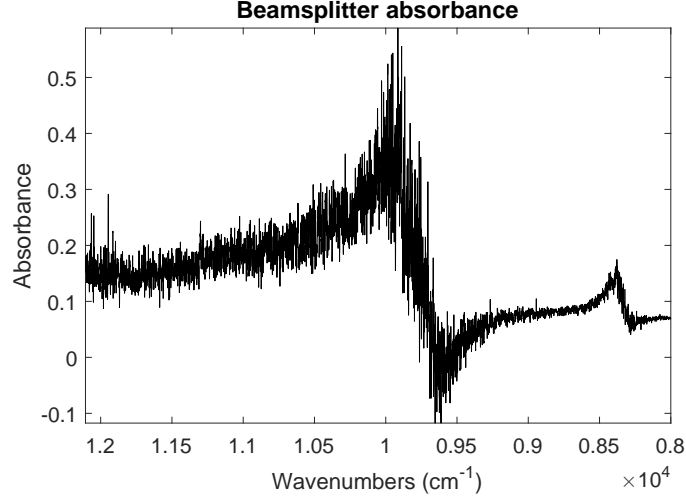


Figure 4.8: Absorbance spectrum of one of the beamsplitters used in the interferometer in Fig. 4.3 shows a strong band near 9950 cm^{-1} , consistent with the wedge observed in the same location of the emission spectrum of the NIR source in Fig. 4.7.

4.5 Micro-Loop Measurement

A MiTeGen micro-loop ($\approx 50\text{ }\mu\text{m}$ diameter) is placed in the sample path, positioned about 7 cm from the camera’s CCD plane. The variance over two regions comparing air and the sample are shown in Fig. 4.10.

Spectra are obtained from the interferograms following the same procedure as in Sec. 4.4. Images of the magnitude and phase at the spectral positions corresponding to the two peaks in Fig. 4.7 are displayed in Fig. 4.11. The phase images are unwrapped using a MATLAB implementation by M. F. Kasim [159], which is based on a technique developed by M. A. Heráez [160]. A large overall slope (along the vertical direction) was removed from the phase images. The slope was estimated from the vertical edge (where contributions from the sample are minimal).

Finally, the spectrum of holograms are back-projected to obtain an in-focus image of the micro-loop. Figure 4.12 shows the results of back-propagating a distance of $z = -7.6\text{ cm}$ (corresponding to the physical distance between the micro-loop and the detector), at the quasi-monochromatic wavelength $\lambda = 1086\text{ nm}$. Back-propagation was performed using modified MATLAB code made available by Latychevskaia and Fink [79], with an assumed

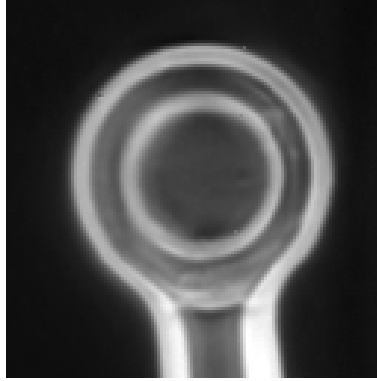


Figure 4.9: A MiTeGen micro loop similar to the one used as a sample in Sec. 4.5. Shown is a mid-infrared absorption measurement, integrated over all wavelengths. The total field of view is $141 \times 141 \mu\text{m}^2$.

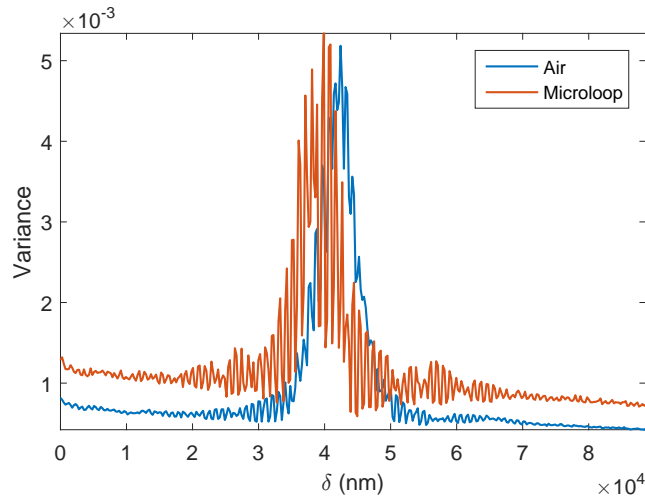


Figure 4.10: The variance over small regions located on the micro-loop, and away from it (labeled Air) shows a negative shift in the ZPD of the micro-loop, expected due to its extended optical path length. This shift is unique to the setup where a sample is placed inside one of the paths, and is not observed in traditional Fourier-transform spectroscopy where the sample is placed outside of a Michaelson interferometer.

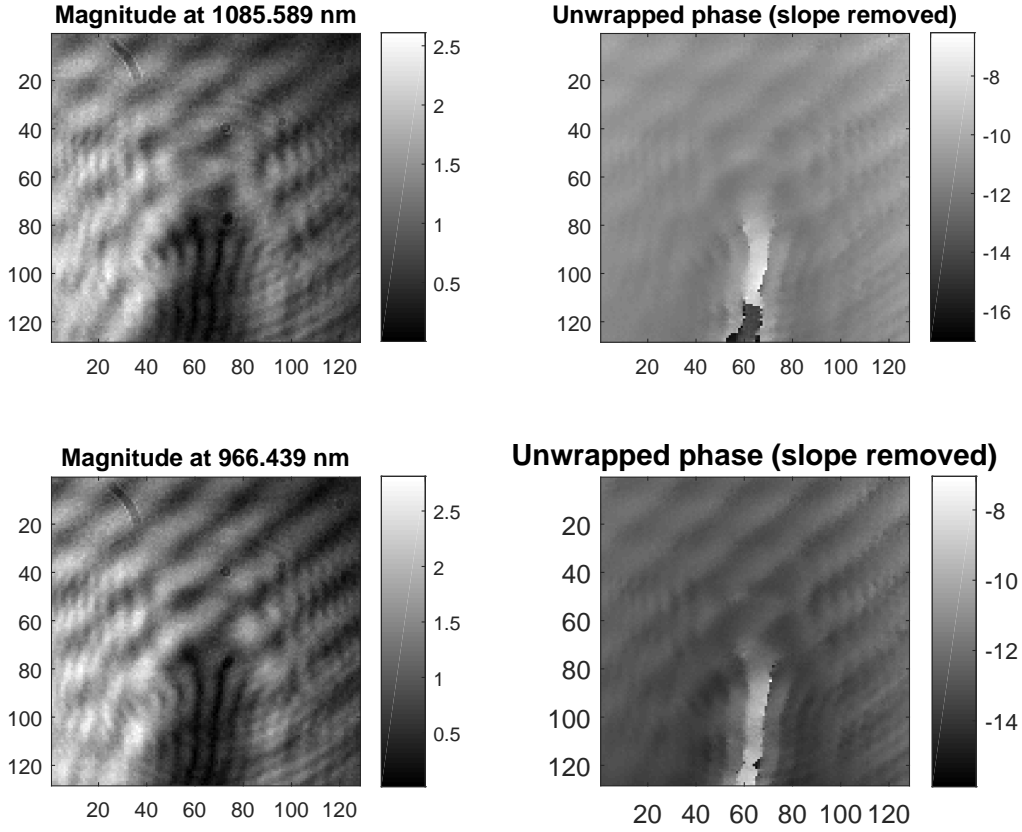


Figure 4.11: Magnitudes and phases at the two peak positions from the emission spectrum in Fig. 4.7. The phase has been unwrapped using [159, 160], and a large overall slope has been subtracted using an estimate obtained along its vertical edge.

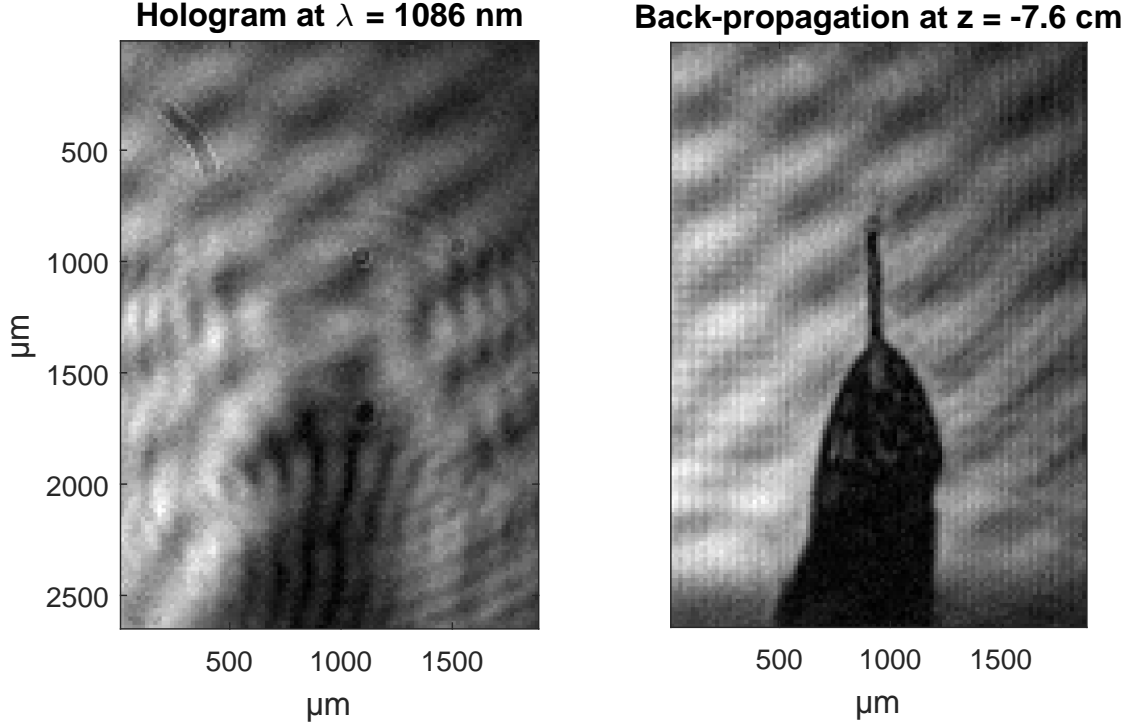


Figure 4.12: Back-propagation results (right) of the hologram (left), using modified MATLAB code made available by Latychevskaia and Fink [79] with an assumed plane wave model. Shown are magnitude images.

plane wave model. The back-propagation distance z was determined by stepping through a stack of images and visually identifying the slice that is most in-focus. The hologram's physical dimensions (referred to as the side-area in [79]) are determined from the camera's specifications: a single pixel has an area of $4.65 \mu\text{m} \times 4.65 \mu\text{m}$; with 4×4 binning, each pixel is approximately $18.6 \mu\text{m} \times 18.6 \mu\text{m}$.

4.6 Discussion

The presence of fringes in the intensity image near ZPD (fig. 4.4) suggests that alignment is not ideal. This may be due to incorrect collimation, or beams converging slightly off-axis, or a combination of both of these effects. Since the NIR flash light was manually filtered

and collimated, it is likely that the wavefront suffers from a degree of curvature, and cannot be considered an ideal plane wave. The SCL and QCL, however, are much closer to ideal Gaussian, collimated beams. Thus, we anticipate that alignment with these sources may be slightly easier, in that the occurrence of fringes will likely be solely due to off-axis alignment rather than poor collimation. There were, however, back-reflections and multiple internal reflections from the beam splitters and other components, that were unexpectedly more prominent than we had hoped. These artifacts were mitigated by placing 5 μm diameter apertures just before BS₂ and BS₃, and a 3 μm diameter aperture just before BS₁.

The second interesting feature to note is the downward slope of the variance and interferogram (Figs. 4.5 and 4.6), which is likely due to the battery losing output power. To correct for this effect, a quadratic baseline is fit and subtracted from each pixel's interferogram. Then, each pixel's interferogram is centered about the estimated position obtained from the peak in the variance (Fig. 4.5), and Fourier transformed to obtain the spectrum in Fig. 4.7. In MATLAB, this requires two `fftshift` operations: one before, and one following the FFT operation. The first half of the resulting FFT spectrum (negative frequencies) are then discarded.

The resulting spectrum appears to contain two peaks: one at 1045 cm^{-1} , while the other at 9234 cm^{-1} , corresponding to wavelengths 957 nm and 1083 nm, respectively. However, measurements of the NIR source using our commercial FTIR microscope shows only one peak at ≈ 940 nm; measurements of the beamsplitter with the FTIR microscope (Fig. 4.8) shows a band at approximately 9750 cm^{-1} . Therefore, it is likely that the appearance of two peaks in the spectrum is actually due to an absorption (or reflection) band from the beamsplitters in our prototype that splits the NIR emission band into two.

The results of the air measurement show consistency with a typical Michaelson interferometer; however, to demonstrate the difference between FTS and FTHS, a sample must be placed along one of the paths. A MiTeGen micro loop is placed along the path indicated in Fig. 4.3, about 7 cm out of focus from the imaging CCD plane. Imaging optics were

not used since it was important to demonstrate that indeed diffraction features could be obtained from a broadband source, and that back-propagation without the twin image could be achieved.

The first notable difference between FTS and FTHS is the expected shift in ZPD when a sample is inserted. Without any dispersion, the shift would simply be equal to the product of the sample's refractive index and optical thickness [56]. The variance in Fig. 4.10 shows a shift in the ZPD, consistent with this expected behavior.

A per-pixel spectrum is obtained from its interferogram using the same method as the emission measurement. A ZPD is estimated from the variance in a region away from the micro loop, and the resulting images at the two spectral positions corresponding to the two peaks in Fig. 4.7 are displayed in Fig. 4.11. Due to likely off-axis alignment, the phase images contained a large vertical slope, which has been removed. However, there remains a diagonal fringing effect, which may be due to multiple internal reflections from the non-commercial-grade beamsplitters, or vibrational interference noise.

Finally, the ability to refocus an image of the micro-loop from the hologram is shown in Fig. 4.12. From the intensity image in Fig. 4.4, it is apparent that the NIR source was not perfectly collimated, as spherical interference effects are present. Nevertheless, a collimated plane-wave was assumed, and back-propagation was performed using this model [79]. Spherical scaling aberrations must be expected when there are significant deviations from this plane-wave model. However, the plane-wave approximation appears to work very well for this dataset. The significant feature to note is that, since it is the broadband generalization of phase-shifting holography (see Sec. 4.2.4), the out-of-focus twin image does not present in the refocused image. This provides a benefit over off-axis holography, as it allows the full resolution of the detector to be utilized, whereas in off-axis holography the resolution is limited by the carrier frequency determined by the interference angle [161].

4.7 Conclusions

We have demonstrated a method for obtaining spatially- and spectrally-resolved amplitude and phase information by extending classical Fourier-transform spectroscopy with a Michaelson interferometer to Fourier-transform holographic spectroscopy using a Mach Zehnder interferometer. With this method, the phase is extracted from an in-line (or, Gabor-like) setup, without the zero-order and conjugate image ambiguity. This has been shown to be a generalized version of phase-shifting holography to the case of broadband illumination [98]. An additional benefit over monochromatic sources is the inherent group phase unwrapping that may be extracted from the shift in the zero-pathlength difference (ZPD) peak.

The additional phase information in mid-infrared microspectroscopy may help improve scatter correction and three-dimensional hyperspectroscopy. Additionally, it inherently provides the benefits of quantitative phase imaging (QPI), allowing both spectral and quantitative phase information to be obtained simultaneously. For instance, combining traditional FTIR spectroscopic pathology techniques [3, 7, 39, 90–93] with QPI [61, 63, 64] may provide powerful new analysis capabilities for histopathology without requiring correlation between multiple microscope instruments.

Unfortunately, mid-IR laser and FPA technology has a way to go before holographic FTIR can replace traditional FTIR. Full coverage of the mid-infrared spectrum is not possible without combining multiple lasers and detectors, which is not a practical or compact solution. At present, the combination of a broadband supercontinuum laser source (Thorlabs), along with a tunable quantum cascade laser (Daylight Solutions), allows coverage over two very important mid-infrared regions of approximately $3300\text{--}2600\text{ cm}^{-1}$, and $1333\text{--}900\text{ cm}^{-1}$, respectively. These regions are crucial for many infrared spectroscopic applications, as they include important chemical bands such as C-H, O-H, N-H, and the so-called fingerprint region [1]. Alternatively, spatially incoherent mid-infrared sources such as the Thorlabs SLS203L may be used with a spatial filter to increase its coherence, at the cost of lower signal-to-noise. However, mid-infrared broadband laser technology has been developing rapidly over the past

few years [94, 95, 162, 163]; full mid-IR coverage may soon be available, and the plethora of diffraction and holographic techniques [85] that have been utilized over the decades in optical, x-ray, acoustics, and electron microscopy, may finally be used to enhance FTIR microspectroscopy. The FTHS method presented here is a first step to a full realization of such phase imaging techniques for mid-infrared spectroscopy.

Chapter 5

Lessons Learned for Extending IR Microscopic Techniques

5.1 Infrared Diffraction Tomography

5.1.1 Introduction

In 2013, a novel realization of three-dimensional hyperspectral infrared imaging using computed tomography (CT) was demonstrated by Martin et al [37]. Three-dimensional voxelated spectra are capable of revealing distinct chemical depth layers that would otherwise be mixed together. For instance, these methods have been applied by Luca Quaroni, et. al., who report subcellular resolution by discerning nuclei and vacuole from their cellular wall [38]. Their results offer an alternative approach for distinguishing distinct spectra from components within cells without complimentary methods such as fluorescence staining [39], or the need to grow cells in a controlled process [40]. Tomographic FTIR has also been important in cases where non-destructive chemical analysis is required, such as in the investigation of a meteorite grain [41].

Unfortunately, however, a major limitation faced when adopting CT to microscopic samples in the infrared has been due to the effect of scatter. Whereas in classical x-ray CT the

refractive index (RI) is close to unity for tissues [52], the average RI for biological materials in the infrared region may be on the order of 1.3 to 1.6 [53, 54]. Furthermore, since we are measuring samples whose extent (or features of interest) are on the order of the radiation wavelength, geometrical ray-optics is an insufficient approximation [55]. Therefore, refraction and multiple scattering effects such as fringes and shape resonances must be expected for all but the smallest of samples whose dimensions do not exceed by very much the radiation wavelength [56]. A more accurate model of the physical situation should also account for the wave nature of the optical system. Diffraction tomography (DT), for example, is a well-established method for wave-like systems such as acoustics and optics [29, 42].

Standard DT algorithms make use of either the Born, or Rytov approximation [29]. While each are appropriate in slightly different contexts, both assume that the refractive index is very small (the theory begins breaking down when it exceeds roughly 10% of the background medium [42]), limiting the theory’s applicability. The relatively large RI for typical biological samples in the mid-infrared means that weakly scattering approximations such as Born and Rytov for three-dimensional imaging may lead to severe reconstruction artifacts. Experimentally, one can use refractive index matching to reduce the scattered field strength. However, in mid-infrared measurements, embedded mediums are often difficult to make, or come at the cost of reduced spectral coverage (e.g., in the case of aqueous solutions, mid-infrared spectra are dominated by very strong H₂O bands), or even changing the chemical signature [1, 7]. Alternatively, model based methods may be used to remove the strong scatter signatures [109–114]. However, due to the large amount of data in three-dimensional hyperspectral imaging (there may be $\sim 10^3$ per-wavelength volumetric reconstructions required), a computationally efficient method is desirable. While Soubies et al achieved efficient reconstructions, their peak performance is still on the order of 10 minutes per wavelength on a higher-end server (Dell PowerEdge T430) [111]. Even with only a hundred or so wavenumbers, this amounts to about a day of computation time. Therefore, approximations that sufficiently capture the physics of biological scattering in the infrared without neglecting

multiple scattering and diffraction effects is desired.

Here, a spectral-based approach is presented, which exploits the assumption that weak absorbance features (typical for biological media in the infrared regime) sit atop a relatively constant refractive index. Further work including simulations (or preferably experimental data) is necessary to test the validity of these assumptions.

5.1.2 Methods

Consider an object with a spatially-dependent complex refractive index $n(\vec{r}, k)$, where $\vec{r} = (x, y, z)$ is the position vector, and $k = 2\pi/\lambda$ is the free-space wavenumber (with wavelength λ). The relative complex permittivity is $\epsilon(\vec{r}, k) = n(\vec{r}, k)^2$. Assuming a scalar wave treatment with a linear dielectric medium, the wave equation relates the (scalar) electric field $u(\vec{r}, k)$ and the object's permittivity via

$$(\nabla^2 + k^2)u(\vec{r}, k) = -k^2[\epsilon(\vec{r}, k) - 1]u(\vec{r}, k) \quad (5.1)$$

Classical Born approximation

In the Born and Rytov approximations, the field is broken into two terms: an incident u_0 and scattered u_s field

$$u(\vec{r}, k) = u_0(\vec{r}, k) + u_s(\vec{r}, k), \quad (5.2)$$

where u_0 solves the homogeneous free-space equation

$$(\nabla^2 + k^2)u_0(\vec{r}, k) = 0 \quad (5.3)$$

A general solution (also referred to as the Lippmann-Schwinger equation) to Eq. 5.1 in three dimensions is given in terms of the Green function $g(R, k) = \frac{\exp(ikR)}{4\pi R}$

$$u(\vec{r}, k) = u_0(\vec{r}, k) + k^2 \int_{\Omega} g(R, k) [\epsilon(\vec{r}', k) - 1] u(\vec{r}', k) d^3 r' \quad (5.4)$$

where $R = |\vec{r} - \vec{r}'|$ and the integral is performed over the object Ω .

The Born solution $u_s(\vec{r}, k) \approx u_B(\vec{r}, k)$ to this integral assumes that the scattered field is much weaker than the incident field, so that Eq. 5.4 can be approximated as

$$u_B(\vec{r}, k) = k^2 \int_{\Omega} g(R, k) [\epsilon(\vec{r}', k) - 1] u_0(\vec{r}', k) d^3 r' \quad (5.5)$$

Unfortunately, the Born approximation, which assumes a weak scattered field u_s , is invalid over many of the useful shorter wavelengths for typical biological media in the infrared, where one typically encounters refractive indices $n \gtrsim 1.3$ [137]. In particular, it is required that the relative phase difference between the scattered and incident field is less than π [29]. As an example, consider a slab of thickness $h = 7 \mu\text{m}$ -thick slab (or, a sphere of radius $a = 3.5 \mu\text{m}$), where the average real refractive index $n_r = 1.5$. The relative phase difference $\Delta\phi$ in the forward direction is [10]

$$\Delta\phi = 2\pi(n_r - 1)h\tilde{\nu} \quad (5.6)$$

As $\Delta\phi$ must be bounded by π ,

$$\pi > 2\pi(n_r - 1)h\tilde{\nu} \quad (5.7)$$

$$\Rightarrow \tilde{\nu} < \frac{1}{2(n_r - 1)h}, \quad (5.8)$$

which, for the example presented, requires that $\tilde{\nu} < 1429 \text{ cm}^{-1}$. This restriction of the Born approximation means that important spectral information above 1429 cannot be accurately

recovered using this method.

Spectral-Based approach

In the following approach, four key assumptions or approximations will be made, based on physical properties of typical biological media in the mid-infrared:

1. A fluctuating real and imaginary permittivity (who are Kramer-Kronig transform pairs), are superimposed on a real and spectrally-constant permittivity;
2. The fluctuating real and imaginary components of the permittivity are small, such that the Born approximation would be valid if only the imaginary component of ϵ were present;
3. The chemical (or spectral) signature of the scattering object does not vary appreciably over its volume;
4. Spectral fluctuations of the electric field internal to the sample are broad relative to absorbance features.

The first and second of these assumptions allows one to express the electric susceptibility $\chi(\vec{r}, k)$ (hereafter referred to as the object potential) as

$$\chi(\vec{r}, k) \equiv \epsilon(\vec{r}, k) - 1 \quad (5.9)$$

$$\approx \Delta(\vec{r}) + \hat{\epsilon}_i(\vec{r}, k) + i\epsilon_i(\vec{r}, k) \quad (5.10)$$

where $\Delta(\vec{r}, k) = \epsilon_0(\vec{r}) - 1$ for a spectrally constant real permittivity $\epsilon_0(\vec{r})$, and $\hat{\epsilon}_i(\vec{r}, k) = \text{KK}[\epsilon_i(\vec{r}, k)]$ is the Kramer-Kronig transformation [10, 138]. While the Born approximation solves for very small Δ , here it may be larger; our ultimate interest will be in the imaginary component ϵ_i , which gives the absorbance features.

The third assumption listed above suggests that we can express the potential everywhere inside the sample as a perturbation

$$\chi(\vec{r}, k) = \chi^{(0)}(\vec{r}, k) + \chi^{(1)}(\vec{r}, k) \quad (5.11)$$

The purpose of the perturbation in Eq. 5.11 can be made explicit if one introduces an *object mask function* $\Phi(\vec{r})$ that is unit valued everywhere interior to the sample, and zero elsewhere.

This permits the following form

$$\chi(\vec{r}, k) = (\chi^{(0)}(k) + \chi^{(1)}(\vec{r}, k)) \Phi(\vec{r}), \quad (5.12)$$

from which it is clear that we are considering the material to be composed of a single spectrum, with small spatial variations. The motivation for this perturbation comes from the observation that measurements of biological media tend to have very similar spectra, with very small changes that are often subtle enough to go undetected without statistical processing [4].

With these first three assumptions, the scattered field can be expressed as a perturbation

$$u_s(\vec{r}, k) = u_s^{(0)} + u_s^{(1)} \quad (5.13)$$

where the two terms are given by

$$u_s^{(0)} = k^2 \chi^{(0)}(k) \int_{\Omega} g(R, k) \Phi(\vec{r}') u(\vec{r}', k) d^3 r' \quad (5.14)$$

$$u_s^{(1)} = k^2 \int_{\Omega} g(R, k) \Phi(\vec{r}') \chi^{(1)}(\vec{r}', k) u(\vec{r}', k) d^3 r' \quad (5.15)$$

Finally, the fourth assumption listed above allows one to perform a local expansion of the internal field about a spectral position k_0 . Of interest is an expansion of the scattered

field

$$u_s(\vec{r}, k) = u_s(\vec{r}, k_0) + (k - k_0) \left. \frac{\partial u_s(\vec{r})}{\partial k} \right|_{k_0} + \dots \quad (5.16)$$

The usefulness of this expansion will be made apparent in Section 5.1.2.

Fourier Transform of Zero-Order Equation

Using the Weyl expansion, the Green function $g(R, k)$ can be expressed as [42]

$$g(R, k) = \frac{-i}{2(2\pi)^2} \int_{-\infty}^{\infty} \frac{\exp\left(i\vec{K}_\rho \cdot \vec{R}_\rho + i\gamma z\right)}{\gamma} d^2 K_\rho \quad (5.17)$$

where $\vec{R}_\rho = (x, y)$ and $\vec{K}_\rho = (K_x, K_y)$ are two-dimensional vectors perpendicular to the z - and K_z -axes, and $\gamma^2 = k^2 - |K_\rho|^2 \geq 0$. Substituting Eq. 5.17 into Eq. 5.14 and rearranging terms in the exponentials, the zero-order scattered field becomes

$$u_s^{(0)} = k^2 \chi^{(0)}(k) \int_{\Omega} \int_{-\infty}^{\infty} \left[\frac{-i}{2(2\pi)^2} \right] e^{i\vec{K}_\rho \cdot \vec{r}_\rho + i\gamma z} \frac{1}{\gamma} \Phi(\vec{r}') [1 + u'_s(\vec{r}', k)] e^{-i\vec{K}_\rho \cdot \vec{r}' - i(\gamma - k)z'} d^2 K_\rho d^3 r' \quad (5.18)$$

where the field has been written $u = \exp(ikz) [1 + u'_s]$, with $u'_s = \exp(-ikz)u_s$. Changing orders of integration, and identifying the right-most exponential as performing a three-dimensional Fourier transform over \vec{r}' , the zero-order scattered field is

$$u_s^{(0)} = \frac{-ik^2}{2} \chi^{(0)}(k) \int_{-\infty}^{\infty} \left[\frac{1}{(2\pi)^2} \right] e^{i\vec{K}_\rho \cdot \vec{r}_\rho + i\gamma z} \frac{1}{\gamma} \mathcal{F} \{ \Phi(\vec{r}) [1 + u'_s(\vec{r}, k)] \} (\vec{K}_\rho, K_z = \gamma - k) d^2 K_\rho \quad (5.19)$$

Recognizing the factor in brackets and exponential as performing an inverse Fourier transform about K_ρ , the forward Fourier transform of the scattered field is therefore

$$\mathcal{F} \{u_s^{(0)}\} (\vec{K}_\rho) = \frac{-ik^2}{2} \chi^{(0)}(k) \frac{e^{i\gamma z}}{\gamma} \mathcal{F} \{\Phi(\vec{r})[1 + u'_s(\vec{r}, k)]\} (\vec{K}_\rho, K_z = \gamma - k) \quad (5.20)$$

Finally, the fourth assumption listed earlier allows one to expand the scattered field u'_s about the spectral position k_0 . In particular, if one places a windowing function $\psi_{a,k_0}(k)$ (defined by its width a and position k_0) in spectral space, one may consider a finite number of series terms, and Eq. 5.20 becomes

$$\begin{aligned} \psi_{a,k_0}(k) \mathcal{F} \{u_s^{(0)}\} (\vec{K}_\rho) = \\ \psi_{a,k_0}(k) \frac{-ik^2 \chi^{(0)}(k)}{2\gamma} e^{i\gamma z} \mathcal{F} \left\{ \Phi(\vec{r}) [1 + u'_s(\vec{r}, k_0) + (k - k_0) \left. \frac{\partial u'_s(\vec{r})}{\partial k} \right|_{k_0} + \dots] \right\} \end{aligned} \quad (5.21)$$

The details of the windowing function ψ_{a,k_0} will depend on the data. Examples of windows include (but are not limited to) boxcar, Gaussian, sine, and Hann [164–166]. The choice of windowing filter may be impacted by the required modeling fidelity; larger window sizes may be tolerable when modeling spectral information where multiple-scatter effects vary slowly as a function of wavenumber, and can be modeled as a polynomial of small degree. At this point, the requirement is that ψ_{a,k_0} has compact support, large enough to capture the behavior of $\chi^{(0)}(k)$, while small enough that the expansion is accurate.

In this form, for discrete samples of the field on a detector plane, a linear system of equations are formed in terms of $\chi^{(0)}$ at various positions of k_0 .

There are a few ways to proceed, depending on results from simulations and experimental data. The leading method to be explored is to assume that a reference spectrum (e.g. Matrigel [19]) is provided and accurately approximates $\chi^{(0)}$. However, this requires an approximation of the real constant refractive index, which might be tricky for certain materials.

Another method is to view Eq. 5.21 as a system of linear equations of the unknown quantities $\chi^{(0)}(k)$, $u'_s(k_0)$, $\partial u'_s/\partial k|_{k_0}$, etc. Numerically, since the window selects a small subset of spectral data points, it is likely that there will be orders of magnitude more available spectra than there are their sampling points. As an example, consider a windowing function that samples 128 spectral points in a region about k_0 . If one measures the field on a 128×128 grid, there will be $\mathcal{O}(10^2)$ more spectra available, making Eq. 5.21 overdetermined in solving for $\chi^{(0)}$ and the field series terms.

A hybrid approach may take into account a combination of these two methods. For example, using a reference spectrum and its Kramer's-Kronig transform, and solving for Δ and the field expansion terms. Another possible method is combining with an established model-based approach [109–114].

The first of these methods will be discussed in more detail. This assumes that a reference spectrum suffices in solving for the series terms in Eq. 5.21.

Field Measurement via Fourier-Transform Holographic Spectroscopy

The response of most imaging devices is to field intensity, and therefore obtaining the scattered field u_s requires a measurement of the phase. Holography and its many variants [56] are often used for the purpose of converting phase information into intensity variations. Here, the field measured is assumed to have been measured with Fourier-Transform Holographic Spectroscopy (FTHS) (see Chapter 4). In the absence of significant dispersion, the unwrapped phase shift is estimated from the shift in the zero-path difference (ZPD) of the collected FTHS interferograms. Furthermore, since FTHS uses a Mach Zehnder interferometer, the resulting interference and measured phase may only be obtained in terms of the path-length *difference*; that is, any absolute phase (e.g., $\exp(ikz)$) carried by the field that is common between the two Mach Zehnder paths is lost at the detector.

Assuming a collimated source beam that has a uniform phase and can be approximated as a plane wave, and also that the phase $\exp(ikz)$ is common to all field terms, the field mea-

sured in FTHS after division by a background (or reference) measurement can be modified from Eq. 5.4 to read

$$u(\vec{r}, k) = 1 + k^2 \int_{\Omega} g(R, k) \chi(\vec{r}', k) [1 + u'(\vec{r}', k)] d^3 r' \quad (5.22)$$

Where $u'_s = \exp(-ikz)u_s$ as it was used in arriving at Eq. 5.18. Subtracting one from Eq. 5.22, the scattered field u_s obtained in FTHS is

$$u_s(\vec{r}, k) = k^2 \int_{\Omega} g(R, k) \chi(\vec{r}', k) [1 + u'(\vec{r}', k)] d^3 r' \quad (5.23)$$

Proposed Algorithm

1. Data collection with FTHS. Assumed to have measured the scattered field u_s (e.g., Eq. 5.23).
2. Calculate 2-D Fourier transform of scattered field $\mathcal{F}\{u_s\}(K_x, K_y)$.
3. Possible normalization (e.g., multiplying by γ)
4. Use window function at position k_0 , calculate values of the field term series using least-squares fitting, with a provided reference spectrum $\chi^{(0)}$ (e.g. Matrigel).
5. Slide window by a single spectral data point, repeat Step 4 until all spectral points are covered.

5.1.3 Conclusions

Four key assumptions about the scattering behavior for typical biological samples in the infrared were presented in Sec. 5.1.2. An algorithm based on these assumptions was presented in Sec. 5.1.2; however, an evaluation of this algorithm requires hyperspectral phase and amplitude measurements. While these may be obtained using the Fourier-transform holographic spectroscopy approach presented in Chapter 4, such data are not available at

this time. Depending on the data collected, the fourth assumption (which requires that spectral fluctuations of the electric field internal to the sample are broad relative to absorbance features) may not hold in practice. In this case, a different approach that utilizes the other three assumptions may be required. For instance, the methods presented here may be combined with digital confocal spectroscopy (Sec. 5.2), three-dimensional quantitative phase imaging techniques [62], or three-dimensional ptychographic transmission microscopy [123, 124].

5.2 Digital Confocal IR Spectroscopy

Probing chemical information within a sample’s interior has recently been possible using tomographic methods that allow for the acquisition of three-dimensional volumes of spectra [37]. FTIR tomography has its limitations however, as the majority of samples of interest are planar in extent, and are thus highly absorbing at extreme angles.

Alternative methods for three-dimensional imaging include confocal microscopy, which operates by blocking out-of-focus light with an aperture, effectively illuminating a small voxel of interest. A series of measurements for each voxel can therefore produce a three-dimensional representation of the sample. Attempts to perform confocal microscopy in infrared have produced promising results [167, 168], though a bright synchrotron source and raster scanning along each dimension is required for full three-dimensional hyperspectral imaging.

We present a method for performing confocal microscopy digitally, using a series of z -axis projection images whose out-of-focus pixels are filtered from the volume using an algorithm inspired by convolutional neural networks. Since the reconstruction is performed digitally, our method does not require the use of any specialized hardware (e.g. lasers, apertures, etc.), and operates using a typical transmission Fourier-transform infrared microscope with an imaging focal plane array (FPA).

5.2.1 Introduction

Recently, a novel realization of three-dimensional hyperspectral infrared imaging using computed tomography (CT) has been demonstrated [37]. Three-dimensional voxelated spectra are capable of revealing distinct chemical depth layers that would otherwise be mixed together. For instance, these methods have been applied by Luca Quaroni, et. al., who report subcellular resolution by discerning nuclei and vacuole from their cellular wall [38]. Their results offer an alternative approach for distinguishing distinct spectra from components within cells without complimentary methods such as fluorescence staining [39], or the need to grow cells in a controlled process [40]. Tomographic FTIR has also been important in cases where non-destructive chemical analysis is required, such as in the investigation of a meteorite grain [41].

Despite its limitations (see Ch. 1, Secs. 1.2 and 1.3), results from this work have been very promising [37] and have motivated our investigation into alternative three-dimensional spectral imaging techniques that can account for a larger class of samples. First, scattering effects limit the quality of CT reconstructions; methods such as diffraction tomography using holography may be more suitable for three-dimensional infrared microspectroscopy, where the wave nature of the system is taken into account (Ch. 4 & 5, Sec. 5.1). The second limitation imposed by tomography is the restriction to samples with cylindrically-bounded extent. This restriction comes from the requirement of projection measurements acquired over 360° about the sample's principal rotational axis [29]. This imposes an upper limit on the radial extent of the sample (usually no more than about $40\text{ }\mu\text{m}$), due to both the high absorptivity as well as non-negligible deviations from the idealized parallel beam model used to perform the reconstructions. As many biological films such as cryotome-sliced tissues are planar (with a lateral extent that may be on the order of centimeters), the quality of CT reconstructions on these type of samples will suffer due to the restricted range of measurement angles.

Accounting for samples with planar extent is possible using limited-angle tomography

methods such as tomosynthesis and laminography. For instance, advances in digital breast tomosynthesis, which are desired for improved diagnosis with minimal radiation exposure to the subject, have been made by optimizing geometry and algorithms [49, 50]. Similarly, laminography methods have shown that missing wedge artifacts may be reduced with monochromatic radiation and proper parallel-beam (or plane-wave) geometry, as opposed to focused (cone-beam) illumination [51]. Other methods used to image in three dimensions include confocal microscopy, where out-of-focus scattered light is blocked using pinholes.

Confocal microscopy

Confocal microscopy is an optical sectioning technique patented by Marvin Minsky in 1961 [169], which uses a pinhole to select only light that scatters from a small localized region of a sample. Many variants of the technique have been developed, including raster laser scanning, pinhole and slit arrays (which improve the rate of data collection), and multi-photon fluorescence confocal imaging [170, 171]. Central to each of these techniques, however, is the use of a pinhole to eliminate out-of-focus light, leaving only the intensity of light originating from a small three-dimensional point in a sample.

Confocal FTIR microscopy has been successfully demonstrated using a synchrotron radiation source, an infinity-corrected lens (to collimate the beam), and a single-pixel MCT detector [167]. While the results are promising, the specific hardware requirements are often not practical. With a typical global infrared source, the intensity is hundreds to thousands of times weaker than that of a synchrotron source, and not enough photons can make it through the pinhole to the detector in any reasonable amount of time. Even with a synchrotron source, the process of obtaining a complete three-dimensional volume of spectra would be tedious, and therefore likely have very low resolution.

In any confocal measurement, a certain amount of “bleeding” will occur, with some out-of-focus light making it through the finite-sized pinhole [170]. Data can be cleaned to partially recover some of this lost resolution by deconvolving the data with a three-dimensional point-

spread function (PSF) [120, 121]. A three-dimensional deconvolution approach applied to a volume of images acquired by stepping through the focal axis is discussed and evaluated first. While the deconvolutional method removed a portion of the out-of-focus light, it did not succeed in producing quality optical sectioning.

We present here a method for performing digital optical sectioning without confocal hardware. The algorithm works by exploiting the fact that, as one steps through images acquired at different focal depths, various features within the sample come in- and out-of-focus. By measuring the “degree of focus,” the algorithm retains regions of maximal focus, while discarding the out-of-focus portions. Similar methods have been developed that, for example, estimate depth from focus [116, 117], or simulating infinite depth of focus in typical bright-field measurements [118, 119]. However, these techniques are optimized for surface reconstructions; transparent media, which are usually the subject of FTIR spectroscopy, requires a different treatment. Presented is an approach that is inspired by convolutional neural networks (CNNs), which are often used in object recognition and classification [115]. The methods are evaluated on both a bright-field dataset, and an infrared measurement.

5.2.2 Methods

Background

A small pinhole placed in the focal plane of an optical system produces what is known as a point spread function (PSF). Figure 5.1 (left) shows the PSF of a 2 μm pinhole at the focal plane. While a single pixel of the image maps an area of about 1.1 μm , the light produced by the 2 μm pinhole clearly extends two pixels, due to diffraction effects. The effect of diffraction on an infinitesimal pinhole is to produce an Airy disk [172] at the detector, which can be written in terms of a first-order Bessel functions of the first kind

$$I(r) = \left(\frac{2J_1(kr)}{kr} \right)^2 \quad (5.24)$$

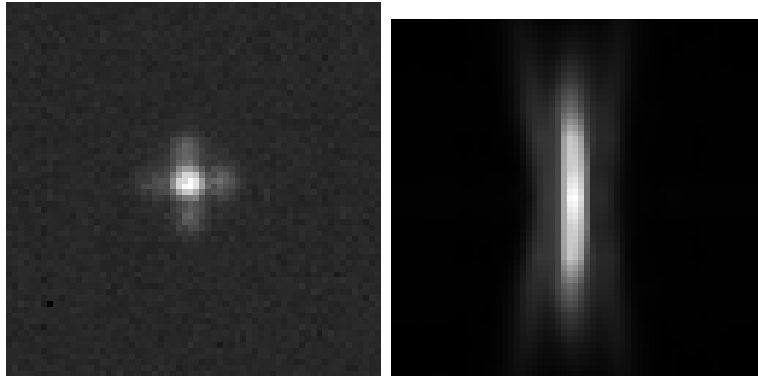


Figure 5.1: **Left:** Chemogram projection image of a 2 μm pinhole measured with a global infrared source. Image is cropped from 128×128 to 64×64 , and each pixel maps $\approx 1.1 \mu\text{m}$ in size. **Right:** Chemogram PSF slice through the center along z -axis, measured from $z = 0$ to 30 μm in 5 μm steps and interpolated to 1 μm steps. Due to the extended acquisition times required when the pinhole is out-of-focus, data are only acquired along the positive z -axis; symmetry is assumed and the data are mirrored about $z = 0$ and processed with a bilateral filter to suppress noise.

Moving the pinhole out of the focal plane has the effect of spreading the PSF, roughly filling a conically-shaped volume in the vertical z -direction (see Fig. 5.1 *right* for infrared, and Fig. 5.5 for bright-field).

Understanding the optical effects of an infinitesimal point is crucial in allowing one to quantify the way in which light behaves for any arbitrary sample of interest. Mattson et al performed two-dimensional deconvolution with a modeled PSF to enhance (or sharpen) FTIR hyperspectral images [173]. In the two-dimensional case, the measured image is the mathematical convolution of the PSF of an infinitesimal pinhole with the “true image:”

$$I_{\text{measured}} = \text{PSF} * I_{\text{true}}$$

where $*$ is the convolutional operator. While an exact reversal of the convolution is impossible due to both a loss of high-frequency information, and deviations of the true PSF from the model, Mattson et al have nevertheless shown that two-dimensional deconvolution can greatly enhance the spatial resolution of FTIR hyperspectral images.

Similarly, just as a pinhole in the focal plane produces a PSF that characterizes the blur of

a measured image, out-of-focus pinhole PSFs describe how a measured image defocuses when the sample moves outside of the focal plane. In the absence of multiple scattering effects, a complete set of pinhole measurements along the z -axis produce a three-dimensional PSF that could in theory be used to reconstruct three-dimensional volumes of data that are also taken about different focal planes along the optical axis.

3D Deconvolution

Performing N sample measurements—ideally such that one measurement is completely in focus at the middle layer of the sample ($z = 0$), while the remaining $N - 1$ measurements are equally split along the $\pm z$ -axis—produces an ordered set of N projection images I_n ($n = 1, \dots, N$). Stacking these projection images in order along the z -axis then fills a volume of data $V = \{I_n | n = 1, \dots, N\}$. Neglecting multiple scattering effects, this volume of data is the “true” sample volume V_{true} , convolved with the three-dimensional PSF (obtained by measuring the pinhole everywhere along the z -axis in a similar manner):

$$V_{\text{measured}} = \text{PSF}_{3\text{D}} * V_{\text{true}}. \quad (5.25)$$

One may recover the true volume by dividing the measurement by the PSF in Fourier space

$$V_{\text{true}} = \text{FFT}^{-1} \left[\frac{\hat{V}_{\text{measured}}}{\hat{\text{PSF}}_{3\text{D}}} \right]. \quad (5.26)$$

where the hat symbol $\hat{}$ denotes the Fourier transform of the quantity, and FFT^{-1} is the inverse Fourier transform operator.

In practice, however, division-by-zero errors and measurement noise result in a loss of information that cannot be recovered by this method of deconvolution. Alternative algorithms exist, e.g. Richardson-Lucy and blind deconvolution, that use various constraints and multiple iterations to better estimate the true data.

Digital optical sectioning

The primary contribution of this section is to extract optical sections using an algorithm inspired by convolutional neural networks (CNNs) [115]. This is motivated by the desire to isolate focal depths where regions of a sample appear in-focus to an observer. CNNs are used extensively in image classification problems, for example face and handwriting recognition. In particular, CNNs allow for translational invariance, so that features can be identified regardless of their position in image space. It is this translational invariance feature, coupled with a measure of the “degree of focus,” that underlies the digital optical sectioning algorithm presented here.

Convolutional neural networks are based on the physiology of living creatures, where retinal neurons tend to overlap rather than have full connectivity. In computer vision, CNNs operate by decomposing images into overlapping windowed segments, which are then processed with various filters. The inner-product between a filter and segment window produces a numerical “activation signal”—used for further processing at a later stage along the network. Since the windows overlap, this process is equivalent to a convolution of the filter and input image. Various convolutional filters are learned by a supervised training of the neural network, such that the greatest activation signal response is achieved for specifically desired features within the input image.

Motivated by the overlapping and processing nature of CNNs, we developed an algorithm that computes a “focus score” as a function of z , given a particular window size and position. Multiple window sizes and scoring techniques are used to build an overall estimate of the sample’s features and their focus positions along z .

Figure 5.2 demonstrates schematically how the algorithm performs for a single window position and size. First, a column of z -axis segments are obtained from a particular window position and size. In the example shown, a 16×16 pixel window positioned near the edge of a microloop sample is used. The second step is to compute the focus of each segment within the column as a function of z . (Methods for computing focus are detailed in Sec. 5.2.2.) The

segments within the column are filtered based on their focus score: those with low relative values are attenuated. Finally, the filtered column of data is added back into a reconstructed dataset (initially empty).

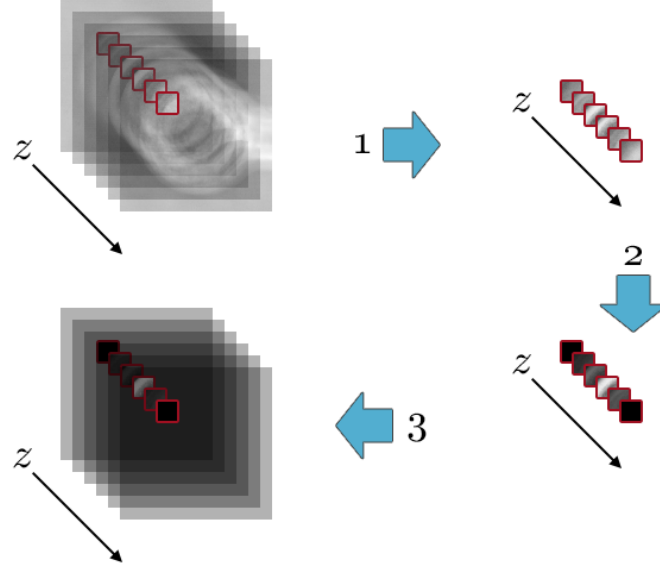


Figure 5.2: **Step 1:** A column of z measurement data are extracted from a window positioned in x , and y . **Step 2:** The column of data is filtered such that positions in z containing minimal focus (by measuring e.g. contrast) are attenuated. **Step 3:** The filtered column of data is added back into the reconstructed dataset. The process repeats for a new overlapping window shifted by one pixel.

Computing Focus

To compute the focus scores, a few statistical measures are performed on the windowed section, including contrast, variance, and frequency/edge content. Two forms of contrast are used, each producing similar results but respond slightly differently: Michelson and Weber. The Michelson contrast of an image segment $I_{u,v}(z)$, where u and v index the pixels within the segment, is computed as

$$\frac{\text{Max}[I_{u,v}](z) - \text{Min}[I_{u,v}](z)}{\text{Max}[I_{u,v}](z) + \text{Min}[I_{u,v}](z)}, \quad (5.27)$$

where the $\text{Max}[I_{u,v}](z)$ operator selects the maximum pixel (u, v) intensity as a function of z . The Weber contrast of an image segment $I_{u,v}(z)$ taken at position (u, v) is computed as

$$\frac{\text{Max}[I_{u,v}](z) - \text{Min}[I_{u,v}](z)}{\bar{I}_{u,v}(z)}, \quad (5.28)$$

with $\bar{I}_{u,v}(z)$ denoting the average of each (u, v) in I as a function of z . The two differ in their usefulness depending on the situation. Since Weber divides by the average intensity, it is more useful in situations where small features sit atop a relatively constant background. Michelson contrast, on the other hand, is useful for periodic features, and quantifies how well the amplitude distinguishes itself from its DC offset.

Calculating the variance is straight forward, using the root-mean-square of the section image (it is not necessary to normalize by the window size since it remains constant along the columns, and filtering is performed on a per-column basis)

$$\sqrt{\sum_{u,v} (I_{u,v}(z) - \bar{I}_{u,v}(z))^2} \quad (5.29)$$

Finally, we look at the (spatial) frequency content of the segment, by multiplying the FFT by an inverted 2D Mexican hat signal (1D shown in fig. 5.3), defined in two dimensional frequency space \vec{f} as

$$\hat{H}(\vec{f}) = \left(1 - \frac{|\vec{f}|^2}{\sigma^2}\right) e^{-|\vec{f}|^2/2\sigma^2} \quad (5.30)$$

where σ^2 controls the Gaussian width, and is chosen such that the maxima occur approximately 70% from the origin of \vec{f} . The purpose of the Gaussian is to suppress large noise errors that can form in what is essentially a second-order differentiation of the input image segment [174]. The resulting “edge energy” content $E(z)$ is obtained by integration of the

square magnitude of this product in Fourier space

$$E(z) \propto \int_0^\infty \int_0^\infty \hat{I}^2(\vec{f}, z) \hat{H}^2(\vec{f}) d\vec{f} \quad (5.31)$$

A plot of $E(z)$ for a windowed section roughly tells when features/edges whose size are of similar order to the window are most pronounced, or in focus.

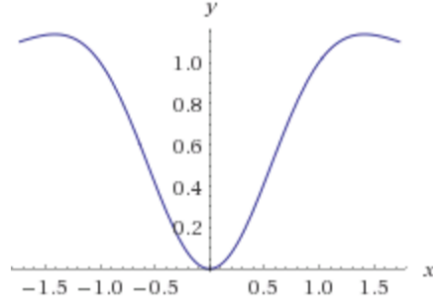
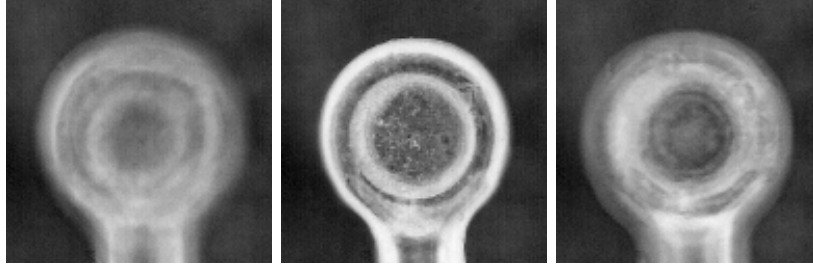


Figure 5.3: 1D inverted Mexican hat function.

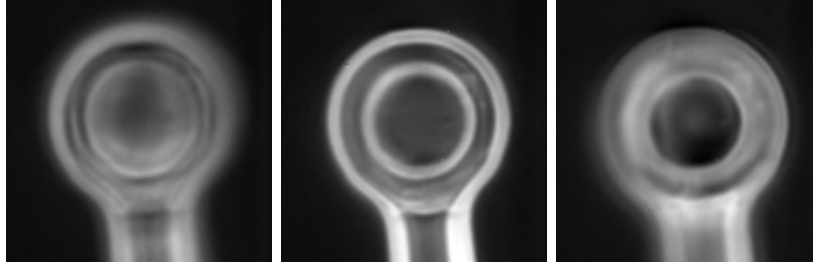
5.2.3 Results

First, the three-dimensional deconvolution method (Sec. 5.2.2) is tested using a 2 μm pinhole to obtain a three-dimensional PSF measurement. These results are compared with the digital optical sectioning method presented in Sec. 5.2.2. Due to the large number of manually stepped measurements required, only a single sample has been measured, and the infrared dataset have limited signal-to-noise. Both the bright-field and infrared measurements were performed of a micro-loop (MiTeGen) that had a thin layer of nail polish deposited on one side; the loop is then suspended in air within the microscope's field of view. The digital optical sectioning methods are demonstrated on both bright-field and mid-infrared measurements.

All data are collected with 1 μm step sizes along the z axis, acquiring 101 total measurements in bright-field (ranging from $z = -50, \dots, 0, \dots, +50$ μm), and 81 measurements for the mid-infrared (ranging from $z = -40, \dots, 0, \dots, +40$ μm). The bright-field measure-



(a) Bright-field images of microloop.



(b) IR chemogram images of microloop

Figure 5.4: From left to right, images are captured with the micro-loop positioned at the focal planes: $-20\ \mu\text{m}$, $0\ \mu\text{m}$, $20\ \mu\text{m}$.

ments are captured over a larger field of view; however, the images have been cropped and down-sampled to 128×128 (with approximately $1.1\ \mu\text{m}$ pixel size) so that the results are consistent with the mid-infrared FPA hyperspectral images. To eliminate dust, scratches and other optical defects from the images, each measurement is divided by a reference measurement taken without a sample in the viewing area, and finally inverted so that dark-field images are obtained. Measurements of the micro-loop acquired at a few focal planes are shown in Fig. 5.4.

Data were collected using a Bruker Hyperion 3000 with a visible camera for bright-field images, and a 128×128 FPA detector for infrared hyperspectral images. Both sets of measurements are taken with $36\times$ magnification. Three-dimensional deconvolution was performed using the freely available DeconvolutionLab [120] plug-in package for ImageJ [121]. All digital optical sectioning algorithms were written in MATLAB [135].

Three-Dimensional Deconvolution

Three-dimensional deconvolution was applied to the bright-field measurements, using the three-dimensional PSF acquired with a 2 μm pinhole stepped along the z -axis (fig. 5.5). Using DeconvolutionLab [120], the best achievable deconvolution results were obtained using the Richardson-Lucy algorithm with TV regularization, and 40 iterations. Results for a few slices of data are shown in Figure 5.7 (d), (e), (f). A maximum intensity projection of the deconvolved data are shown in Figure 5.8 (middle).

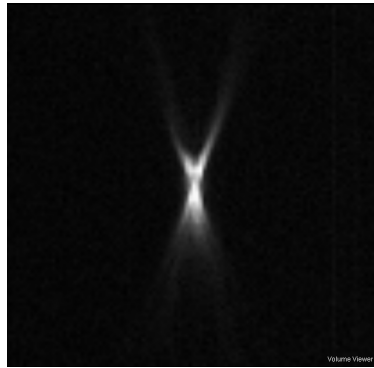


Figure 5.5: Visible three-dimensional PSF for a 2 μm pinhole. Slice taken through $x = 0$, with the z -axis pointing upwards and y -axis pointing to the right.

Digital optical sectioning

The digital optical sectioning method presented in Sec. 5.2.2 is applied to both the bright-field, and infrared measurement of the micro-loop. Examples of the “focus score” calculated using the Michaelson contrast are shown for two window sizes in Figure 5.6. For the smaller window size (4×4), the focus curve is more noisy, and two peaks on either side of $z = 0$ present. In the current version of the algorithm, only the largest peak is considered (occurring at about $+5 \mu\text{m}$). When the window is increased to 16×16 , the focus curve is smoother, and a single peak dominates the curve at about $z = 0$.

Digital optical sectioning is performed using Michaelson contrast, variance, and the “edge energy” calculations given in Sec. 5.2.2, using 2×2 , 4×4 , 8×8 , and 16×16 window sizes for each. An example of the variance calculation with a 2×2 window is shown for a few depths in

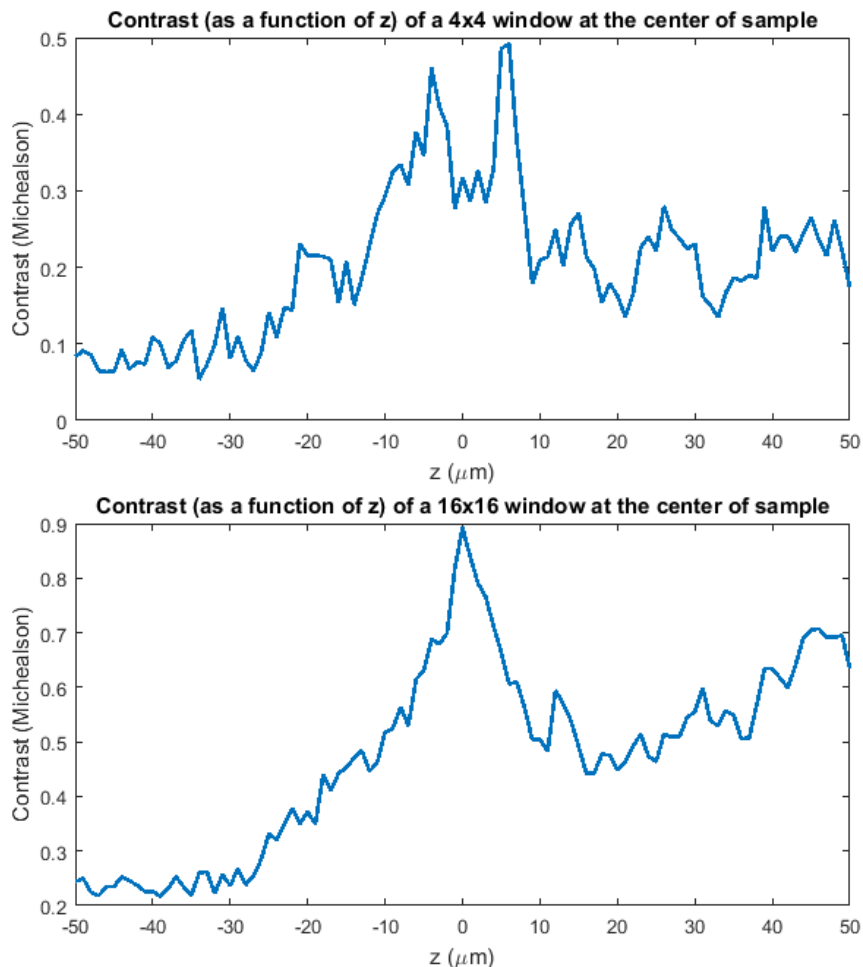


Figure 5.6: Plots of the Michelson contrast calculated for a window positioned in the center of the microloop. **Top:** A 4×4 px² window. **Bottom:** A 16×16 px² window

Figure 5.7, (g), (h), and (i). The cumulative result from averaging each of the 12 calculations are shown in Figure 5.7, (j), (k), and (l). These are compared with the deconvolution results in Figure 5.7, (d), (e), and (f). Additional plots comparing the deconvolution and digital optical sectioning results are shown in Figures 5.8, 5.9, and 5.10.

Infrared results

The large number of manually stepped measurements required by the digital optical sectioning method limited the signal-to-noise of the infrared hyperspectral images. Therefore, integrations over a few bands attributed to distinct chemicals in the micro-loop and nail

polish were performed, with digital optical sectioning applied to these bands. Figure 5.11 shows the obtained spectra; the upper spectrum is captured from the center of the loop, where only nail polish is present, while the lower spectrum is on the micro-loop and contains a mixture of the two spectra. The regions used for integrating the bands (with a polynomial baseline) are highlighted in yellow and pink, corresponding to the micro-loop and nail polish, respectively.

The same procedure that was applied to the bright-field dataset were applied to both of the infrared components (micro-loop and nail polish). That is, twelve calculations using Michaelson contrast, variance, and the “edge energy” functions given in Sec. 5.2.2, using 2×2 , 4×4 , 8×8 , and 16×16 window sizes, were averaged together for both the micro-loop and nail polish components of the infrared dataset. Volume renderings of the results are shown in Figure 5.12, where the micro-loop and nail polish components are combined with their respective colors highlighted in Figure 5.11.

Figure 5.13 shows the estimated focus score for the two components (micro-loop and nail polish), where the two appear to come into focus at slightly different locations along the z -axis. The focus score is calculated using the variance function with an 8×8 window.

5.2.4 Discussion

The results from three-dimensional deconvolution (Figs. 5.7 (d, e, f) and 5.8 (middle)) show some cleaning of the edges; however, it is apparent that this method alone cannot produce confocal results. In particular, Figure 5.8 (middle) shows that the three-dimensional deconvolution method fails to localize any sample features in the z -axis. A number of factors may have limited the deconvolution approach, such as poor-quality PSF measurements, or the fact that a white-light source was used. Point-spread functions are typically defined for monochromatic light [56, 172]. The $2 \mu\text{m}$ pinhole size is on the order of three times the wavelength for bright-field light.

Results from the digital optical sectioning, for both the visible and infrared, show that

confocal-like results may be achieved using measures of its focus. Particularly, both the bright-field and infrared results show that the micro-loop was mounted at a slight angle. This can be seen for the bright-field in Figure 5.9 (right), and for the infrared in Figure 5.12 (rightmost).

A limitation of the digital optical sectioning approach, however is that since it inherently requires the identification of spatial features, samples that are chemically homogeneous within a large region may fail to be identified by the algorithm. Furthermore, the infrared results were obtained using bands that are associated with two distinct chemicals. That means, the methods were not evaluated as to whether voxelated spectra could be obtained. In other words, the results only demonstrated three-dimensional localization of chemicals, but not their relative strengths.

5.2.5 Conclusions

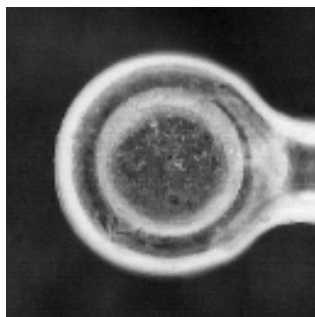
The methods presented for digital confocal microscopy using the techniques presented in Sec. 5.2.2 have shown improved optical sectioning compared to three-dimensional deconvolution methods. However, the method does not take into account multiple scattering. Furthermore, since our method requires information related to features of the sample, the algorithm may be limited in cases where the sample is largely homogeneous. Most samples, however, exhibit some degree of artifacts and discontinuities—even within chemically homogeneous samples.

The methods were also limited by the unavailability of a translating stage (along the axial dimension). Therefore, further testing with mid-infrared hyperspectral datasets is required. Future work may revisit the approach using automated stage control and holographic techniques (e.g., collected using FTHS (see Ch. 4)), such as Fourier ptychography microscopy [122]. Three-dimensional ptychographic transmission microscopy has been demonstrated by Maiden et al using a multi-slice approach for thin samples [123], while extending their methods to thicker samples in 2014 [124]. The method is attractive since it inherently accounts

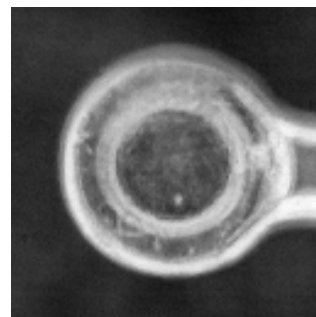
for multiple scattering. Ptychography has also been used to achieve super-resolution [125], and also a non-holographic approach has been demonstrated using LEDs [126].



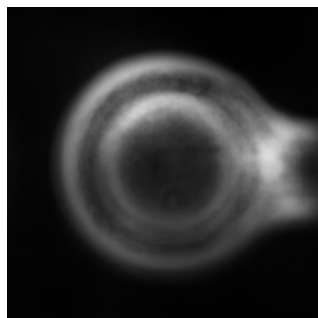
(a) Raw data: $z = -9 \mu\text{m}$



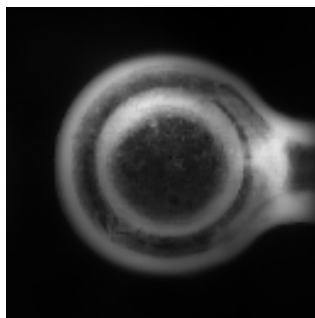
(b) Raw data: $z = 0 \mu\text{m}$



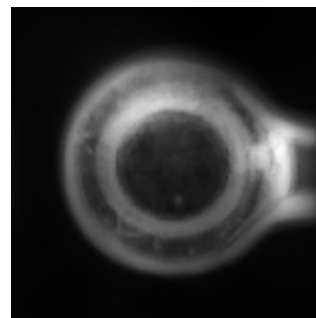
(c) Raw data: $z = +9 \mu\text{m}$



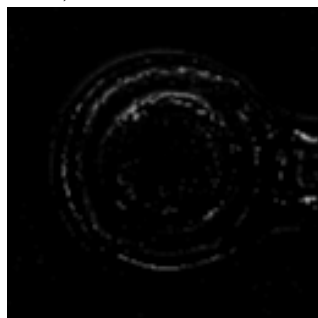
(d) Deconvolution (Rich. Lucy. w/ TV reg.; 40 iters): $z = -9 \mu\text{m}$



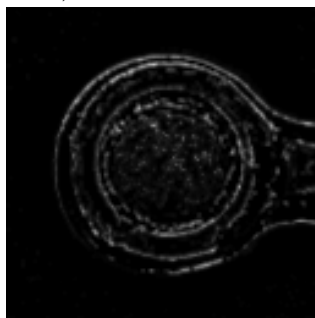
(e) Deconvolution (Rich. Lucy. w/ TV reg.; 40 iters): $z = 0 \mu\text{m}$



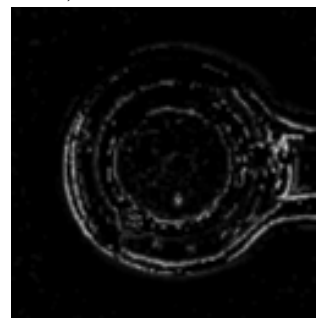
(f) Deconvolution (Rich. Lucy. w/ TV reg.; 40 iters): $z = +9 \mu\text{m}$



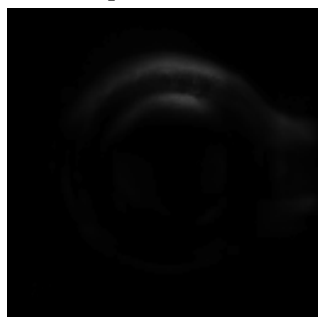
(g) Variance ($2 \times 2\text{px}^2$): $z = -9 \mu\text{m}$



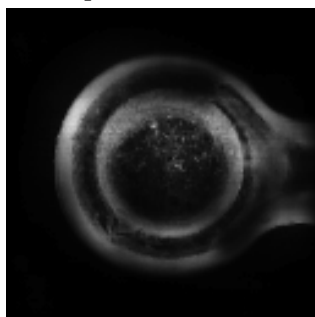
(h) Variance ($2 \times 2\text{px}^2$): $z = 0 \mu\text{m}$



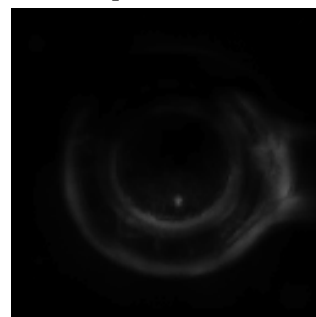
(i) Variance ($2 \times 2\text{px}^2$): $z = +9 \mu\text{m}$



(j) Final: $z = -9 \mu\text{m}$



(k) Final: $z = 0 \mu\text{m}$



(l) Final: $z = +9 \mu\text{m}$

Figure 5.7: Various algorithms applied to the raw bright-field data (top row), each shown at three z positions.

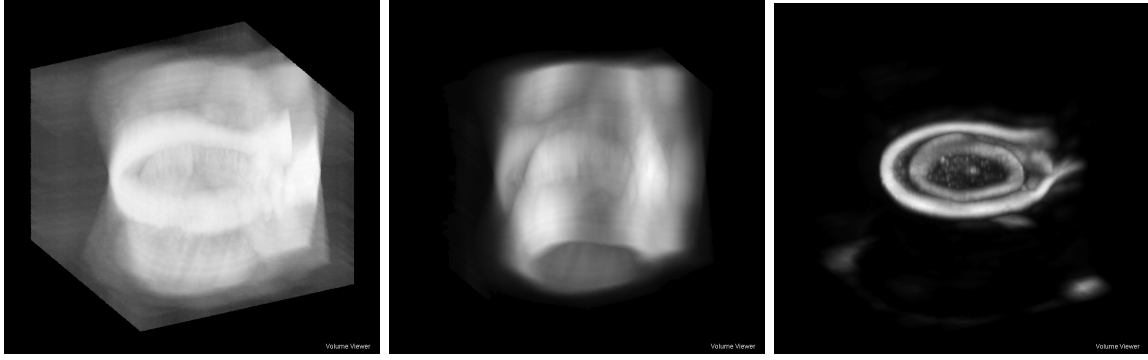


Figure 5.8: Maximum intensity projection images viewed from an angle. **Left:** Raw data. **Middle:** Deconvolved data (Richardson-Lucy with TV normalization, 40 iterations). **Right:** Digital optical sectioning algorithm. The method fails for large $|z|$, where only out-of-focus light ever enters a z window column.

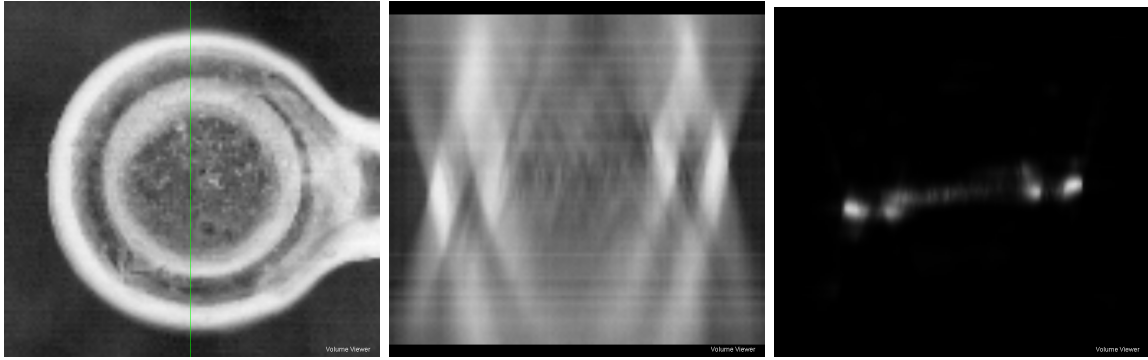


Figure 5.9: **Left:** Raw data at $z = 0$. Vertical green line shows the slice used in both the middle and right figures. **Middle:** Raw data y - z slice at $x = 0$ (z axis points upwards). **Right:** Digital optical sectioning results capture the angle with which the microloop was mounted.

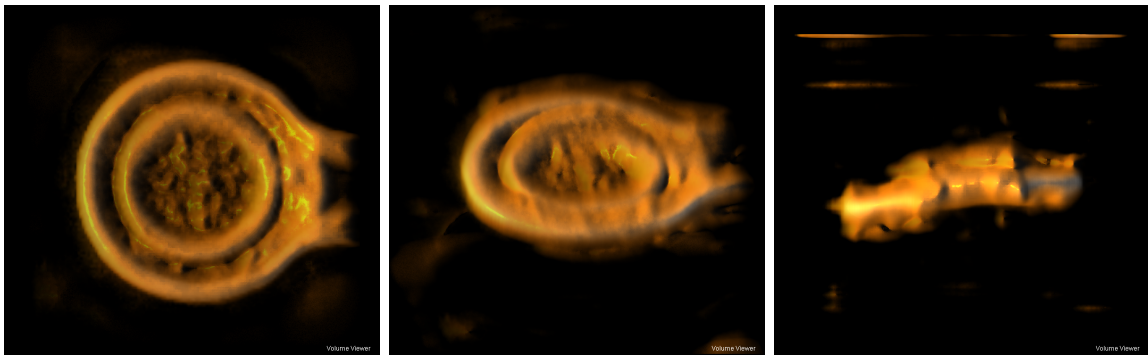


Figure 5.10: Volume renders of the digital optical sectioning results. **Left:** Bird's eye view (looking into the $-z$ direction). **Middle:** At an angle. **Right:** Side view, looking into the $-x$ direction (z -axis pointing upwards), showing that the angle with which the microloop was mounted has been captured by the algorithm.

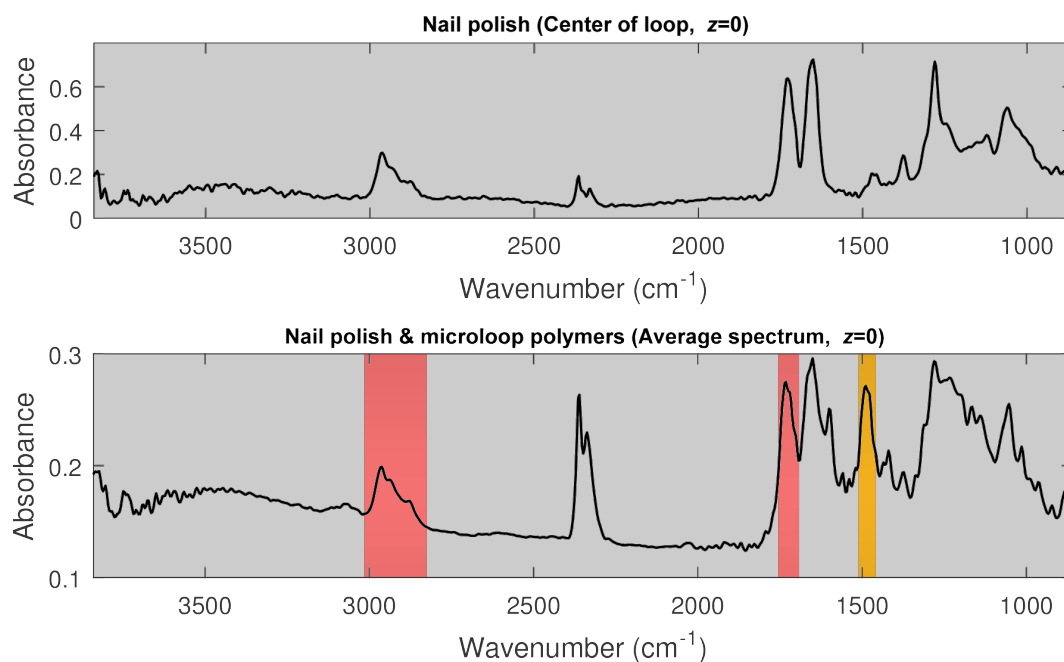


Figure 5.11: Average spectrum at $z = 0$. Yellow regions are attributed to polyimids in the micro-loop while pink regions are attributed to functional groups in the nail polish.

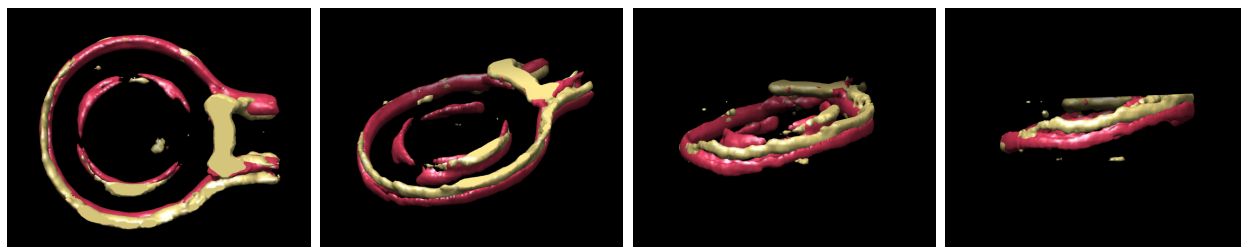


Figure 5.12: Volume renderings from y - x (leftmost) to x - z (rightmost) using color-coded baseline-integrated regions from the spectrum in Fig. 5.11.

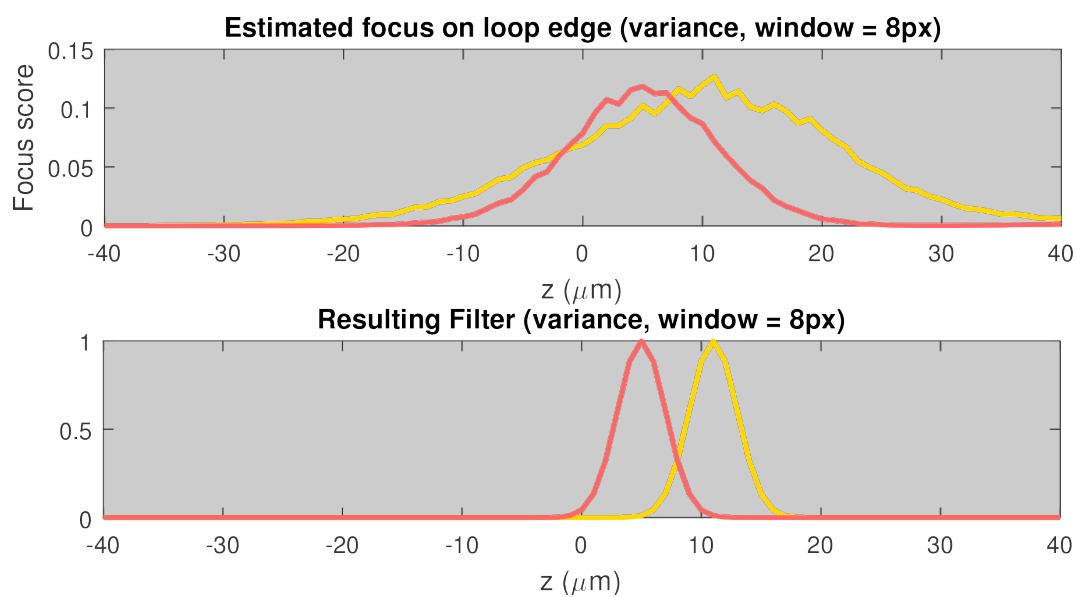


Figure 5.13: Average spectrum at $z = 0$. Yellow regions are attributed to polyimids in the micro-loop while pink regions are attributed to functional groups in the nail polish.

References

- [1] B.H. Stuart. *Infrared Spectroscopy: Fundamentals and Applications*. Analytical Techniques in the Sciences (AnTs). Wiley, 2004.
- [2] P.R. Griffiths and J.A. De Haseth. *Fourier transform infrared spectrometry*. Chemical analysis v. 83. Wiley, 1986.
- [3] Max Diem, Antonella Mazur, Kathleen Lenau, Jen Schubert, Ben Bird, Milo Miljković, Christoph Krafft, and Jürgen Popp. “Molecular pathology via IR and Raman spectral imaging”. In: *Journal of biophotonics*. 6.11-12 (2013), pp. 855–886.
- [4] Ebrahim Aboualizadeh, Christine M Sorenson, Alex J Schofield, Miriam Unger, Nader Sheibani, and Carol Hirschmugl. “Temporal diabetes-induced biochemical changes in distinctive layers of mouse retina”. In: *Scientific Reports* 8 (Dec. 2018).
- [5] Caineng Zou, Maria Mastalerz, Suyun Hu, Carley Gasaway, Yanyan Chen, and Xiaowan Tao. “Applications of Micro-Fourier Transform Infrared Spectroscopy (FTIR) in the Geological Sciences—A Review”. In: *International journal of molecular sciences*. 16.12 (2015), pp. 30223–30250.
- [6] Hongyu Li, Elizabeth C. Minor, and Prosper K. Zigah. “Diagenetic changes in Lake Superior sediments as seen from FTIR and 2D correlation spectroscopy”. In: *Organic Geochemistry* 58 (2013), pp. 125 –136.
- [7] Julio Trevisan, Paul Bassan, Rohit Bhargava, Holly J. Butler, Matthew J Baker, Júlio Trevisan, Holly J Butler, Konrad M Dorling, Peter R Fielden, Simon W Fogarty,

- Nigel J Fullwood, Kelly A Heys, Caryn Hughes, Peter Lasch, Pierre L Martin-Hirsch, Blessing Obinaju, Ganesh D Sockalingum, Josep Sulé-Suso, Rebecca J Strong, and Michael J Walsh. “Using Fourier transform IR spectroscopy to analyze biological materials”. In: *Nature protocols*. 9.8 (2014), pp. 1771–1791.
- [8] Tatiana Konevskikh, Arkadi Ponossov, Reinhold Blümel, Rozalia Lukacs, and Achim Kohler. “Fringes in FTIR spectroscopy revisited: understanding and modelling fringes in infrared spectroscopy of thin films”. In: *Analyst* 140 (12 2015), pp. 3969–3980.
- [9] Melissa Romeo and Max Diem. “Correction of dispersive line shape artifact observed in diffuse reflection infrared spectroscopy and absorption/reflection (transflection) infrared micro-spectroscopy”. In: *Vibrational Spectroscopy* 38.1 (2005), pp. 129 –132.
- [10] C. Bohren and D. R. Huffman. *Absorption and Scattering of Light by Small Particles*. Ed. by C. Bohren and D. R. Huffman. Wiley Science Paperback Series, 1998.
- [11] Brynmor J Davis, P. Scott Carney, P Scott Carney, and Rohit Bhargava. “Theory of Mid-infrared Absorption Microspectroscopy: II. Heterogeneous Samples”. In: *Analytical chemistry*. 82.9 (2010), pp. 3487–3499.
- [12] Brynmor J Davis, P. Scott Carney, P Scott Carney, and Rohit Bhargava. “Theory of Midinfrared Absorption Microspectroscopy: I. Homogeneous Samples”. In: *Analytical chemistry*. 82.9 (2010), pp. 3474–3486.
- [13] Gustav Mie. “Beiträge zur Optik trüber Medien, speziell kolloidaler Metallösungen”. In: *Annalen der physik* 330.3 (1908), pp. 377–445.
- [14] Helmuth Horvath. “Gustav Mie and the scattering and absorption of light by particles: Historic developments and basics”. In: *Journal of Quantitative Spectroscopy and Radiative Transfer* 110.11 (2009). Light Scattering: Mie and More Commemorating 100 years of Mie’s 1908 publication, pp. 787–799.
- [15] H.C. van de Hulst. *Light Scattering by Small Particles*. Structure of Matter Series. John Wiley & Sons, 1957.

- [16] Brian Mohlenhoff, Melissa Romeo, Max Diem, and Bayden R. Wood. “Mie-Type Scattering and Non-Beer-Lambert Absorption Behavior of Human Cells in Infrared Microspectroscopy”. In: *Biophysical Journal* 88.5 (2005), pp. 3635–3640.
- [17] A. Kohler, J. Sulé-Suso, G. D. Sockalingum, M. Tobin, F. Bahrami, Y. Yang, J. Pijanka, P. Dumas, M. Cotte, D. G. van Pittius, G. Parkes, and H. Martens. “Estimating and Correcting Mie Scattering in Synchrotron-Based Microscopic Fourier Transform Infrared Spectra by Extended Multiplicative Signal Correction”. In: *Applied Spectroscopy* 62.3 (2008). PMID: 18339231, pp. 259–266.
- [18] Paul Bassan, Hugh J. Byrne, Franck Bonnier, Joe Lee, Paul Dumas, and Peter Gardner. “Resonant Mie scattering in infrared spectroscopy of biological materials - understanding the ‘dispersion artefact’”. In: *Analyst* 134 (8 2009), pp. 1586–1593.
- [19] Paul Bassan, Achim Kohler, Harald Martens, Joe Lee, Hugh J. Byrne, Paul Dumas, Ehsan Gazi, Michael Brown, Noel Clarke, and Peter Gardner. “Resonant Mie Scattering (RMieS) correction of infrared spectra from highly scattering biological samples”. In: *Analyst* 135 (2 2010), pp. 268–277.
- [20] Tatiana Konevskikh, Rozalia Lukacs, Reinhold Blümel, Arkadi Ponossov, and Achim Kohler. In: *Faraday Discuss.* 187 (0 2016), pp. 235–257.
- [21] Tatiana Konevskikh, Rozalia Lukacs, and Achim Kohler. “An improved algorithm for fast resonant Mie scatter correction of infrared spectra of cells and tissues”. In: *Journal of Biophotonics* 11.1 (2018), e201600307.
- [22] Johanne H. Solheim, Evgeniy Gunko, Dennis Petersen, Frederik Großerüschkamp, Klaus Gerwert, and Achim Kohler. “An open-source code for Mie extinction extended multiplicative signal correction for infrared microscopy spectra of cells and tissues”. In: *Journal of Biophotonics* 0.0 (2019), e201800415.

- [23] Alessandra Vittorini-Orgeas and Antonio Bianconi. “From Majorana Theory of Atomic Autoionization to Feshbach Resonances in High Temperature Superconductors”. In: *Journal of Superconductivity and Novel Magnetism* 22.3 (2009), pp. 215–221.
- [24] Ugo Fano. “Sullo spettro di assorbimento dei gas nobili presso il limite dello spettro d’arco”. In: *Il Nuovo Cimento (1924-1942)* 12.3 (1935), pp. 154–161.
- [25] U. Fano. “Effects of Configuration Interaction on Intensities and Phase Shifts”. In: *Physical Review* 124 (1961), pp. 1866–1878.
- [26] Yong S Joe, Arkady M Satanin, and Chang Sub Kim. “Classical analogy of Fano resonances”. In: *Physica Scripta* 74.2 (2006), pp. 259–266.
- [27] Mikhail V. Rybin, Alexander N. Poddubny, Yuri S. Kivshar, Mikhail F Limonov, Mikhail V Rybin, Alexander N Poddubny, and Yuri S Kivshar. “Fano resonances in photonics”. In: *Nature photonics*. 11.9 (2017), pp. 543–554.
- [28] Alex J. Schofield, Reinhold Blümel, Achim Kohler, Rozalia Lukacs, and Carol J. Hirschmugl. “Extracting pure absorbance spectra in infrared microspectroscopy by modeling absorption bands as Fano resonances”. In: *The Journal of Chemical Physics* 150.15 (2019), p. 154124.
- [29] A.C. Kak, M. Slaney, IEEE Engineering in Medicine, and Biology Society. *Principles of Computerized Tomographic Imaging*. IEEE Press, 1988.
- [30] Xiang Zhu and Dianwen Zhang. “Efficient parallel Levenberg-Marquardt model fitting towards real-time automated parametric imaging microscopy”. In: *PloS one* 8.10 (2013), e76665–e76665.
- [31] Jorge J. Moré. “The Levenberg-Marquardt algorithm: Implementation and theory”. In: *Numerical Analysis*. Ed. by G. A. Watson. Berlin, Heidelberg: Springer Berlin Heidelberg, 1978, pp. 105–116.

- [32] D.V. Likhachev. “Model selection in spectroscopic ellipsometry data analysis: Combining an information criteria approach with screening sensitivity analysis”. In: *Applied Surface Science* 421 (2017). 7th International Conference on Spectroscopic Ellipsometry, pp. 617–623.
- [33] Hirotugu Akaike. “A New Look at the Statistical Model Identification”. In: *Selected Papers of Hirotugu Akaike*. Ed. by Emanuel Parzen, Kunio Tanabe, and Genshiro Kitagawa. New York, NY: Springer New York, 1998, pp. 215–222.
- [34] Hemendra Ghimire, Mahathi Venkataramani, Zhen Bian, Yuan Liu, and A. G. Unil Perera. “ATR-FTIR spectral discrimination between normal and tumorous mouse models of lymphoma and melanoma from serum samples”. In: *Scientific Reports* 7.1 (2017), p. 16993.
- [35] Maja Stankovic, Ruzica Nikolic, Dragan Djordjevic, Nenad Krstić, Milos Djordjevic, and Jasmina Jovanovic. “The application of micro-Fourier transform infrared spectroscopy in biomedical sciences: The investigation of biological mineral tissues and histopathological materials”. In: *Advanced technologies* 4 (Jan. 2015), pp. 53–59.
- [36] R. Salzer and H.W. Siesler. *Infrared and Raman Spectroscopic Imaging*. Wiley, 2014.
- [37] Michael C. Martin, Charlotte Dabat-Blondeau, Miriam Unger, Julia Sedlmair, Dilworth Y. Parkinson, Hans A. Bechtel, Barbara Illman, Jonathan M. Castro, Marco Keiluweit, David Buschke, Brenda Ogle, Michael J. Nasse, and Carol J. Hirschmugl. “3D spectral imaging with synchrotron Fourier transform infrared spectro-microtomography”. In: *Nat Meth* 10.9 (2013). Brief Communication, pp. 861–864.
- [38] Luca Quaroni, Martin Obst, Marcus Nowak, and Fabio Zobi. “Three-Dimensional Mid-Infrared Tomographic Imaging of Endogenous and Exogenous Molecules in a Single Intact Cell with Subcellular Resolution”. In: *Angewandte Chemie International Edition* 54.1 (2015), pp. 318–322.

- [39] Sylvain Clède, Clotilde Policar, and Christophe Sandt. “Fourier Transform Infrared (FT-IR) Spectromicroscopy to Identify Cell Organelles: Correlation with Fluorescence Staining in MCF-7 Breast Cancer Cells”. In: *Applied Spectroscopy* 68.1 (2014), pp. 113–117.
- [40] Peter Lasch, Anthony Pacifico, and Max Diem. “Spatially resolved IR microspectroscopy of single cells”. In: *Biopolymers* 67.4-5 (2002), pp. 335–338.
- [41] Julia Sedlmair, Robert E. Peale, Carol J. Hirschmugl, Mehmet Yesiltas, Robert E Peale, and Carol J Hirschmugl. “Synchrotron-Based Three-Dimensional Fourier-Transform Infrared Spectro-Microtomography of Murchison Meteorite Grain”. In: *Applied spectroscopy* 71.6 (2017), pp. 1198–1208.
- [42] A.J. Devaney. *Mathematical Foundations of Imaging, Tomography and Wavefield Inversion*. Mathematical Foundations of Imaging, Tomography and Wavefield Inversion. Cambridge University Press, 2012.
- [43] Yongjin Sung and Ramachandra R. Dasari. “Deterministic regularization of three-dimensional optical diffraction tomography”. In: *J. Opt. Soc. Am. A* 28.8 (2011), pp. 1554–1561.
- [44] JooWon Lim, KyeoReh Lee, Kyong Hwan Jin, Seungwoo Shin, SeoEun Lee, YongKeun Park, and Jong Chul Ye. “Comparative study of iterative reconstruction algorithms for missing cone problems in optical diffraction tomography”. In: *Opt. Express* 23.13 (2015), pp. 16933–16948.
- [45] B. Goris, W. Van den Broek, K.J. Batenburg, H. Heidari Mezerji, and S. Bals. “Electron tomography based on a total variation minimization reconstruction technique”. In: *Ultramicroscopy* 113 (2012), pp. 120–130.
- [46] Yuchen Deng, Yu Chen, Yan Zhang, Shengliu Wang, Fa Zhang, and Fei Sun. “ICON: 3D reconstruction with ‘missing-information’ restoration in biological electron tomography”. In: *Journal of Structural Biology* 195.1 (2016), pp. 100–112.

- [47] Laurène Donati, Masih Nilchian, Sylvain Trépout, Cédric Messaoudi, Sergio Marco, and Michael Unser. “Compressed sensing for STEM tomography”. In: *Ultramicroscopy* 179 (2017), pp. 47–56.
- [48] Eva Bladt, Daniël M. Pelt, Sara Bals, and Kees Joost Batenburg. “Electron tomography based on highly limited data using a neural network reconstruction technique”. In: *Ultramicroscopy* 158 (2015), pp. 81–88.
- [49] Rongping Zeng, Subok Park, Predrag Bakic, and Kyle J Myers. “Evaluating the sensitivity of the optimization of acquisition geometry to the choice of reconstruction algorithm in digital breast tomosynthesis through a simulation study”. In: *Physics in Medicine and Biology* 60.3 (2015), pp. 1259–1288.
- [50] James T Dobbins and Devon J Godfrey. “Digital x-ray tomosynthesis: current state of the art and clinical potential”. In: *Physics in Medicine and Biology* 48.19 (2003), R65–R106.
- [51] L. Helfen, T. Baumbach, P. Mikulík, D. Kiel, P. Pernot, P. Cloetens, and J. Baruchel. “High-resolution three-dimensional imaging of flat objects by synchrotron-radiation computed laminography”. In: *Applied Physics Letters* 86.7 (2005), p. 071915.
- [52] R. A. Lewis. “Medical phase contrast x-ray imaging: current status and future prospects”. In: *Physics in Medicine and Biology* 49.16 (2004), pp. 3573–3583.
- [53] David Smith, James S. Wilkinson, David J Rowe, and James S Wilkinson. “Complex refractive index spectra of whole blood and aqueous solutions of anticoagulants, analgesics and buffers in the mid-infrared”. In: *Scientific reports*. 7.1 (2017).
- [54] Brian W. Pogue and Michael S. Patterson. “Review of tissue simulating phantoms for optical spectroscopy, imaging and dosimetry”. In: *Journal of Biomedical Optics* 11.4 (2006), pp. 1–16–16.
- [55] E. Hecht. *Optics*. Pearson education. Addison-Wesley, 2002.

- [56] J.W. Goodman. *Introduction to Fourier Optics*. McGraw-Hill physical and quantum electronics series. W. H. Freeman, 2005.
- [57] Y. Shechtman, Y. C. Eldar, O. Cohen, H. N. Chapman, J. Miao, and M. Segev. “Phase Retrieval with Application to Optical Imaging: A contemporary overview”. In: *IEEE Signal Processing Magazine* 32.3 (2015), pp. 87–109.
- [58] B.E.A. Saleh and M.C. Teich. *Fundamentals of Photonics*. Wiley Series in Pure and Applied Optics. Wiley, 2007.
- [59] Gabriel Popescu, Takahiro Ikeda, Ramachandra R. Dasari, and Michael S. Feld. “Diffraction phase microscopy for quantifying cell structure and dynamics”. In: *Opt. Lett.* 31.6 (2006), pp. 775–777.
- [60] Zilker, A., Engelhardt, H., and Sackmann, E. “Dynamic reflection interference contrast (RIC-) microscopy: a new method to study surface excitations of cells and to measure membrane bending elastic moduli”. In: *J. Phys. France* 48.12 (1987), pp. 2139–2151.
- [61] KyeoReh Lee, Kyoohyun Kim, Jaehwang Jung, Ji Han Heo, Sangyeon Cho, Lee Sangyun, Gyu Young Chang, Young Ju Jo, Hyunjoo Park, and YongKeun Park. “Quantitative Phase Imaging Techniques for the Study of Cell Pathophysiology: From Principles to Applications”. In: *Sensors* 13 (Apr. 2013), pp. 4170–4191.
- [62] Micah H. Jenkins and Thomas K. Gaylord. “Three-dimensional quantitative phase imaging via tomographic deconvolution phase microscopy”. In: *Appl. Opt.* 54.31 (2015), pp. 9213–9227.
- [63] Thomas A. Zangle and Michael A. Teitell. “Live-cell mass profiling: an emerging approach in quantitative biophysics”. In: *Nature Methods* 11 (2014). Perspective, 1221 EP –.

- [64] Benjamin Rappaz, Pierre Marquet, Etienne Cuche, Yves Emery, Christian Depeursinge, and Pierre J. Magistretti. “Measurement of the integral refractive index and dynamic cell morphometry of living cells with digital holographic microscopy”. In: *Opt. Express* 13.23 (2005), pp. 9361–9373.
- [65] J. R. Fienup. “Phase retrieval algorithms: a comparison”. In: *Appl. Opt.* 21.15 (1982), pp. 2758–2769.
- [66] D. Russell Luke, James V. Burke, and Richard G. Lyon. “Optical Wavefront Reconstruction: Theory and Numerical Methods”. In: *SIAM Review* 44.2 (2002), pp. 169–224.
- [67] Michael Reed Teague. “Deterministic phase retrieval: a Green’s function solution”. In: *J. Opt. Soc. Am.* 73.11 (1983), pp. 1434–1441.
- [68] N. Streibl. “Phase imaging by the transport equation of intensity”. In: *Optics Communications* 49.1 (1984), pp. 6–10.
- [69] Chao Zuo, Qian Chen, and Anand Asundi. “Comparison of Digital Holography and Transport of Intensity for Quantitative Phase Contrast Imaging”. In: *Fringe 2013*. Ed. by Wolfgang Osten. Berlin, Heidelberg: Springer Berlin Heidelberg, 2014, pp. 137–142.
- [70] José A. Ferrari, Gastón A. Ayubi, Jorge L. Flores, and César D. Perciante. “Transport of intensity equation: Validity limits of the usually accepted solution”. In: *Optics Communications* 318 (2014), pp. 133–136.
- [71] Yunhui Zhu, Zhengyun Zhang, and George Barbastathis. “Phase imaging for absorptive phase objects using hybrid uniform and structured illumination Transport of Intensity Equation”. In: *Opt. Express* 22.23 (2014), pp. 28966–28976.
- [72] Laura Waller, Lei Tian, and George Barbastathis. “Transport of Intensity phase-amplitude imaging with higher order intensity derivatives”. In: *Opt. Express* 18.12 (2010), pp. 12552–12561.

- [73] Zhong Jingshan, Rene A. Claus, Justin Dauwels, Lei Tian, and Laura Waller. “Transport of Intensity phase imaging by intensity spectrum fitting of exponentially spaced defocus planes”. In: *Opt. Express* 22.9 (2014), pp. 10661–10674.
- [74] Chao Zuo, Qian Chen, Yingjie Yu, and Anand Asundi. “Transport-of-intensity phase imaging using Savitzky-Golay differentiation filter - theory and applications”. In: *Opt. Express* 21.5 (2013), pp. 5346–5362.
- [75] D. GABOR. “A New Microscopic Principle”. In: *Nature* 161.4098 (1948), pp. 777–778.
- [76] Dennis Gabor. *Nobel Lecture: Holography, 1948-1971*. 1971.
- [77] Emmett N. Leith and Juris Upatnieks. “Wavefront Reconstruction with Continuous-Tone Objects*”. In: *J. Opt. Soc. Am.* 53.12 (1963), pp. 1377–1381.
- [78] Emmett N. Leith and Juris Upatnieks. “Wavefront Reconstruction with Diffused Illumination and Three-Dimensional Objects*”. In: *J. Opt. Soc. Am.* 54.11 (1964), pp. 1295–1301.
- [79] Tatiana Latychevskaia and Hans-Werner Fink. “Practical algorithms for simulation and reconstruction of digital in-line holograms”. In: *Appl. Opt.* 54.9 (2015), pp. 2424–2434.
- [80] Lu Rong, Yan Li, Shuo Liu, Wen Xiao, Feng Pan, and Dayong Wang. “Iterative solution to twin image problem in in-line digital holography”. In: *Optics and Lasers in Engineering* 51.5 (2013), pp. 553–559.
- [81] K.A. Nugent. “Twin-image elimination in Gabor holography”. In: *Optics Communications* 78.3 (1990), pp. 293–299.
- [82] Junseong Eom and Sangjun Moon. “Three-Dimensional High-Resolution Digital In-line Hologram Reconstruction with a Volumetric Deconvolution Method”. In: *Sensors* 18 (Sept. 2018), p. 2918.

- [83] Tatiana Latychevskaia and Hans-Werner Fink. “Holographic time-resolved particle tracking by means of three-dimensional volumetric deconvolution”. In: *Opt. Express* 22.17 (2014), pp. 20994–21003.
- [84] P. Hariharan. *Basics of Holography*. Cambridge University Press, 2002.
- [85] Myung K. Kim. “Principles and techniques of digital holographic microscopy”. In: *SPIE Reviews* 1.1 (2010), pp. 1 –51 –51.
- [86] “Elementary Speckle Interferometry”. eng. In: *Full-Field Measurements and Identification in Solid Mechanics*. Hoboken, NJ USA: John Wiley & Sons, Inc., 2012, pp. 125–156.
- [87] Robert Jones. *Holographic and speckle interferometry: a discussion of the theory, practice, and application of the techniques*. eng. Second edition. Cambridge studies in modern optics ; 6. Cambridge [England] ; New York: Cambridge University Press, 1989.
- [88] Joseph Goodman. *Speckle Phenomena in Optics: Theory and Applications*. Jan. 2007.
- [89] Vittorio Bianco, Pasquale Memmolo, Marco Leo, Silvio Montresor, Cosimo Distante, Melania Paturzo, Pascal Picart, Bahram Javidi, and Pietro Ferraro. “Strategies for reducing speckle noise in digital holography”. In: *Light: Science & Applications* 7.1 (2018), p. 48.
- [90] L. Suzanne Leslie, Andre Kadjacsy-Balla, and Rohit Bhargava. “High-definition fourier transform infrared spectroscopic imaging of breast tissue”. In: *Progress in Biomedical Optics and Imaging - Proceedings of SPIE*. Vol. 9420. SPIE, 2015.
- [91] Saumya Tiwari, Vijaya B. Reddy, Rohit Bhargava, and Jaishankar Raman. “Computational Chemical Imaging for Cardiovascular Pathology: Chemical Microscopic Imaging Accurately Determines Cardiac Transplant Rejection”. In: *PLOS ONE* 10.5 (2015), pp. 1–15.

- [92] Jayakrupakar Nallala, Gavin Rhys Lloyd, Michael Hermes, Neil Shepherd, and Nick Stone. “Enhanced spectral histology in the colon using high-magnification benchtop FTIR imaging”. In: *Vibrational Spectroscopy* 91.Supplement C (2017). Prominent Young Vibrational Spectroscopists, pp. 83–91.
- [93] Sylvain Clède, François Lambert, Christophe Sandt, Slavka Kascakova, Miriam Unger, Etienne Harté, Marie-Aude Plamont, Rénette Saint-Fort, Ariane Deniset-Besseau, Zoher Gueroui, Carol Hirschmugl, Sophie Lecomte, Alexandre Dazzi, Anne Vessières, and Clotilde Policar. “Detection of an estrogen derivative in two breast cancer cell lines using a single core multimodal probe for imaging (SComPI) imaged by a panel of luminescent and vibrational techniques”. In: *Analyst* 138.19 (2013), pp. 5627–5638.
- [94] Reza Salem, Zack Jiang, Dongfeng Liu, Robert Pafchek, David Gardner, Paul Foy, Mohammed Saad, Doug Jenkins, Alex Cable, and Peter Fendel. “Mid-infrared supercontinuum generation spanning 1.8 octaves using step-index indium fluoride fiber pumped by a femtosecond fiber laser near 2 μm ”. In: *Opt. Express* 23.24 (2015), pp. 30592–30602.
- [95] Claus Kuepper, Angela Kallenbach-Thieltges, Hendrik Juetten, Andrea Tannapfel, Frederik Großerueschkamp, and Klaus Gerwert. “Quantum Cascade Laser-Based Infrared Microscopy for Label-Free and Automated Cancer Classification in Tissue Sections”. In: *Scientific Reports* 8.1 (2018), p. 7717.
- [96] Ludwig Zehnder. “Ein neuer Interferenzrefraktor”. In: *Zeitschrift für Instrumentenkunde* 11 (1891), pp. 275–285.
- [97] Ludwig Mach. “Ueber einen interferenzrefraktor”. In: *Zeitschrift für Instrumentenkunde* 12.3 (1892), p. 89.
- [98] Ichirou Yamaguchi and Tong Zhang. “Phase-shifting digital holography”. In: *Opt. Lett.* 22.16 (1997), pp. 1268–1270.

- [99] N. Warnasooriya and M. K. Kim. “LED-based multi-wavelength phase imaging interference microscopy”. In: *Opt. Express* 15.15 (2007), pp. 9239–9247.
- [100] Ichirou Yamaguchi, Tatsuki Matsumura, and Jun ichi Kato. “Phase-shifting color digital holography”. In: *Opt. Lett.* 27.13 (2002), pp. 1108–1110.
- [101] Nienke Bosschaart, Maurice C. Aalders, Dirk J. Faber, Jelmer J. Weda, Martin J. van Gemert, and Ton G. van Leeuwen. “Quantitative measurements of absorption spectra in scattering media by low-coherence spectroscopy”. In: *Opt. Lett.* 34.23 (2009), pp. 3746–3748.
- [102] Nienke Bosschaart, Dirk J. Faber, Ton G. van Leeuwen, and Maurice C. G. Aalders. “In vivo low-coherence spectroscopic measurements of local hemoglobin absorption spectra in human skin”. In: *Journal of Biomedical Optics* 16.10 (2011), pp. 1–4.
- [103] V. Duc Nguyen, D. J. Faber, E. van der Pol, T. G. van Leeuwen, and J. Kalkman. “Dependent and multiple scattering in transmission and backscattering optical coherence tomography”. In: *Opt. Express* 21.24 (2013), pp. 29145–29156.
- [104] A. K. Trull, J. van der Horst, J. G. Bijster, and J. Kalkman. “Transmission optical coherence tomography based measurement of optical material properties”. In: *Opt. Express* 23.26 (2015), pp. 33550–33563.
- [105] A. K. Trull, J. van der Horst, J. G. Bijster, and J. Kalkman. “Transmission optical coherence tomography sensing”. In: *Optical Sensing and Detection IV*. Ed. by Francis Berghmans and Anna G. Editors Mignani. SPIE, 2016.
- [106] Di Jin, Renjie Zhou, Zahid Yaqoob, and Peter T. C. So. “Tomographic phase microscopy: principles and applications in bioimaging (Invited)”. In: *J. Opt. Soc. Am. B* 34.5 (2017), B64–B77.
- [107] Yongjin Sung, Niyom Lue, Bashar Hamza, Joseph Martel, Daniel Irimia, Ramachandra R. Dasari, Wonshik Choi, Zahid Yaqoob, and Peter So. “Three-Dimensional Holo-

- graphic Refractive-Index Measurement of Continuously Flowing Cells in a Microfluidic Channel”. In: *Physical review applied* 1 (2014), p. 014002.
- [108] Yongjin Sung, Wonshik Choi, Christopher Fang-Yen, Kamran Badizadegan, Ramachandra R. Dasari, and Michael S. Feld. “Optical diffraction tomography for high resolution live cell imaging”. In: *Opt. Express* 17.1 (2009), pp. 266–277.
 - [109] H. Liu, U. S. Kamilov, D. Liu, H. Mansour, and P. T. Boufounos. “Compressive imaging with iterative forward models”. In: (2017), pp. 6025–6029.
 - [110] H. Liu, D. Liu, H. Mansour, P. T. Boufounos, L. Waller, and U. S. Kamilov. “SEAGLE: Sparsity-Driven Image Reconstruction Under Multiple Scattering”. In: *IEEE Transactions on Computational Imaging* 4.1 (2018), pp. 73–86.
 - [111] Emmanuel Soubies, Thanh-An Pham, and Michael Unser. “Efficient inversion of multiple-scattering model for optical diffraction tomography”. In: *Opt. Express* 25.18 (2017), pp. 21786–21800.
 - [112] Yu Sun, Zhihao Xia, and Ulugbek S. Kamilov. “Efficient and accurate inversion of multiple scattering with deep learning”. In: *Opt. Express* 26.11 (2018), pp. 14678–14688.
 - [113] JooWon Lim, Alexandre Goy, Morteza Hasani Shoreh, Michael Unser, and Demetri Psaltis. “Imaging complex objects using learning tomography”. In: 10503 (2018).
 - [114] JooWon Lim, Abdul Wahab, GwangSik Park, KyeoReh Lee, YongKeun Park, and Jong Chul Ye. “Beyond Born-Rytov limit for super-resolution optical diffraction tomography”. In: *Opt. Express* 25.24 (2017), pp. 30445–30458.
 - [115] Yann LeCun, Yoshua Bengio, and Geoffrey Hinton. “Deep learning”. In: *Nature* 521 (2015), 436 EP –.
 - [116] S.K. Nayar and Yasuo Nakagawa. “Shape from focus: An effective approach for rough surfaces”. In: June 1990, 218 –225 vol.2.

- [117] Y Xiong and S.A. Shafer. “Depth from focusing and defocusing”. In: July 1993, pp. 68–73.
- [118] F. Aguet, D. Van De Ville, and M. Unser. “Model-Based 2.5-D Deconvolution for Extended Depth of Field in Brightfield Microscopy”. In: *IEEE Transactions on Image Processing* 17.7 (2008), pp. 1144–1153.
- [119] Brigitte Forster, Dimitri Van De Ville, Jesse Berent, Daniel Sage, and Michael Unser. “Complex wavelets for extended depth-of-field: A new method for the fusion of multichannel microscopy images”. In: *Microscopy Research and Technique* 65.1-2 (2004), pp. 33–42.
- [120] Cédric Vonesch, Raquel Terrés Cristofani, and Guillaume Schmit. *DeconvolutionLab*. Version 14.02.2014. Mar. 2016.
- [121] Caroline A. Schneider, Wayne S. Rasband, and Kevin W. Eliceiri. “NIH Image to ImageJ: 25 years of image analysis”. In: *Nature Methods* 9 (2012), pp. 671–675.
- [122] Guoan Zheng, Roarke Horstmeyer, and Changhuei Yang. “Wide-field, high-resolution Fourier ptychographic microscopy”. In: *Nature photonics* 7.9 (2013), pp. 739–745.
- [123] A. M. Maiden, M. J. Humphry, and J. M. Rodenburg. “Ptychographic transmission microscopy in three dimensions using a multi-slice approach”. In: *J. Opt. Soc. Am. A* 29.8 (2012), pp. 1606–1614.
- [124] T. M. Godden, R. Suman, M. J. Humphry, J. M. Rodenburg, and A. M. Maiden. “Ptychographic microscope for three-dimensional imaging”. In: *Opt. Express* 22.10 (2014), pp. 12513–12523.
- [125] Andrew M. Maiden, Martin J. Humphry, Fucui Zhang, and John M. Rodenburg. “Superresolution imaging via ptychography”. In: *J. Opt. Soc. Am. A* 28.4 (2011), pp. 604–612.
- [126] Lei Tian and Laura Waller. “3D intensity and phase imaging from light field measurements in an LED array microscope”. In: *Optica* 2.2 (2015), pp. 104–111.

- [127] Taewoo Kim, Renjie Zhou, Mustafa Mir, S Derin Babacan, P Carney, Lynford Goddard, and Gabriel Popescu. “White-light diffraction tomography of unlabeled live cells”. In: *Nature Photonics* 8 (Jan. 2014), pp. 256–263.
- [128] Milos Miljkovic, Benjamin Bird, and Max Diem. “Line shape distortion effects in infrared spectroscopy”. In: *Analyst* 137 (17 2012), pp. 3954–3964.
- [129] Vincenzo Giannini, Yan Francescato, Hemmel Amrania, Chris C. Phillips, and Stefan A. Maier. “Fano Resonances in Nanoscale Plasmonic Systems: A Parameter-Free Modeling Approach”. In: *Nano Letters* 11.7 (2011). PMID: 21635012, pp. 2835–2840.
- [130] Ronen Adato, Alp Artar, Shyamsunder Erramilli, and Hatice Altug. “Engineered Absorption Enhancement and Induced Transparency in Coupled Molecular and Plasmonic Resonator Systems”. In: *Nano Letters* 13.6 (2013). PMID: 23647070, pp. 2584–2591.
- [131] Tomáš Neuman, Christian Huck, Jochen Vogt, Frank Neubrech, Rainer Hillenbrand, Javier Aizpurua, and Annemarie Pucci. “Importance of Plasmonic Scattering for an Optimal Enhancement of Vibrational Absorption in SEIRA with Linear Metallic Antennas”. In: *The Journal of Physical Chemistry C* 119.47 (2015), pp. 26652–26662.
- [132] Paul Bassan, Joe Lee, Ashwin Sachdeva, Juliana Pissardini, Konrad M. Dorling, John S. Fletcher, Alex Henderson, and Peter Gardner. “The inherent problem of transflection-mode infrared spectroscopic microscopy and the ramifications for biomedical single point and imaging applications”. In: *Analyst* 138 (1 2013), pp. 144–157.
- [133] M. I. Tribelsky, A. E. Miroshnichenko, and Y. S. Kivshar. “Unconventional Fano resonances in light scattering by small particles”. In: *EPL (Europhysics Letters)* 97.4 (2012), p. 44005.
- [134] Thomas G. Mayerhöfer, Harald Mutschke, and Jürgen Popp. “Employing Theories Far beyond Their Limits—The Case of the (Boguer-) Beer–Lambert Law”. In: *ChemPhysChem* 17.13 (2016), pp. 1948–1955.

- [135] *MATLAB Version 8.6.0.267246 (R2015b)*. The MathWorks Inc. Natick, Massachusetts, 2015.
- [136] J. Hsieh. *Computed Tomography: Principles, Design, Artifacts, and Recent Advances*. Press Monograph Series. SPIE, 2015.
- [137] Steven L Jacques. “Optical properties of biological tissues: a review”. In: *Physics in Medicine & Biology* 58.11 (2013), R37.
- [138] G.B. Arfken, H.J. Weber, and F.E. Harris. *Mathematical Methods for Physicists: A Comprehensive Guide*. Elsevier, 2012.
- [139] C. Hughes, A. Henderson, M. Kansiz, K. M. Dorling, M. Jimenez-Hernandez, M. D. Brown, N. W. Clarke, and P. Gardner. “Enhanced FTIR bench-top imaging of single biological cells”. In: *Analyst* 140 (7 2015), pp. 2080–2085.
- [140] The Sage Developers. *SageMath, the Sage Mathematics Software System (Version 8.0)*. 2017.
- [141] Ghazal Azarfar, Ebrahim Aboulizadeh, Nicholas M. Walter, Simona Ratti, Camilla Olivieri, Alessandra Norici, Michael Nasse, Achim Kohler, Mario Giordano, and Carol J. Hirschmugl. “Estimating and correcting interference fringes in infrared spectra in infrared hyperspectral imaging”. In: *Analyst* 143 (19 2018), pp. 4674–4683.
- [142] R. Lukacs, R. Blümel, B. Zimmerman, M. Bağcıoğlu, and A. Kohler. “Recovery of absorbance spectra of micrometer-sized biological and inanimate particles”. In: *Analyst* 140 (9 2015), pp. 3273–3284.
- [143] Jan Schäfer. *MatScat*. Version 1.4.0.0. Apr. 2016.
- [144] Jan-Patrick Schäfer. “Implementierung und Anwendung analytischer und numerischer Verfahren zur Lösung der Maxwellgleichungen für die Untersuchung der Lichtausbreitung in biologischem Gewebe”. PhD thesis. Universität Ulm, 2011.

- [145] Paul Bassan, Ashwin Sachdeva, Achim Kohler, Caryn Hughes, Alex Henderson, Jonathan Boyle, Jonathan H. Shanks, Michael Brown, Noel W. Clarke, and Peter Gardner. “FTIR microscopy of biological cells and tissue: data analysis using resonant Mie scattering (RMieS) EMSC algorithm”. In: *Analyst* 137 (6 2012), pp. 1370–1377.
- [146] Nina Sultanova, S Kasarova, and I Nikolov. “Dispersion Properties of Optical Polymers”. In: *ACTA PHYSICA POLONICA A* 116 (Oct. 2009), pp. 585–587.
- [147] H. H. Li. “Refractive index of alkali halides and its wavelength and temperature derivatives”. In: *Journal of Physical and Chemical Reference Data* 5 (Apr. 1976), pp. 329–528.
- [148] Sebastian Berisha, Thomas van Dijk, Rohit Bhargava, P. Scott Carney, and David Mayerich. “BIM-Sim: Interactive Simulation of Broadband Imaging Using Mie Theory”. In: *Frontiers in Physics* 5 (2017), p. 5.
- [149] L. Marple. “Computing the discrete-time “analytic” signal via FFT”. In: *IEEE Transactions on Signal Processing* 47.9 (1999), pp. 2600–2603.
- [150] Michael Feldman. *Hilbert Transform Applications in Mechanical Vibration*. John Wiley & Sons, 2011.
- [151] Thomas van Dijk, David Mayerich, P. Scott Carney, and Rohit Bhargava. “Recovery of Absorption Spectra from Fourier Transform Infrared (FT-IR) Microspectroscopic Measurements of Intact Spheres”. In: *Applied Spectroscopy* 67.5 (2013). PMID: 23643044, pp. 546–552.
- [152] A. Kohler, C. Kirschner, A. Oust, and H. Martens. “Extended Multiplicative Signal Correction as a Tool for Separation and Characterization of Physical and Chemical Information in Fourier Transform Infrared Microscopy Images of Cryo-Sections of Beef Loin”. In: *Applied Spectroscopy* 59.6 (2005), pp. 707–716.

- [153] Eric C Mattson, Miriam Unger, Binod Manandhar, Zahrasadat Alavi, and Carol J Hirschmugl. “Multi-beam Synchrotron FTIR Chemical Imaging: Impacts of Schwarzschild Objective and Spatial Oversampling on Spatial Resolution”. In: *Journal of Physics: Conference Series* 425.14 (2013), p. 142001.
- [154] Michael J. Nasse, Michael J. Walsh, Eric C. Mattson, Ruben Reininger, Andre Kajdacsy-Balla, Virgilia Macias, Rohit Bhargava, and Carol J. Hirschmugl. “High-resolution Fourier-transform infrared chemical imaging with multiple synchrotron beams”. In: *Nat Meth* 8.5 (2011), pp. 413–416.
- [155] Wikipedia contributors. *Atan2 — Wikipedia, The Free Encyclopedia*. <https://en.wikipedia.org/w/index.php?title=Atan2&oldid=859313982>. [Online; accessed 5-October-2018]. 2018.
- [156] Ichirou Yamaguchi, Jun ichi Kato, Sohgo Ohta, and Jun Mizuno. “Image formation in phase-shifting digital holography and applications to microscopy”. In: *Appl. Opt.* 40.34 (2001), pp. 6177–6186.
- [157] Cheng-Shan Guo, Li Zhang, Hui-Tian Wang, Jun Liao, and Y. Y. Zhu. “Phase-shifting error and its elimination in phase-shifting digital holography”. In: *Opt. Lett.* 27.19 (2002), pp. 1687–1689.
- [158] Pengyi Guo and Anthony J. Devaney. “Digital microscopy using phase-shifting digital holography with two reference waves”. In: *Opt. Lett.* 29.8 (2004), pp. 857–859.
- [159] M. F. Kasim. *Fast 2D phase unwrapping implementation in MATLAB*. 2017.
- [160] Miguel Arevallilo Herráez, David R. Burton, Michael J. Lalor, and Munther A. Gdeisat. “Fast two-dimensional phase-unwrapping algorithm based on sorting by reliability following a noncontinuous path”. In: *Appl. Opt.* 41.35 (2002), pp. 7437–7444.
- [161] Tatsuki Tahara, Xiangyu Quan, Reo Otani, Yasuhiro Takaki, and Osamu Matoba. “Digital holography and its multidimensional imaging applications: a review”. In: *Microscopy* 67.2 (Feb. 2018), pp. 55–67.

- [162] Yu Yao, Anthony J. Hoffman, and Claire F. Gmachl. “Mid-infrared quantum cascade lasers”. In: *Nature Photonics* 6 (2012). Review Article, p. 432.
- [163] Chuanfei Yao, Zhixu Jia, Zhenrui Li, Shijie Jia, Zhipeng Zhao, Lei Zhang, Yan Feng, Guanshi Qin, Yasutake Ohishi, and Weiping Qin. “High-power mid-infrared super-continuum laser source using fluorotellurite fiber”. In: *Optica* 5.10 (2018), pp. 1264–1270.
- [164] Carlo Cattani. *Wavelet and wave analysis as applied to materials with micro or nanostructure* Carlo Cattani, Jeremiah Rushchitsky. Series on advances in mathematics for applied sciences; v. 74. Hackensack, NJ: World Scientific Pub. Co., 2007.
- [165] Paul S Addison. *The illustrated wavelet transform handbook: introductory theory and applications in science, engineering, medicine and finance*. Bristol: Institute of Physics Publishing, 2002.
- [166] S. Mallat. *A Wavelet Tour of Signal Processing*. Wavelet Tour of Signal Processing. Elsevier Science, 1999.
- [167] F Jamme, B Lagarde, A Giuliani, G A Garcia, and L Mercury. “Synchrotron infrared confocal microscope: Application to infrared 3D spectral imaging”. In: *Journal of Physics: Conference Series* 425.14 (2013), p. 142002.
- [168] David L. Wetzel, Yong-Cheng Shi, and John A. Reffner. “Synchrotron Infrared Confocal Microspectroscopical Detection of Heterogeneity within Chemically Modified Single Starch Granules”. In: *Applied Spectroscopy* 64.3 (2010). PMID: 20223062, pp. 282–285.
- [169] Minsky Marvin. “Microscopy apparatus”. Pat. 3013467 (United States). 1961.
- [170] A.R. Hibbs. *Confocal Microscopy for Biologists*. Disease Management of Fruits and Vegetables Series. Springer US, 2004.
- [171] *Handbook of biological confocal microscopy*. Revised edition. New York: Plenum Press, 1990.

- [172] Tony Wilson. *Confocal microscopy*. Academic Press, 1990.
- [173] Eric Mattson, Michael J Nasse, Margaret Rak, Kathleen M Gough, and Carol Hirschmugl. “Restoration and Spectral Recovery of Mid-Infrared Chemical Images”. In: *Analytical chemistry* 84 (June 2012), pp. 6173–80.
- [174] Olivier Faugeras. *Three-dimensional computer vision: a geometric viewpoint*. Artificial intelligence (Cambridge, Mass.) Cambridge, Mass.: MIT Press, 1993.

Appendix: Overview of In-line Holography

Holography is an imaging technique for converting phase information from a scattering object into spatial intensity variations, using its interference with a known reference wave. Many books and articles covering the various methods, techniques, applications, and historical aspects of holography already exist; the purpose here is to highlight the most fundamental results that apply in the context of this work (particularly, Chapters 4 and 5). A comprehensive overview of the basics of holography may be found in Hariharan [84], while a thorough review of digital holographic microscopy methods and techniques are detailed by Kim [85]. A few practical algorithms for digital holography (including supplementary MATLAB [135] code) are provided by Latychevskaia and Fink [79]. Finally, as most holographic systems contain optical components such as focusing lenses (physical, digital, or both), the propagation of light in such systems are often treated mathematically with Fourier optics — an overview of which is available in Goodman [56].

Practically, there are an unlimited number of holographic system configurations that are possible for recording and reconstruction. However, the fundamental physics in each system can usually be related back to a few basic configurations – one of which is the subject of this appendix. In particular, in-line holography is perhaps the most fundamental configuration; however, at its most basic level the desired hologram is coupled with ambiguous information: both the desired phase and its conjugate are recorded (also known as the twin image problem). Off-axis holography is another very common and useful configuration that allows one to isolate these effects, although at the expense of decreased spatial resolution [161]. While most holographic configurations may be related to in-line and off-axis configurations, the in-line method is detailed here since it is fundamental to the methods presented in Chapter 4.

As is typical in the literature, the physics of electromagnetic fields considered here are treated with the scalar wave approximation; that is, polarization effects are assumed negligible. However, if an account of the polarization is required, the mathematical results may

be applied to each polarization state independently. For instance, if the source is randomly polarized, holograms may be recorded using linear polarization filters installed at the source and detector to record the horizontal and vertical responses separately.

A.1 In-line Holography

There are two types of in-line holography that will be examined: common path, and double path interferometers. In common path in-line holography, the reference field and scattered field share the same physical path (see Fig. A.1). This configuration is most similar to transmission Fourier-transform infrared spectroscopy microscopes. It will be shown that, if the scattered field is weak, certain approximations make this arrangement sufficient for recording and reconstructing objects from holograms (although limited by the twin-image problem inherent to in-line holography). In addition to having a less complex design with fewer optical components, this configuration has the benefit of being much more stable against vibrations [161]. Its downside, however, is that strongly absorbing or scattering objects invalidate the required approximations.

Double path in-line holography, on the other hand, physically separates the reference from the scattered field using beamsplitters. This allows greater control over the recording process; for instance, to adjust the contrast or, as will be shown, to digitally reconstruct a objects that may not fulfill the weak-scattering requirements of common path holography. Its drawbacks, however, include a more complex design and increased sensitivity to vibrational noise. Also, as with the common path arrangement, the double path in-line configuration also suffers from the twin-image problem.

A.1.1 Common Path Interference

Consider a weakly-scattering object \mathbf{O} placed at $z = 0$, which is illuminated by a monochromatic incident plane wave $U_0 = |U_0| \exp(i2\pi z/\lambda)$ with wavelength λ propagating in the $+z$

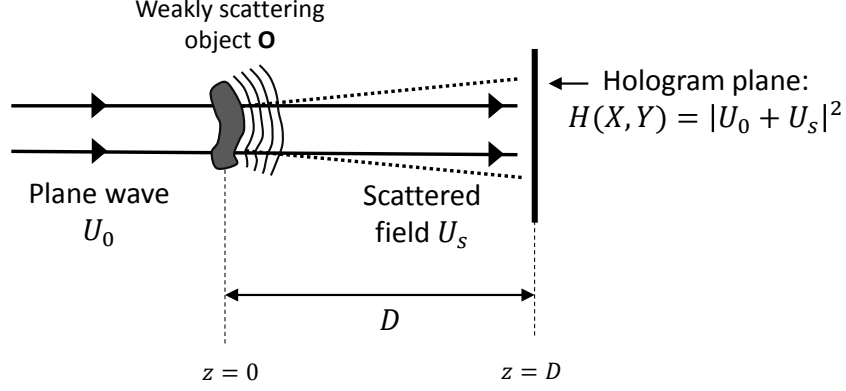


Figure A.1: Common path in-line holography recording configuration. An incident plane wave U_0 induces a field U_s from a weakly-scattering object \mathbf{O} . The fields U_0 and U_s interfere at the hologram plane located a distance D to the right.

direction (Fig. A.1). Denote by $U_s(X, Y) = |U_s(X, Y)| \exp(i\phi(X, Y))$ the scattered field (i.e., the field attributed solely to the object \mathbf{O}) at a distance $z = D$ downstream from \mathbf{O} . The intensity distribution H in the $z = D$ plane is therefore given by the modulus square of the superposition of the incident and scattered fields

$$\begin{aligned}
 H(X, Y) &= |U_0 + U_s|^2 \\
 &= U_0^2 + |U_s|^2 + U_0 U_s + U_0 U_s^* \\
 &= U_0^2 + |U_s(X, Y)|^2 + 2U_0 |U_s(X, Y)| \cos\{\phi(X, Y)\}
 \end{aligned} \tag{A-1}$$

Defining $z = D$ as the hologram plane, it is apparent that a recording of H includes both amplitude and phase information, where the phase ϕ at (X, Y) is encoded via the cosine term in Eq. A-1.

Since the object \mathbf{O} is assumed to be weakly scattering, $|U_s|$ is small, and the relative

intensity distribution $h(X, Y) = \frac{H(X, Y)}{U_0^2}$ is approximated as¹

$$h(X, Y) \approx 1 + \frac{2|U_s|}{|U_0|} \cos \{\phi(X, Y)\} \quad (\text{A-2})$$

Figure A.2 shows the reconstruction process. Illuminating the hologram $h(X, Y)$ with the original reference wave U_0 gives a field distribution $U^+(X, Y)$ immediately to the right of the hologram

$$\begin{aligned} U^+(X, Y) &\equiv h(X, Y) U_0 \\ &= \exp(ikz) (|U_0| + |U_s| \exp(i\phi) + |U_s| \exp(-i\phi)) \end{aligned} \quad (\text{A-3})$$

The second term in Eq. A-3 is the desired original scattered field distribution at the hologram plane which will then propagate to the right (+ z direction) according to the free-space Helmholtz equation [56] – exactly as it would if the object **O** were still situated a distance D to the left of the hologram. Unfortunately, however, the phase conjugate (third term), along with a zero-order wave (first term) are also superimposed. The phase conjugate, also known as the “twin image,” propagates as though the object is situated a distance D to the right of the hologram. A detector placed at $z = D$ would therefore detect three components: a real image formed by the third term, a virtual image originating from $z = -D$, and the zero-order field appearing as a DC offset due to the reference field (see Fig. A.2). In digital holography, a virtual detector may be placed at any location by numerically propagating the field the desired distance, bringing the object into focus on either side of the hologram plane [79].

Fortunately, for digitally recorded holograms, the zero-order term may be removed by subtracting unity from the hologram h before reconstruction. However, the twin image is in-

¹In traditional analog holography, H is the recorded signal, and the contrast of reconstructions are limited by the scaling factor $|U_0|^2$, along with any other non-linear material-dependent factors from the response of the film [84]. However, digital holography allows one to obtain h through measurement of a “background” image that does not contain the sample.

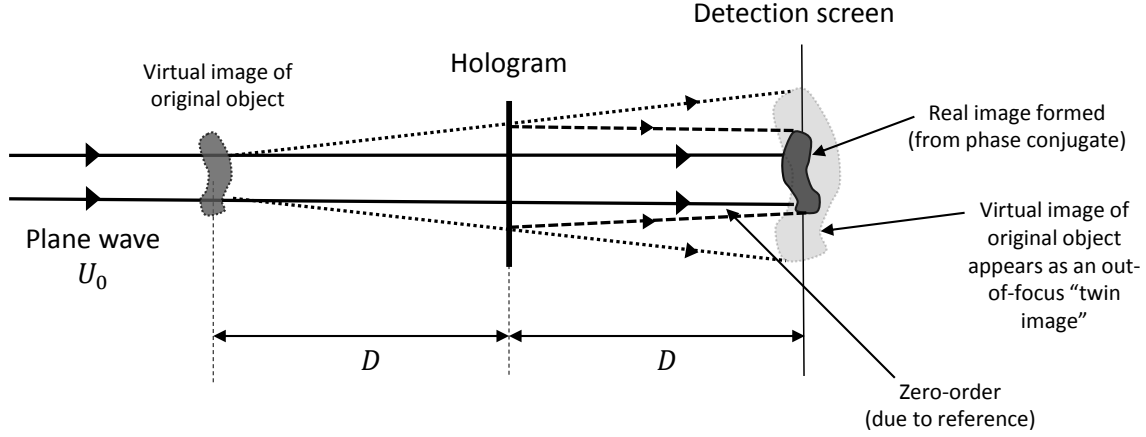


Figure A.2: The in-line hologram is reconstructed by illuminating the hologram with the original reference field U_0 . To the right of the hologram, three components emerge superimposed: the zero-order due to U_0 , a real image (which is the phase conjugate of the original object's field), and a virtual image of \mathbf{O} appearing out-of-focus at the detection screen.

separable without additional corrective algorithms [80]. In cases where the scattering object is located a large distance D from the hologram plane, the twin image may be sufficiently out of focus such that its presence is tolerable. Alternatively, more experimental flexibility is offered by using double path in-line holography, where methods such as phase-shifting holography [98, 156–158] may be used to eliminate the twin image.

A.1.2 Double Path Interference

The approximation for the common path in-line hologram h in Eq. A-2 assumed that the reference field is much larger than the scattered field $|U_0| \gg |U_s|$, such that the $|U_s|^2/|U_0|^2$ term is negligible. This is not ideal for many samples where larger absorbances may occur, especially in infrared imaging. Using double path interference, however, the term may be exactly removed with an additional measurement. It also allows other techniques to be utilized, such as modulating the reference field phase, which may be used for eliminating the twin image [98], or spectroscopy (Chapter 4).

One commonly used double path in-line configuration is the Mach Zehnder interferometer (MZI) [96, 97] shown in Fig. A.3. In this double path configuration, the source is equally²

²This assumption is only for mathematical simplicity. It is not necessary (or realistic) that the beamsplit-

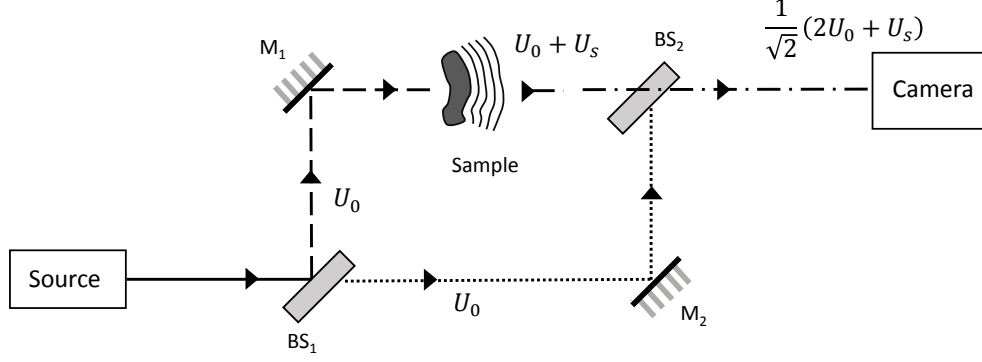


Figure A.3: In a Mach Zehnder interferometer, the source is split into two paths with strengths U_0 by the beamsplitter BS_1 (with a perfect transmitting/reflecting ratio assumed for simplicity). The total field along the sample path just before the second beamsplitter BS_2 is $U_0 + U_s$, where U_s is the scattered field due to the sample. This field is combined with the reference U_0 that was transmitted by BS_1 , and the total combined field at the camera by BS_2 is $U_0 + \frac{1}{2}U_s$.

reflected and transmitted by a beamsplitter BS_1 , so that the same “incident” field U_0 travels along two physically separate equidistant paths. Along the sample path, the incident field U_0 interacts with the sample, inducing a scattered field U_s ; the total field along this path just before the second beamsplitter BS_2 is $U = U_0 + U_s$. The recorded hologram H is therefore

$$H(X, Y) = \frac{1}{2}|U + U_0|^2 \quad (\text{A-4})$$

$$= \frac{1}{2} [U_0^2 + |U(X, Y)|^2 + 2U_0|U(X, Y)| \cos \{\phi(X, Y)\}] \quad (\text{A-5})$$

Note that, if the reference path (the field transmitted by BS_1) were blocked, the resulting intensity at the detector $\frac{1}{2}|U(X, Y)|^2$ would be identical to the common path case (Sec. A.1.1), up to a scaling factor due to attenuation from the beamsplitter. However, in the double path configuration the primary interference is between the two paths. One benefit in this case is that a separate measurement of the sample path (with the reference path blocked) allows the second term in Eq. A-5 to be subtracted using this measurement. Then, dividing through by the background reference U_0 as in the common path case, a normalized

ters perfectly transmit and reflect with 50% efficiency, although they should be close to achieve the greatest possible signal-to-noise measurement. See Ch. 4 (Sec. 4.2.3) for more details.

hologram h is obtained for the total field U , without the approximation used previously in Eq. A-2

$$h(X, Y) = 1 + \frac{2|U|}{|U_0|} \cos \{\phi(X, Y)\} \quad (\text{A-6})$$

Depending on the purpose of the hologram, the total field U along the sample path may be the desired quantity, such as in quantitative phase microscopy [61, 85]. However, for applications such as diffraction tomography [29, 42], the scattered field U_s is of interest. In this case, one may extract U_s from the total field using knowledge of the incident field U_0 (such as a plane wave), or performing an additional holography measurement where U_0 is the “sample” whose field is obtained. In either case, the setup described is still limited since the twin-image has not been removed. However, various modifications of the MZI setup in Fig. A.3 may be used to eliminate the twin-image (e.g., phase-shifting holography [98], or Fourier-transform holographic spectroscopy in Ch. 4).

A.1.3 Example: Imaging a Point Source

An illustrative example of a point source hologram is now given. There are two ways in which a point source hologram may be acquired: a completely opaque screen at the $z = 0$ plane with a small opening at the position (x_p, y_p) (see Fig. A.4), or a small obstruction at (x_p, y_p) . In the first case, a double path configuration is required (not shown) since the mostly opaque screen blocks the reference field (i.e., it is considered a large scatterer). For a small point obstruction, however, either configuration will produce a hologram. In fact, this situation frequently arises in practice, as dust and small imperfections along the optical path can cause point-source diffraction effects that superimpose at the hologram plane. In either case, the mathematics are the same for both cases (up to a phase factor). For non-point source samples, the results here are still illustrative since the Huygens principle states that an arbitrary field may be thought of as a superposition of point-sources located along its

wavefront [56].

Consider a point source \mathbf{P} positioned at coordinates $(x_p, y_p, 0)$ which radiates spherical waves toward the hologram plane situated a distance $z = D$ from \mathbf{P} as shown in Fig. A.4. The field U_p due to a radiating point source is [56]

$$U_p = A \frac{\exp ikR}{R}, \quad (\text{A-7})$$

where

$$R = \sqrt{(x - x_p)^2 + (y - y_p)^2 + z^2} \quad (\text{A-8})$$

and A is the source's field strength. Close to the principal axis z (i.e., when $\delta_x^2 = \frac{(X-x_p)^2}{z^2}$ and $\delta_y^2 = \frac{(Y-y_p)^2}{z^2}$ are very small), the paraxial approximation is useful to employ. Although distortions will be introduced when these conditions are not fulfilled, the approximation helps in obtaining a qualitative understanding of the holographic principles. In the paraxial approximation, the radial distance R is expanded to second order in δ_x and δ_y , and U_p becomes

$$U_p(x, y) \approx \frac{A}{z} \exp(ikz) \exp \left\{ \frac{ik}{2z} ((x - x_p)^2 + (y - y_p)^2) \right\} \quad (\text{A-9})$$

At the hologram plane, the field $U_p(X, Y)$ is therefore

$$U_p(X, Y) = \frac{A}{D} \exp \left\{ \frac{ik}{2D} ((X - x_p)^2 + (Y - y_p)^2) \right\} \quad (\text{A-10})$$

where constant phase factors are ignored for simplicity. Using Eq. A-2 (or Eq. A-6), the

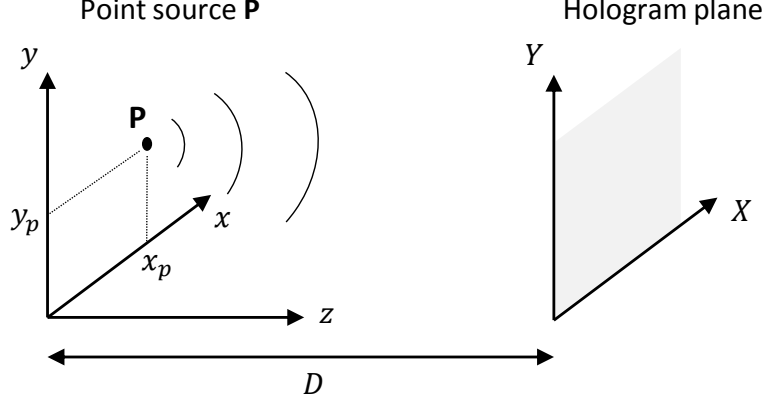


Figure A.4: Point source diffraction at coordinates (x_p, y_p) produce the Fresnel zone holograms in Fig. A.5 for various distances D . The point source \mathbf{P} may be due to a small obstruction (e.g., dust), or from a small opening of an opaque screen, in which case a double-path configuration is required to interfere with a reference field (not shown).

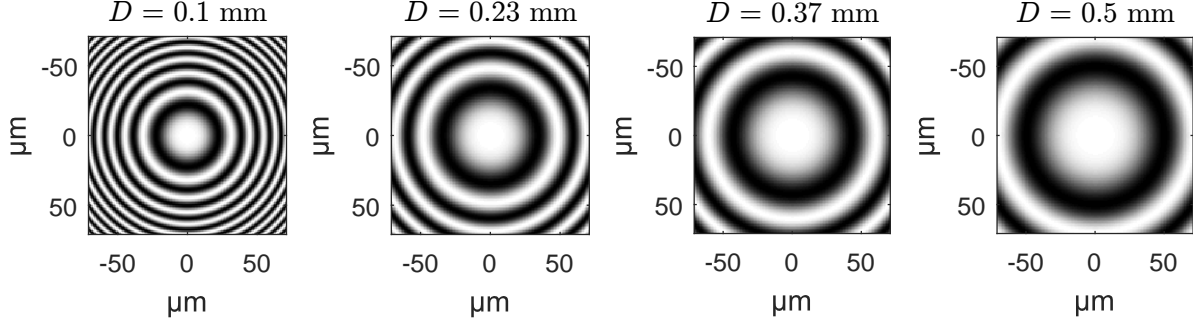


Figure A.5: Example Fresnel zone plates due to a point source located at various distances D from the hologram plane (Fig. A.4). The hologram is a 128×128 image with a linear pixel size of 1.1 μm , capturing the interference of a point source located at the origin, radiating with a wavelength $\lambda = 5$ μm .

normalized hologram h_p of \mathbf{P} with an in-line plane wave reference is therefore

$$h_p(X, Y) = 1 + \frac{2A}{D|U_0|} \cos \left\{ \frac{k}{2D} ((X - x_p)^2 + (Y - y_p)^2) \right\} \quad (\text{A-11})$$

$$= 1 + 2 \frac{\Re[U_p]}{|U_0|}, \quad (\text{A-12})$$

Holograms for point sources located at various distances D are illustrated in Fig. A.5. The field pattern $U_p(X, Y)$ at the hologram plane is known as a Fresnel Zone Plate.

The problem of the twin image discussed in Sec. A.1 can also be illustrated by recon-

structing the point source hologram. Illuminating h_p with the reference plane wave U_0 gives

$$\begin{aligned}
U^+ &= U_0 h_p = (U_0 + 2\Re[U_p]) \exp(ikz) \\
&= U_0 \exp(ikz) + \exp\left\{ikz + \frac{ik}{2D}((X - x_p)^2 + (Y - y_p)^2)\right\} + \\
&\quad \exp\left\{ikz - \frac{ik}{2D}((X - x_p)^2 + (Y - y_p)^2)\right\}
\end{aligned} \tag{A-13}$$

Inspection of terms in Eq. A-13 reveals that the reconstructed field can be interpreted as a zero order passage of the reference beam (first term), along with a diverging wave from a point source located a distance $-D$ from the hologram plane (second term), as well as a wave converging to a point source located on the opposite side D of the hologram plane (third term). From the Huygens principle, it is therefore evident that reconstructions of in-line holograms of arbitrary objects inherently includes an overlapping of a real and virtual image the object. In Chapter 4, we present a modification of the MZI in Fig. A.3 adapted for holographic spectroscopy, which not only removes this twin image, but also works with polychromatic sources.

CURRICULUM VITAE

Alex J. Schofield

Place of birth: Milwaukee, WI

Education

B.S., University of Wisconsin-Milwaukee, May 2013

Major: Computer Science & Physics

Dissertation Title: Scattering in Infrared Microspectroscopy

Research Experience

Graduate Research Assistant (Infrared Spectroscopy), 2015–2019

Mid-infrared scattering phenomena and holography, 3D tomographic imaging and analysis

Graduate Research Assistant (Astrophysics), 2014–2015

Numerical simulations and analysis of star formation

Undergraduate Research Assistant (Astronomy), 2012–2013

Assisted in software pipeline design for automatic transient detection in VLA data

Publications

1. Schofield, Alex J., Blümel, Reinhold, Kohler, Achim, Lukacs, Rozalia, & Hirschmugl, Carol J., “Extracting pure absorbance spectra in infrared microspectroscopy by modeling absorption bands as Fano resonances”, *J. Chem. Phys.* 150, 154124 (2019)
2. Aboualizadeh, E., Sorenson, C. M., Schofield, A. J., Unger, M., Sheibani, N., & Hirschmugl, C. J., “Temporal diabetes-induced biochemical changes in distinctive layers of mouse retina”, *Scientific Reports*, 8(1), 1096 (2018)

Presentations

Schofield, A.J., Blümel, Reinhold, Kohler, Achim, Lukacs, Rozalia, Hirschmugl, Carol J., “Fano resonances in infrared spectroscopy”. Oral presentation at SciX 2018, Oct., Atlanta, GA

Schofield, A.J., et. al., “Fano resonances in infrared spectroscopy”. Poster presented at AVS Prairie Chapter Symposium 2017, Sept., Milwaukee, WI

Schofield, A.J., Hirschmugl, Carol J., “Digital confocal infrared spectroscopy”. Poster presented at SciX 2016, Sept., Minneapolis, MN

Awards/Honors

Editor's Pick: Publication No. 1 (In: *Journal of Chemical Physics*), 2019

Chancellor's Graduate Student Award, 2018

Summer Research Fellowship, 2018

Lichtman Memorial Award, 2018

Summer Research Award (Qualifier exam completed on first attempt), 2013

Dean's List, Spring 2011, Fall 2009, Spring 2009

Teaching Experience

Graduate Teaching Assistant, UW-Milwaukee

Undergraduate Teaching Assistant, UW-Milwaukee

Math & Physics Tutoring, UWM Panther Academic Support Services